Evolution of compressible Görtler vortices subject to free-stream vortical disturbances

Samuele Viaro

Supervisor: Dr. Pierre Ricco

Department of Mechanical Engineering

University of Sheffield

This dissertation is submitted for the degree of

Doctor of Philosophy

February 2019

Dedicato alle persone che mi stanno piú a cuore:
mio padre Sergio, mia madre Lodovica, mia sorella Jessica e...la piccola Joy!

Insieme abbiamo raggiunto anche questo traguardo.

Acknowledgements

I would like to acknowledge the financial support of the US Air Force with the AFOSR grant FA9550-15-1-0248. I would also like to thank Dr. Marvin Goldstein and the Ohio Aerospace Institute for hosting me during my time abroad. I am also very grateful to my supervisor, Dr. Pierre Ricco, for guiding me through my doctoral studies. Special thanks go to my family without whom I would not have been able to complete my studies.

Abstract

The perturbations triggered by free-stream vortical disturbances in compressible boundary layers developing over concave walls are studied numerically and through asymptotic methods. We employ an asymptotic framework based on the limit of high Görtler number, the scaled parameter defining the centrifugal effects, we use an eigenvalue formulation where the free-stream forcing is neglected, and solve the receptivity problem by integrating the compressible boundary-region equations complemented by appropriate initial and boundary conditions which synthesize the influence of the free-stream vortical flow. In the limit of high frequencies, the triple-deck equations are also solved and their results compared with the solution of the boundary-region equations. The boundary-layer perturbations, in the proximity of the leading edge, develop as thermal Klebanoff modes and, when centrifugal effects become influential, these modes turn into thermal Görtler vortices, i.e., streamwise rolls characterized by intense velocity and temperature perturbations. The high-Görtler-number asymptotic analysis reveals the condition for which the Görtler vortices start to grow and that the Mach number is destabilizing when the spanwise diffusion is negligible and stabilizing when the boundary-layer thickness is comparable with the spanwise wavelength of the vortices. The theoretical analysis also shows that the vortices move towards the wall as the Mach number increases when the Görtler number is large. These results are confirmed by the receptivity analysis, which additionally clarifies that the temperature perturbations respond to this reversed behavior further downstream than the velocity perturbations. A matched-asymptotic composite profile, found by combining the inviscid core solution and the near-wall viscous solution, agrees well with the receptivity profile sufficiently downstream and at high Görtler number. The Görtler vortices tend to move towards the boundary-layer core when the flow

is more stable, i.e., as the frequency or the Mach number increase, or when the curvature decreases. As a consequence, a region of unperturbed flow is generated near the wall. We also find that the streamwise length scale of the boundary-layer perturbations is always lower than the free-stream streamwise wavelength. During the initial development of the vortices, only the receptivity calculations are accurate. Downstream where the free-stream disturbances have fully decayed, the growth rate and wavelength are computed accurately by the eigenvalue analysis, although the correct amplitude of the Görtler vortices can only be determined by the receptivity calculations. It is further proved that the eigenvalue predictions of the growth rate and wavenumber worsen as the Mach number increases, as these quantities show a dependence on the wall-normal direction.

The receptivity analysis is also used to compute the neutral curves generated by free-stream disturbances, i.e., curves that identify the region of growth and decay of the boundary-layer perturbations, for different Görtler numbers, Mach numbers, wavelengths, and low frequencies of the free-stream disturbance. The growth rate of the perturbation is used to identify if the boundary-layer instability is in the form of Klebanoff modes or Görtler vortices. A critical Görtler number can be identified below which Klebanoff modes are the only source perturbations, even when curvature is present. From the receptivity and eigenvalue formulation we define a streamwise-dependent receptivity coefficient and discuss the N-factor approach for transition prediction.

Finally, the equations the triple-deck analysis reveals that the curvature effects do not play a role in the limit of high frequencies, which is also confirmed by the boundary-region results.

Table of contents

List of figures

List of tables

Nomenclature

Roman Symbols

$\mathtt{G}$	Görtler number $\mathtt{G} = \frac{\mathtt{R}^2}{r}$
$\mathtt{K}$	Klebanoff modes
k	wavenumber
$\mathtt{M}$	Mach number
$\mathtt{R}$	Reynolds number based on Λ_z^*: $\mathtt{R} = \frac{U_\infty^* \Lambda_z^*}{\nu_\infty^*}$
x	Dimensionless coordinates in the streamwise direction
y	Dimensionless coordinates in the wall-normal direction
z	Dimensionless coordinates in the spanwise direction

Greek Symbols

λ	wavelength

Superscripts

$*$	Dimensional quantities

Subscripts

∞	oncoming free stream

Acronyms / Abbreviations

EV Eigenvalue

$\bar{x}$-LUBR Linearized Unsteady Boundary Region in $(\bar{x}, \eta)$

LUBR Linearized Unsteady Boundary Region in $(\hat{x}, \eta)$

Chapter 1

Doctoral development

1.1 Conferences

This work has been presented at the following conferences:

- Fluid mechanics conference, Prague, March 2017;
- AFSOR hypersonic portfolio review, NASA Langley center Virginia, July 2017;
- European Turbulence Conference, Stockholm, August 2017;
- Euromech colloquia on instabilities, Bari, September 2017;
- APS-Division of Fluid Dynamics, Denver, November 2017;
- EFMC 12, Vienna, September 2018;

1.2 Publications

The list of publications includes:

- S.Viaro, P.Ricco, ”Neutral stability curves of low-frequency Görtler flow generated by free-stream vortical disturbances”, J. Fluid Mech.-Rapids, 845, 2018;

- S.Viaro, P.Ricco, “Compressible unsteady Görtler vortices subject to free-stream vortical disturbances”, JFM-18-S-1023.R1;
- S.Viaro, P.Ricco, “Neutral stability curves of compressible Görtler flow generated by free-stream vortical disturbances”, J. Fluid Mech.-Rapids (to be submitted)

Chapter 2

Introduction

In 1940 Görtler (1940) published a paper where a new type of boundary-layer instability was introduced. This Görtler instability originates from an inviscid unbalance between pressure and centrifugal forces caused by the curvature of flow streamlines. In most cases, curvature is introuce thanks to a curved concave surface, as shown in figure 2.1. The resulting perturbation

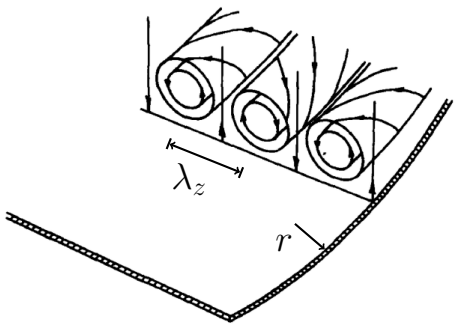

Fig. 2.1 Representation of Görtler vortices edveloping along concave surfaces.

evolves in the form of counter-rotating vortices which are elongated in the streamwise direction. Their streamwise velocity dominates over the cross-flow velocities. They evolve slowly in the streamwise direction and with a constant spanwise wavelength. They have been referred to as Görtler vortices. Görtler's mathematical result was confirmed experimentally by Liepmann (1945), who first showed that transition to turbulence is anticipated with respect to the flat-plate case. Comprehensive reviews on Görtler flow have been published by Hall (1990), Floryan (1991), and Saric (1994).

2.1 Incompressible Görtler vortices

The original work of Görtler (1940) was based on a theory simplified by the parallel mean-flow assumption which contrasts with the growing nature of boundary layers. Tani (1962) first performed detailed measurements of the perturbed flow proving that Görtler vortices evolve with a nearly constant spanwise wavelength. An improvement to the original theory was achieved in the work of Floryan and Saric (1982) by introducing non-parallel effects and using other assumptions which led to an eigenvalue system of ordinary differential equations. When the dimensional spanwise wavelength of Görtler vortices is of the same order as the boundary-layer thickness, Hall (1983) demonstrated that any assumption simplifying the governing partial differential equations to ordinary differential equations does not lead to a precise description of the evolution of the Görtler vortices, so that for example the amplitude of the perturbations, the dependence of the growth rate on the wall-normal direction, and the flow behaviour near the leading edge would not be computed correctly. In the same paper several disturbance profiles were introduced at different streamwise locations near the leading edge as initial conditions and, for each location and initial profile, the instability developed in a different manner. The influence of the external disturbances was not accounted for and the perturbations were assumed to vanish outside of the boundary layer. Swearingen and Blackwelder (1983) and Kottke (1988) proved experimentally that receptivity of the base flow to free-stream turbulence has a strong impact on the properties of Görtler instability, such as the spanwise wavelength, and on the breakdown of the vortices to turbulence. Hall (1990) was the first to introduce the effect of receptivity to free-stream turbulence on the Görtler vortices, obtaining a better agreement with experimental data than for the cases where artificial initial conditions were imposed at a fixed streamwise location. More recently, Borodulin et al. (2017) also claimed that free-stream turbulence is one of the most efficient ways to excite Görtler instability.

A further pioneering step towards understanding receptivity was achieved by Leib et al. (1999), who formulated a rigorous mathematical framework based on the unsteady boundary region equations that, through asymptotic matching, unequivocally fixes the initial and outer boundary conditions based on the external free-stream vortical disturbances. They

focused on the incompressible viscous instabilities that arise in flat-plate boundary layers in the form of streamwise elongated vortices, known as Klebanoff modes, now widely recognized to be initiators of bypass transition to turbulence (Matsubara and Alfredsson, 2001; Ovchinnikov et al., 2008). Localized streaks have also been investigated using the boundary region equations (Hewitt and Duck, 2018). Recently, Ricco et al. (2016) highlighted the strengths of the framework introduced by Leib et al. (1999) by comparing it to other theoretical approaches found in literature for the analysis of bypass transition, and proved its validity by showing good agreement with the experimental data and with the direct numerical simulation data of Wu and Moin (2009). When streamwise concave curvature is present, Klebanoff modes turn into Görtler vortices as they evolve downstream. This was first proved by Wu et al. (2011) by extending the theory of Leib et al. (1999) for flows over concave surfaces where free-stream turbulence was modeled by three-dimensional vortical external disturbances. Their theoretical results agree well with the experimental data in the linear region of evolution (Boiko et al., 2010b; Finnis and Brown, 1997; Tani, 1962). In the limit of high Görtler number, the asymptotic analysis of Wu et al. (2011) revealed the different stages through which the Görtler instability evolves. It goes through two pre-modal stages and then it amplifies exponentially. During their growth, the vortices become trapped in a wall layer. This is a distinctive feature of incompressible Görtler vortices and it is markedly different from the behavior of Klebanoff modes, which tend to move to the upper part of the boundary layer.

The effects of nonlinearity on the unsteady Görtler vortices triggered by free-stream vortical disturbances have been studied by Boiko et al. (2010a), Xu et al. (2017) and Marensi and Ricco (2017), whereas the effects of nonlinearity on the mean flow was investigated by Hewitt and Duck (2014). In addition, the excitation of Görtler vortices by local surface nonuniformities has been recently investigated by Boiko et al. (2017).

2.2 Compressible Görtler vortices

The initiation of the transition to turbulence caused by Görtler instability affects the performance of several technological applications, especially in the compressible regime. A typical important example is the high-speed flow in turbine engine intakes, where the free stream is highly disturbed. It is thus crucial to study the influence of free-stream disturbances to predict transition in these systems and to evince how the change of the flow regime from laminar to turbulent affects the performance of turbomachines (Mayle, 1991; Volino and Simon, 1995). Additional examples of Görtler flows in the compressible regime include airfoils (Mangalam et al., 1985), hypersonic air breathing vehicles (Ciolkosz and Spina, 2006), and supersonic nozzles (Chen et al., 1992).

Compressible Görtler vortices were originally described by the parallel theory of Hammerlin (1961) and were first visualized by Ginoux (1971). A parallel theory was also employed later by Kobayashi and Kohama (1977) and was further extended to include non-parallel effects by El-Hady and Verma (1983), Hall and Malik (1989), and Hall and Fu (1989). The eigenvalue approach was improved by Spall and Malik (1989) by solving a system of partial differential equations coupled with prescribed initial conditions under the assumption of vanishing perturbations outside the boundary layer. Spall and Malik (1989) also mentioned that physically meaningful initial conditions do require receptivity, i.e., the process by which external disturbances interact with the perturbations inside the boundary layer. This work was later modified by Wadey (1992) through a new set of improved initial conditions, but receptivity was still not introduced. The eigenvalue approach with vanishing perturbations in the free stream was also adopted by Dando and Seddougui (1993) to study compressible Görtler vortices. From these early theories it was first noticed that increasing the Mach number leads to a more stable flow and to a shift of the vortices away from the wall. More recently, two conference papers by Whang and Zhong (2002, 2003) reported direct numerical simulation results on the influence of free-stream disturbances on Görtler vortices in the hypersonic regime, Li et al. (2010) investigated the nonlinear development of Görtler instability through nonlinear parabolized stability equations and direct numerical simulations, and Ren and Fu

(2015) showed how differences in the primary instability lead to considerable changes in the secondary instability, thereby impacting the transition to turbulence.

Experimental works on compressible Görtler flows are more limited than incompressible flows. De Luca et al. (1993) experimentally confirmed that in the compressible regime Görtler vortices also evolve with a constant spanwise wavelength. Ciolkosz and Spina (2006) ran experimental tests on transonic and supersonic Görtler vortices and showed that the spanwise wavelength of the vortices remained approximately constant as the Mach number and Görtler number varied and that the measured growth rates agreed reasonably well with existing stability results. Görtler vortices were also noticed to be the unwanted cause of transition for the design of quiet hypersonic wind tunnels (Schneider, 2008). Wang et al. (2018) performed a flow visualization of the complete evolution of Görtler vortices from the laminar to the turbulent regime reporting that, although the linear growth rate decreases as the Mach number increases, the secondary instability was enhanced. They also stressed that the theoretical works are steps ahead of the limited number of experimental works on compressible Görtler instability. To the best of our knowledge, rigorous experiments on compressible flows over concave surfaces describing the effect of free-stream turbulence on the Görtler vortices are indeed not available in the literature. This has arguably been one of the reasons why, although progresses have been made, there are no theoretical works on the receptivity of compressible boundary layers over concave surfaces to free-stream vortical disturbances and on the engendered unsteady Görtler vortices.

2.3 Neutral stability

Thanks to the theoretical advancements for the incompressible flows, which culminated in the work of Wu et al. (2011), and compressible flows, here presented, the Görtler flow is connected in a unique and precise way to the properties of free-stream disturbances. However, the neutral curves associated to concave surfaces, i.e., curves that identify regions of stability and instability of the boundary-layer, were not investigated by Wu et al. (2011) and it does continue to be an unsolved issue for both incompressible and compressible flows. On the

contrary, the problem of neutral curves for flat plates subject to TS waves instability was solved by Tollmien (1929).

The first neutral curves were computed based on the simplified parallel flow theories, such as the original work of Görtler (1940), which lead to inconsistent results for wavenumbers of order one and unphysical results for small wavenumbers. Only in the limit of high spanwise wavenumbers the parallel flow theories are acceptable (Hall, 1990). Hall (1983) showed the influence of different initial conditions on the neutral curves and, thanks to a receptivity analysis, improved his results in Hall (1990). However, even this last formulation was unable to capture all the experimental unstable points of Tani (1962) which are indeed included in the unstable regions computed by Viaro and Ricco (2018). The neutral stability curves of Viaro and Ricco (2018) were computed with the theory of Wu et al. (2011) and are here extended to include the effects of compressibility. In their neutral curves the complete range of low frequencies and spanwise wavenumbers is covered, starting from the leading edge and including the flat plate scenario. They also demonstrate the existence of a Görtler number below which only Klebanoff modes are present, even over curved surfaces, and a Görtler number above which Klebanoff modes shift into Görtler vortices directly.

2.4 Objectives

The objective of this research is to study the receptivity to free-stream vortical disturbances of compressible boundary layers over streamwise-concave surfaces and the consequent growth of unsteady Görtler vortices. We use asymptotic methods and numerical computations to solve the equations of motion. We achieve this goal by combining the theoretical framework of Wu et al. (2011) for incompressible flows over concave surfaces and the one of Ricco and Wu (2007), who extended the theory by Leib et al. (1999) to study compressible Klebanoff modes over flat surfaces. We focus on boundary layers where the free-stream Mach number is of order one and the instability only takes the form of Görtler vortices, i.e., at sufficiently low frequencies for which oblique Tollmien-Schlichting waves do not appear at realistic streamwise locations. We thus exclude the range of frequencies for which the receptivity

mechanism discovered by Ricco and Wu (2007) is operational. Our rigorous theoretical framework allows us to compute the neutral stability curves for different flow conditions. We finally adopt a triple-deck approach to show that there is no curvature effect in the limit of high frequencies.

Section §3.1.1 outlines the flow scaling and decomposition, while §3.2 presents the unsteady boundary-region equations with curvature effects. Starting from these equations, in §3.3 we derive a compressible eigenvalue framework with and without the parallel-flow assumption, in §3.4 we adopt an asymptotic framework valid at high Görtler numbers to study the different evolution stages and in §3.5 we derive the triple-deck equations valid at high frequencies. Section §4.1.1-§4.1.4 show the influence of compressibility, radius of curvature, oncoming vortical disturbances and frequency on the development of the instability. The growth rate is shown in §4.1.5 whereas in §4.1.6 a qualitative comparison with the direct numerical simulation (DNS) results by Whang and Zhong (2003) is proposed. The results for the neutral stability curves are presented in §4.1.7. Through the receptivity analysis, we modify the receptivity coefficient introduced by Wu et al. (2011) in §4.2.3 in order to recover the maximum amplitude of the perturbation inside the boundary layer starting from the local eigenvalue solution. Additionally, we discuss in §4.2.4 the `N`-factor approach when receptivity is introduced in the analysis of boundary layers subject to free-stream disturbances. The numerical boundary-region solutions are compared with the eigenvalue, the asymptotic and triple-deck solutions in §4.2, §4.3 and §4.4, respectively.

Chapter 3

Theoretical results

3.1 Scaling and equations of motion

We consider a uniform compressible air flow of velocity U_∞^* and temperature T_∞^* past a slightly concave plate with constant radius of curvature r^*. Hereinafter the asterisk * identifies dimensional quantities. In the proximity of the surface, the flow is described by the orthogonal curvilinear coordinate system $\mathbf{x} = \{x, y, z\}$ (Floryan and Saric, 1982) that defines the streamwise, wall-normal, and spanwise directions. Therefore, x is the streamwise coordinate, y is the wall-normal coordinate, and z is the spanwise coordinate, orthogonal to x and y. The conversion from the Cartesian to the curvilinear coordinates system is achieved through the Lamé coefficients $h_x = 1 - y^*/r^*, h_y = 1$, and $h_z = 1$ (Wu et al., 2011). The flow domain is represented in figure 3.1.

The free-stream disturbances are assumed to be of small intensity, passively advected by the uniform free-stream flow, and of the gust-type. These three-dimensional vortical disturbances, far upstream and away from the wall, take the form

$$\mathbf{u} - \mathbf{i} = \varepsilon \hat{\mathbf{u}}^\infty \, e^{i(\mathbf{k}\cdot\mathbf{x} - k_x \mathrm{R} \hat{t})} + \text{c.c.}, \tag{3.1}$$

where c.c. indicates the complex conjugate, ε is a small parameter, $\mathbf{i}$ is the unit vector along the streamwise direction, and $\hat{t}$ is the dimensionless time defined below. The oncoming veloc-

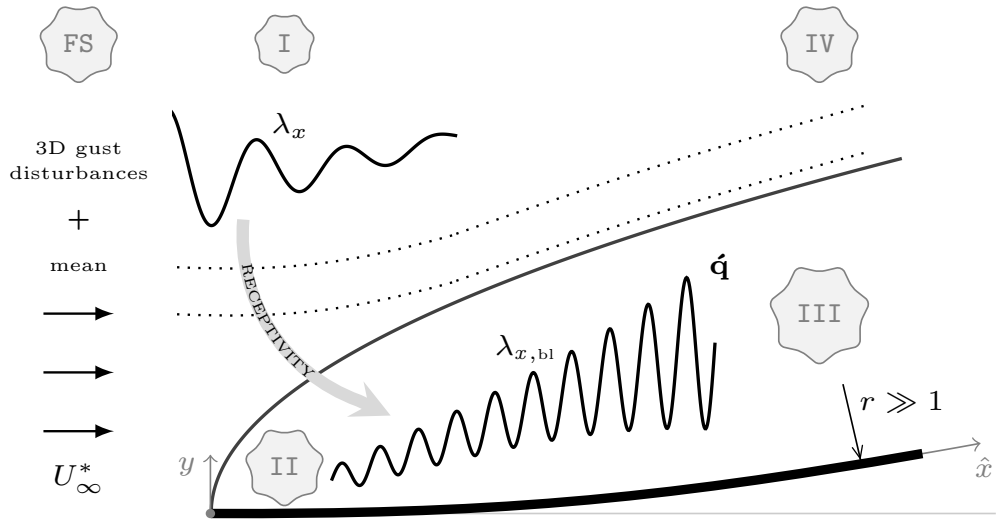

Fig. 3.1 Sketch of the receptivity mechanism to free-stream vortical disturbances and the asymptotic regions $\mathtt{I}, \mathtt{II}, \mathtt{III}, \mathtt{IV}, \mathtt{FS}$ of the boundary layer. λ_x is the streamwise wavelength of the free-stream disturbance and $\lambda_{x,\mathrm{bl}}$ is the streamwise wavelength of the boundary-layer perturbation $\acute{\mathbf{q}}$ sufficiently downstream from the leading edge.

ity $\mathbf{u}$ is therefore decomposed into its dimensionless mean, $-\mathbf{i}$, and a three-dimensional disturbance $\hat{\mathbf{u}}^\infty\, e^{i(\mathbf{k}\cdot\mathbf{x}-k_x \mathtt{R}\hat{t})}$ that is assumed to be convected by the mean flow of non-dimensional velocity of one. The wavenumber vector $\mathbf{k} = \{k_x, k_y, k_z\}$ and the amplitude of the free-stream velocity disturbance $\hat{\mathbf{u}}^\infty = \{\hat{u}^\infty, \hat{v}^\infty, \hat{w}^\infty\}$ satisfy the solenoidal condition $\mathbf{k}\cdot\hat{\mathbf{u}}^\infty = 0$. The characteristic length scale is $\Lambda_z^* = \lambda_z^*/2\pi$, where λ_z^* is the spanwise wavelength of the gust. As the flow is periodic along the spanwise direction and the boundary-layer dynamics is linear because the perturbation is assumed of small amplitude, λ_z^* is also the spanwise wavelength of the Görtler vortices. This is supported by laboratory evidence as experiments in both incompressible and compressible boundary layers over concave plates have reported a constant spanwise length scale of the vortices (Ciolkosz and Spina, 2006; De Luca et al., 1993; Tani, 1962). The characteristic velocity, temperature and pressure are U_∞^*, T_∞^*, and $\rho_\infty^* U_\infty^{*2}$, respectively, where ρ_∞^* is the mean density of air in the free stream. $\mathtt{R} = U_\infty^* \Lambda_z^* / \nu_\infty^* \gg 1$ defines the Reynolds number, where ν_∞^* is the kinematic viscosity of air in the free stream, $\mathtt{G} = \mathtt{R}^2 \Lambda_z^*/r^* = \mathscr{O}(1)$ defines the Görtler number, and $\mathtt{M} = U_\infty^*/a_\infty^* = \mathscr{O}(1)$ defines the Mach number, where $a_\infty^* = (\gamma \mathscr{R}^* T_\infty^*)^{1/2}$ is the speed of sound in the free stream, $\mathscr{R}^* = 287.06$ J

$\mathrm{kg}^{-1}\ \mathrm{K}^{-1}$ is the ideal gas constant for air, and $\gamma = 1.4$ is the ratio of specific heats. The parameter for frequency becomes $k_x\mathtt{R} = 2\pi\Lambda_z^{*2}U_\infty^*/(\lambda_x^*\nu_\infty^*)$ and the dimensionless spanwise wavenumber is $k_z = 1$. Time and the streamwise coordinate are scaled as $\hat{t} = U_\infty^* t^*/(\mathtt{R}\Lambda_z^*)$ and $\hat{x} = x^*/(\mathtt{R}\Lambda_z^*)$, respectively, due to our interest in streamwise elongated perturbations. The streamwise scaling used in Ricco and Wu (2007) could have been implemented, i.e., $\bar{x} = k_x x$, but we would have not been able to investigate the steady perturbations $k_x = 0$ as in Wu et al. (2011).

Ricco and Wu (2007) proved that, for certain flow conditions defined by the parameter $\kappa = k_z/(k_x\mathtt{R})^{1/2}$, the spanwise pressure gradient of the disturbance couples with the boundary-layer vortical disturbances to generate highly oblique TS waves at sufficiently large streamwise locations $\hat{x}_c$. For $\mathtt{M} = 3$, this instability appears when $0 < \kappa < 0.03$. As $\mathtt{M}$ decreases, the neutral point $\hat{x}_c$ moves downstream and if $\mathtt{M} < 0.8$ the $\hat{x}_c$ location is too far downstream to be physically relevant. In our study we restrict ourselves to cases for which $\kappa > 0.15$, a value that comes from our choice of experimental parameters for the investigation of the frequency influence in §4.1.4 , and therefore the highly-oblique TS waves investigated by Ricco and Wu (2007) do not occur.

3.1.1 Flow decomposition

The boundary-layer velocity, pressure, and temperature $\mathbf{q} = \{u, v, w, p, \tau\}$ are decomposed into their mean $\mathbf{Q} = \{U, V\}$ and perturbation $\acute{\mathbf{q}}$ as

$$\mathbf{q}(\mathbf{x}, t) = \mathbf{Q}(\mathbf{x}) + \varepsilon\,\acute{\mathbf{q}}(\mathbf{x}, t). \tag{3.2}$$

Under the assumption $r \gg 1$, curvature effects on the mean flow can be neglected (Spall and Malik, 1989). Consequently, at leading order the mean flow behaves as if the plate were flat. The Dorodnitsyn-Howarth transformation, which is the equivalent of the Blasius formulation but for compressible flows, can then be applied to obtain the mean-flow momentum equation

$\mathscr{M}$ and energy equation $\mathscr{E}$ in similarity form (Stewartson, 1964)

$$\mathscr{M}\rceil \quad \left(\frac{\mu F''}{T}\right)' + FF'' = 0, \tag{3.3}$$

$$\mathscr{E}\rfloor \quad \left(\frac{\mu T'}{\mathtt{Pr}T}\right)' + \mathtt{M}^2(\gamma-1)\frac{\mu F''^2}{T} + FT' = 0, \tag{3.4}$$

where we have introduced the compressible Blasius function $F = F(\eta)$, the temperature $T = T(\eta)$, and the dynamic viscosity $\mu(T) = T^{\omega}$, where $\omega = 0.76$ (Stewartson, 1964). The prime $'$ indicates the derivative with respect to the independent similarity variable $\eta = \bar{Y}/(2\hat{x})^{1/2}$, where $\bar{Y}(\hat{x}, y) = \int_0^y 1/T(\hat{x}, \bar{y})\mathrm{d}\bar{y}$. The Prandtl number, assumed to be constant, is $\mathtt{Pr} = 0.707$. The boundary conditions for (3.3) and (3.4) are

$$\eta = 0\rceil \quad F = F' = 0, \qquad T' = 0, \tag{3.5}$$

$$\eta \to \infty\rfloor \quad F' \to 1, \qquad T \to 1. \tag{3.6}$$

The streamwise velocity U and the wall-normal velocity V of the mean flow are

$$U = F', \qquad V = \frac{T(\eta_c F' - F)}{\mathtt{R}(2\hat{x})^{1/2}}, \tag{3.7}$$

where $\eta_c(\eta) = T^{-1}\int_0^{\eta} T(\hat{\eta})\mathrm{d}\hat{\eta}$ (Stewartson, 1964).

3.2 The compressible boundary-region equations

The theoretical framework used herein is a combination of the work of Wu et al. (2011) on incompressible Görtler flows over concave surfaces with the work of Ricco and Wu (2007) on compressible Klebanoff modes over flat surfaces. Both papers are extensions of the original theory proposed by Leib et al. (1999) for the incompressible flat-plate case.

Before introducing the boundary-region equations with curvature effects it is instructive to discuss the different asymptotic flow regions, represented in figure 3.1. The flow domain is divided in five main regions: region FS (free stream) for which $x^2 + y^2 \gg 1$, and regions I,

II, III, and IV. Goldstein (1978) developed an analytic framework for the description of the free-stream vortical disturbances in region I. Here, the external disturbances are described as a superposition of inviscid harmonic vortical disturbances which, in the limit $\varepsilon \ll 1$, can be analyzed separately due to the linearity of the problem. As the free-stream vortical disturbances evolve further downstream, the outer flow enters region IV where the mean flow is also inviscid. Here, the displacement effect caused by the boundary-layer growth and the energy decay due to viscous dissipation are analytically treated (Leib et al., 1999). The dynamics of the flow disturbance in these outer regions causes the origin and growth of the perturbation in the viscous regions II and III inside the boundary layer. The method of matched asymptotic expansion is used to link the outer regions I and IV with the boundary-layer regions II and III. Region II is governed by the linearized unsteady boundary-layer equations, i.e., the linearized unsteady boundary-region (LUBR) equations with the spanwise diffusion and normal pressure gradient terms neglected. Originally introduced by Kemp (1951), the LUBR equations are the full Navier-Stokes and continuity equations with the terms pertaining to the streamwise viscous diffusion and the streamwise pressure gradient neglected. This is a rigorous simplification that follows directly from the assumptions $\mathrm{R} \to \infty$ and $k_x \to 0$. Gulyaev et al. (1989), Choudhari (1996), and Leib et al. (1999) recognized that the linearized unsteady boundary-layer equations are appropriate only in a small region near the leading edge where the spanwise wavelength λ_z^* is much larger than the boundary-layer thickness $\delta^* = \mathscr{O}((x^* \nu_\infty^* / U_\infty^*)^{1/2})$. As the boundary layer grows to a thickness comparable with the spanwise wavelength, i.e., $\delta^* = \mathscr{O}(\lambda_z^*)$, the spanwise diffusion terms become of the same order of the wall-normal diffusion terms. This occurs in region III, where the Klebanoff modes in the flat-plate case and the Görtler vortices for flows over concave surfaces are fully developed. The LUBR equations, complemented by rigorous initial and free-stream boundary conditions, must therefore be used to study the flow in region III. The boundary-layer perturbations are assumed to be periodic in time t and along the spanwise direction z. They are expressed as in Gulyaev et al. (1989),

$$\check{\mathbf{q}}(\mathbf{x},t) = ik_z\check{w}\left\{\mathrm{R}\bar{u},\, (2\hat{x})^{1/2}\bar{v},\, \frac{1}{ik_z}\bar{w},\, \frac{1}{\mathrm{R}}\bar{p},\, \mathrm{R}\bar{\tau}\right\} e^{i(k_z z - k_x \mathrm{R}\hat{t})} + \text{c.c.}, \tag{3.8}$$

where $\check{w} \equiv \hat{w}^{\infty} + ik_z\hat{v}^{\infty}(k_x^2+k_z^2)^{-1/2}$ and $\bar{\mathbf{q}}(\hat{x},\eta) = \{\bar{u},\bar{v},\bar{w},\bar{p},\bar{\tau}\}(\hat{x},\eta)$. Equation (3.25) represent the three-dimensional part of the disturbance in which the periodicity of the spanwise direction and time is included in the exponential term, and the term $\check{w}$ comes from the matching with the oncoming flow field. Starting from the full compressible continuity and Navier-Stokes equations in curvilinear coordinates, using the Lamé coefficients and the scaling previously introduced, we find the perturbation equations. The mean flow (3.7) and perturbations (3.8) are then introduced into the equations of motion. Finally, taking the limits $\mathtt{R}\to\infty$ and $k_x\to 0$ with $k_x\mathtt{R} = \mathscr{O}(1)$, the LUBR equations are obtained:

$$\mathscr{C}] \quad \frac{\eta_c}{2\hat{x}}\frac{T'}{T}\bar{u} + \frac{\partial\bar{u}}{\partial\hat{x}} - \frac{\eta_c}{2\hat{x}}\frac{\partial\bar{u}}{\partial\eta} - \frac{T'}{T^2}\bar{v} + \frac{1}{T}\frac{\partial\bar{v}}{\partial\eta} + \bar{w} + \left(ik_x\mathtt{R}\frac{1}{T} - \frac{1}{2\hat{x}}\frac{FT'}{T^2}\right)\bar{\tau} - \frac{F'}{T}\frac{\partial\bar{\tau}}{\partial\hat{x}} + \frac{1}{2\hat{x}}\frac{F}{T}\frac{\partial\bar{\tau}}{\partial\eta} = 0, \tag{3.9}$$

$$\mathscr{X}] \quad \left(-ik_x\mathtt{R} - \frac{\eta_c}{2\hat{x}}F'' + k_z^2\mu T\right)\bar{u} + F'\frac{\partial\bar{u}}{\partial\hat{x}} - \frac{1}{2\hat{x}}\left(F + \frac{\mu'T'}{T} - \frac{\mu T'}{T^2}\right)\frac{\partial\bar{u}}{\partial\eta} - \frac{1}{2\hat{x}}\frac{\mu}{T}\frac{\partial^2\bar{u}}{\partial\eta^2} + \frac{F''}{T}\bar{v} + \frac{1}{2\hat{x}T}\left(FF'' - \mu''F''T' + \frac{\mu'F''T'}{T} - \mu'F'''\right)\bar{\tau} - \frac{1}{2\hat{x}}\frac{\mu'F''}{T}\frac{\partial\bar{\tau}}{\partial\eta} = 0, \tag{3.10}$$

$$\begin{aligned}\mathscr{Y}] \quad & \frac{1}{4\hat{x}^2}\left[\eta_c\left(FT' - F'T\right) - \eta_c^2F''T + FT\right]\bar{u} + \frac{\mu'T'}{3\hat{x}}\frac{\partial\bar{u}}{\partial\hat{x}} - \frac{\mu}{6\hat{x}}\frac{\partial^2\bar{u}}{\partial\hat{x}\partial\eta} + \frac{\eta_c\mu}{12\hat{x}^2}\frac{\partial^2\bar{u}}{\partial\eta^2} + \\ & \frac{1}{12\hat{x}^2}\left(\eta_c\mu'T' + \mu - \frac{\eta_c\mu T'}{T}\right)\frac{\partial\bar{u}}{\partial\eta} + \left[\frac{1}{2\hat{x}}\left(F' + \eta_cF'' - \frac{FT'}{T}\right) - ik_x\mathtt{R} + k_z^2\mu T\right]\bar{v} + \\ & F'\frac{\partial\bar{v}}{\partial\hat{x}} + \frac{1}{\hat{x}}\left[\frac{2}{3T}\left(\frac{\mu T'}{T} - \mu'T'\right) - \frac{F}{2}\right]\frac{\partial\bar{v}}{\partial\eta} - \frac{2}{3\hat{x}}\frac{\mu}{T}\frac{\partial^2\bar{v}}{\partial\eta^2} + \frac{\mu'T'}{3\hat{x}}\bar{w} - \frac{\mu}{6\hat{x}}\frac{\partial\bar{w}}{\partial\eta} + \frac{1}{2\hat{x}}\frac{\partial\bar{p}}{\partial\eta} + \\ & \left[\frac{1}{3\hat{x}^2T}\left(\mu''FT'^2 - \frac{\mu'FT'^2}{T} + \mu'FT'' + \mu'F'T'\right) - \frac{1}{4\hat{x}^2}\left(F'F - \eta_cF'^2 - \eta_cFF'' + \right.\right. \\ & \left.\left.\frac{F^2T'}{T} + \mu'F'' + \eta_c\mu''F''T' - \frac{\eta_c\mu'F''T'}{T} + \eta_cF'''\mu'\right)\right]\bar{\tau} + \frac{\mu'}{\hat{x}^2}\left(\frac{FT'}{3T} - \frac{\eta_cF''}{4}\right)\frac{\partial\bar{\tau}}{\partial\eta} - \\ & \frac{\mu'F''}{2\hat{x}}\frac{\partial\bar{\tau}}{\partial\hat{x}} + \boxed{\frac{\mathtt{G}}{(2\hat{x})^{1/2}}\left(2F'\bar{u} - \frac{F'^2}{T}\bar{\tau}\right)} = 0,\end{aligned} \tag{3.11}$$

$$\mathscr{Z}| \quad -\frac{k_z^2\eta_c\mu' TT'}{2\hat{x}}\bar{u}+\frac{k_z^2\mu T}{3}\frac{\partial\bar{u}}{\partial\hat{x}}-\frac{k_z^2\eta_c\mu T}{6\hat{x}}\frac{\partial\bar{u}}{\partial\eta}+k_z^2\mu' T'\bar{v}+\frac{k_z^2\mu}{3}\frac{\partial\bar{v}}{\partial\eta}+$$
$$\left(\frac{4}{3}k_z^2\mu T-ik_x\mathtt{R}\right)\bar{w}+F'\frac{\partial\bar{w}}{\partial\hat{x}}+\frac{1}{2\hat{x}}\left(\frac{\mu T'}{T^2}-F-\frac{\mu' T'}{T}\right)\frac{\partial\bar{w}}{\partial\eta}-\frac{1}{2\hat{x}}\frac{\mu}{T}\frac{\partial^2\bar{w}}{\partial\eta^2}-$$
$$k_z^2T\bar{p}+\frac{k_z^2}{3\hat{x}}\mu' FT'\bar{\tau}=0, \tag{3.12}$$

$$\mathscr{E}\rfloor \quad -\frac{\eta_c}{2\hat{x}}T'\bar{u}+\frac{T'}{T}\bar{v}+\left[\frac{FT'}{2\hat{x}T}-ik_x\mathtt{R}+\frac{k_z^2\mu T}{\mathtt{Pr}}-\frac{1}{2\hat{x}\mathtt{Pr}}\frac{\partial}{\partial\eta}\left(\frac{\mu' T'}{T}\right)\right]\bar{\tau}+F'\frac{\partial\bar{\tau}}{\partial\hat{x}}+$$
$$\frac{1}{2\hat{x}}\left(\frac{\mu T'}{\mathtt{Pr}T^2}-F-\frac{2\mu' T'}{\mathtt{Pr}T}\right)\frac{\partial\bar{\tau}}{\partial\eta}-\frac{1}{2\hat{x}\mathtt{Pr}}\frac{\mu}{T}\frac{\partial^2\bar{\tau}}{\partial\eta^2}-\mathtt{M}^2\frac{\gamma-1}{\hat{x}T}\left(\mu F''\frac{\partial\bar{u}}{\partial\eta}+\frac{\mu' F''^2}{2}\bar{\tau}\right)=0, \tag{3.13}$$

where $\mathscr{C}$, $\mathscr{X}$, $\mathscr{Y}$, $\mathscr{Z}$, $\mathscr{E}$ indicate the continuity, x-momentum, y-momentum, z-momentum, and energy equations. In these equations the prime $'$ represents differentiation with respect to the independent variable (η or T). The equations of Ricco and Wu (2007) for the compressible flow over a flat surface and of Wu et al. (2011) for the incompressible flow over a concave surface are recovered by setting $\mathtt{G}=0$ and $\mathtt{M}=0$, respectively. Curvature effects derive from the centrifugal force and only appear in the convective terms of the $\mathscr{Y}$ equation (3.11). These terms, boxed in (3.11), are proportional to the Görtler number $\mathtt{G}$ and, in the compressible case, also include the temperature perturbation (El-Hady and Verma, 1983; Hall and Malik, 1989). The LUBR equations are parabolic along the streamwise direction and are influenced by $\mathtt{G}$, k_y, $k_x\mathtt{R}$, and $\mathtt{M}$, which account for the effects of curvature, ratio of the free-stream spanwise wavelength to the wall-normal wavelength, frequency, and compressibility, respectively.

The streamwise velocity $\bar{u}$ and the temperature perturbation $\bar{\tau}$ inside the boundary layer tend to zero as the free stream is approached because they amplify inside the boundary layer to an order of magnitude larger than the corresponding free-stream disturbances (Ricco and Wu, 2007). Therefore, the boxed curvature terms in (3.11) can be neglected as $\eta\to\infty$ and

we recover the free-stream boundary conditions used by Ricco and Wu (2007):

$$\eta = 0\rceil \quad \bar{u} = \bar{v} = \bar{w} = \frac{\partial \bar{\tau}}{\partial \eta} = 0, \tag{3.14}$$

$$\eta \to \infty\rfloor \quad \bar{u} \to 0, \tag{3.15}$$

$$\frac{\partial \bar{v}}{\partial \eta} + |k_z|(2\hat{x})^{1/2}\bar{v} \to -e^{i[k_x \mathrm{R}\hat{x} + k_y(2\hat{x})^{1/2}(\eta - \beta_c)] - \left(k_y^2 + k_z^2\right)\hat{x}}, \tag{3.16}$$

$$\frac{\partial \bar{w}}{\partial \eta} + |k_z|(2\hat{x})^{1/2}\bar{w} \to ik_y(2\hat{x})^{1/2} e^{i[k_x \mathrm{R}\hat{x} + k_y(2\hat{x})^{1/2}(\eta - \beta_c)] - \left(k_y^2 + k_z^2\right)\hat{x}}, \tag{3.17}$$

$$\frac{\partial \bar{p}}{\partial \eta} + |k_z|(2\hat{x})^{1/2}\bar{p} \to 0, \tag{3.18}$$

$$\bar{\tau} \to 0, \tag{3.19}$$

where compressibility effects are taken into account by the parameter $\beta_c(\mathtt{M}) \equiv \lim_{\eta \to \infty}(\eta - F)$, which is computed numerically (Ricco et al., 2009). These boundary conditions are derived based on the matching between the inner boundary layer flow and the outer flow. Since curvature effects are also negligible in the limit $\hat{x} \to 0$, the initial conditions of Ricco and Wu (2007) apply:

$$\hat{x} \to 0\rceil \quad \bar{u} \to 2\hat{x}U_0 + (2\hat{x})^{3/2}U_1, \tag{3.20}$$

$$\bar{v} \to V_0 + (2\hat{x})^{1/2}V_1 - \left[V_c - \frac{1}{2}g_1|k_z|(2\hat{x})^{1/2}\right] e^{-|k_z|(2\hat{x})^{1/2}\bar{\eta}} + \frac{i}{(k_y - i|k_z|)(2\hat{x})^{1/2}}\left[e^{ik_y(2\hat{x})^{1/2}\bar{\eta} - \left(k_y^2 + k_z^2\right)\hat{x}} - e^{-|k_z|(2\hat{x})^{1/2}\bar{\eta}}\right] - \bar{v}_c, \tag{3.21}$$

$$\bar{w} \to W_0 + (2\hat{x})^{1/2}W_1 - V_c|k_z|(2\hat{x})^{1/2} e^{-|k_z|(2\hat{x})^{1/2}\bar{\eta}} + \frac{1}{k_y - i|k_z|}\left[k_y e^{ik_y(2\hat{x})^{1/2}\bar{\eta} - \left(k_y^2 + k_z^2\right)\hat{x}} - i|k_z|e^{-|k_z|(2\hat{x})^{1/2}\bar{\eta}}\right] - \bar{w}_c, \tag{3.22}$$

$$\bar{p} \to \frac{P_0}{(2\hat{x})^{1/2}} + P_1 + \left[g_1 - \frac{V_c}{|k_z|(2\hat{x})^{1/2}}\right] e^{-|k_z|(2\hat{x})^{1/2}\bar{\eta}} - \bar{p}_c, \tag{3.23}$$

$$\bar{\tau} \to 2\hat{x}T_0 + (2\hat{x})^{3/2}T_1, \tag{3.24}$$

where $\bar{\eta} \equiv \eta - \beta_c$. The common parts $\bar{v}_c$, $\bar{w}_c$, and $\bar{p}_c$, the constants g_1 and V_c, and the solutions U_0, V_0, W_0, P_0, T_0, U_1, V_1, W_1, P_1, T_1 are derived in Appendix B. The numerical procedure for solving the LUBR equations is described in Appendix A. The significance of receptivity can be emphasized by noting that k_y only influences the solution through the initial and boundary conditions. This is because the LUBR equations (3.9)-(3.13) do not include k_y as a parameter.

3.2.1 Neutral curve parameters

In early studies (Hall, 1990), the abscissa and ordinate of neutral curves associated to the Görtler instability were represented with a scaled spanwise wavenumber and a scaled Görtler number, using the boundary-layer thickness as the characteristic length. Translated into our scaling, the neutral curves would be plotted in a $\mathscr{X}$-$\mathscr{G}$ plane, with the abscissa being $\mathscr{X} = (2\hat{x})^{1/2}$ and the ordinate $\mathscr{G} = \mathtt{G}\mathscr{X}^3/\sqrt{2}$. However, the neutral curves would collapse on a $\mathscr{X}^3$ curve and the behavior of the flow would not be revealed, particularly in the vicinity of the leading edge. We found that our neutral curves are better represented in an $\hat{x}$-$\mathtt{G}$ plane in order to demonstrate the connection between Klebanoff modes, Görtler vortices and stability of the flow as the values of $k_x\mathtt{R}$, k_y and $\mathtt{M}$ are changed.

Two parameters are introduced to represent the neutral curves:

$$\varsigma(\hat{x}) \equiv \frac{\mathrm{dE}(\hat{x})}{\mathrm{d}\hat{x}}, \qquad \beta(\hat{x}) \equiv \frac{\mathrm{d}^2|\bar{u}(\hat{x})|_{\max}}{\mathrm{d}\hat{x}^2}, \tag{3.25}$$

where $\mathtt{E}(\hat{x}) \equiv \int_0^\infty |\bar{u}(\hat{x},\eta)|^2 \mathrm{d}\eta$ is the perturbation energy scaled by $(2\hat{x})^{1/2}$ (Hall, 1990) and $|\bar{u}(\hat{x})|_{\max} \equiv \max_\eta |\bar{u}(\hat{x},\eta)|$ is the maximum value of the streamwise velocity perturbation amplitude along $\eta = y/(2\hat{x})^{1/2}$. The parameter β is here introduced to identify the streamwise location where the perturbation shift from Klebanoff modes to Görtler vortices. By defining $\varsigma(\hat{x})$ in this manner the information from the amplitude of the perturbation is retained, which is of particular importance for a receptivity analysis. If we had normalized the parameter $\varsigma(\hat{x})$ by the energy $\mathtt{E}(\hat{x})$, as in Hall (1990), we would have lost the information of the perturbation amplitude. The scaled perturbation energy in (3.25) is computed with the $|\bar{u}|$ velocity alone

as, when Görtler vortices are present, the physical transverse velocities are much smaller than the physical streamwise velocity (Wu et al., 2011).

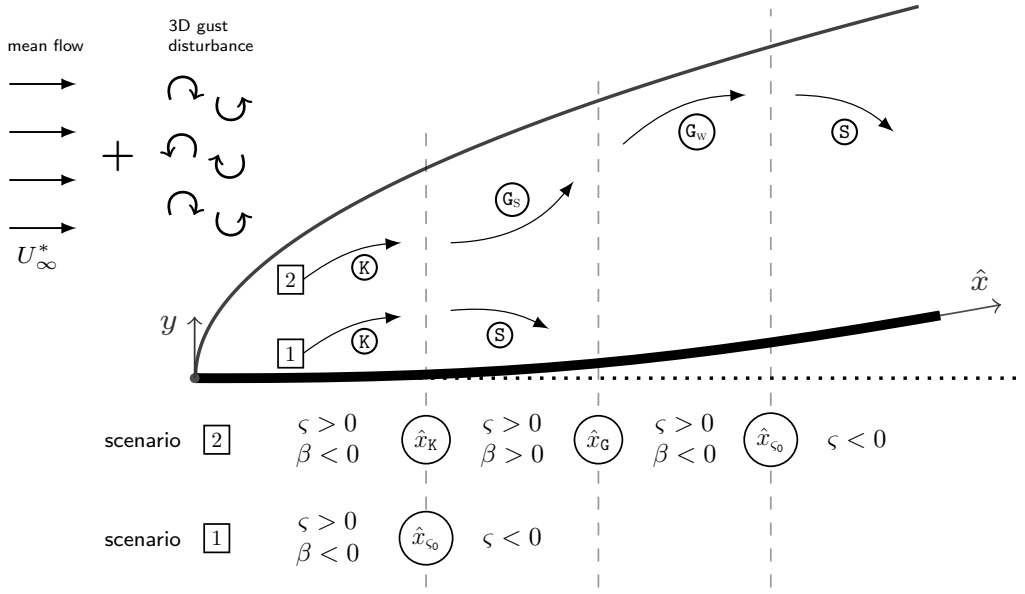

Fig. 3.2 Sketch of the boundary layer representing K-vortices (K), Görtler vortices with strong growth (G_S), Görtler vortices with weak growth (G_W), and stable flows (S) through the two parameters ς and β defined in (3.25). A typical scenario for $G < G_B = 10.9$ and for $G > G_C = 17$ are represented by 1 and 2, respectively, for a steady flow.

The instabilities can be classified based on (3.25) as shown in figure 3.2. When $\varsigma < 0$ the flow is stable whereas it is unstable when $\varsigma > 0$. The neutral points, located at $\hat{x} = \hat{x}_{\varsigma_0}$, are associated to $\varsigma = 0$. In the proximity of the leading edge, curvature effects do not play any role. As a consequence, the boundary layer perturbations start growing as Klebanoff modes, herein labelled K-vortices (K), associated to $\varsigma > 0$ and $\beta < 0$. As G, k_y, M and k_xR change, the K-vortices can stabilize downstream of $\hat{x} = \hat{x}_{\varsigma_0}$ or shift into Görtler vortices for $\hat{x} = \hat{x}_K$. This last location is associated with $\beta'(\hat{x}) > 0$ and $\beta = 0$, where the prime indicates the derivative with respect to $\hat{x}$. Initially, the growth of the Görtler vortices is characterized by $\beta > 0$, classified as strong growth and identified by (G_S) (G_S-vortices). Downstream of $\hat{x} = \hat{x}_G$, the location with the maximum local growth rate, the growth of Görtler vortices, characterized by $\beta < 0$, weakens (G_W-vortices, (G_W)) with $\beta = 0$ and $\beta' < 0$. Finally, stability is reached for $\hat{x} > \hat{x}_{\varsigma_0}$.

3.3 The eigenvalue equations

Because of the inviscid unbalance between the centrifugal force and the wall-normal pressure, the Görtler instability exhibits an exponential streamwise amplification. Following the work of Wu et al. (2011), we can take advantage of this property by adopting a simplified mathematical framework based on an additional decomposition of the quantities defined in (3.8),

$$\bar{\mathbf{q}}(\hat{x},\eta) = \{\bar{u},\bar{v},\bar{w},\bar{p},\bar{\tau}\} \equiv \widetilde{\mathbf{q}}(\eta)\, e^{\int^{\hat{x}} \sigma_{\text{EV}}(x)\mathrm{d}x}, \tag{3.26}$$

where $\widetilde{\mathbf{q}} = \{\widetilde{u},\widetilde{v},\widetilde{w},\widetilde{p},\widetilde{\tau}\}$ and $\sigma_{\text{EV}} = \sigma_{\text{EV, Re}} + i\sigma_{\text{EV, Im}}$ is a complex function whose real part $\sigma_{\text{EV, Re}}(\hat{x})$ is the local growth rate and the imaginary part $\sigma_{\text{EV, Im}}(\hat{x})$ is proportional to the streamwise wavenumber of the boundary-layer perturbation, i.e.,

$$k_{x,\,\text{EV}}(\hat{x}) = \frac{1}{\hat{x}} \int^{\hat{x}} \sigma_{\text{EV}}(x)\mathrm{d}x. \tag{3.27}$$

Expression (3.26) is a local eigenvalue (EV) decomposition, i.e., valid at a specified streamwise location, which implies that the streamwise dependence of the perturbation is absorbed in $\sigma(\hat{x})$, while the wall-normal variation is distilled in $\widetilde{\mathbf{q}}(\eta)$. The EV perturbation (3.26) is only defined to within an undetermined amplitude which can only be found through the receptivity analysis, i.e., by accounting for the influence of the free-stream disturbance. Nevertheless, the EV approach has the advantage of identifying the streamwise locations where the perturbation exhibits exponential growth and where its growth rate and streamwise length scale are not influenced by the initial and free-stream boundary conditions.

By substituting (3.26) into (3.9)-(3.13) we obtain the non-parallel EV system of equations, which preserves the growing nature of the boundary-layer mean flow. The equations can be further simplified by invoking the η-based parallel mean-flow assumption, which implies $V = 0$, and by taking the limit $\hat{x} \gg 1$ (Wu et al., 2011). This work is intended to show the results of both the parallel and non-parallel assumptions. For numerical reasons, the system of ordinary differential equations (ODE) is written as a system of first order equations by

introducing three new variables,

$$\widetilde{f}(\eta) \equiv \frac{\partial \widetilde{u}}{\partial \eta}, \qquad \widetilde{g}(\eta) \equiv \frac{\partial \widetilde{w}}{\partial \eta}, \qquad \widetilde{h}(\eta) \equiv \frac{\partial \widetilde{\tau}}{\partial \eta}. \tag{3.28}$$

The non-parallel compressible EV equations are given in the following, where the terms between $\langle\,\rangle$ can be neglected under the parallel flow assumption because they arise from the wall-normal velocity V given in (3.7).

$$\mathscr{C}\rceil \quad \frac{\partial \widetilde{v}}{\partial \eta} = \left(\sigma F' - ik_x \mathtt{R}\right)\widetilde{\tau} - \sigma T \widetilde{u} + \widetilde{v}\frac{T'}{T} - T\widetilde{w} + \left\langle \frac{FT'}{2\hat{x}T}\widetilde{\tau} - \frac{\eta_c}{2\hat{x}}T'\widetilde{u} - \frac{F}{2\hat{x}}\widetilde{h} + \frac{\eta_c T}{2\hat{x}}\widetilde{f} \right\rangle, \tag{3.29}$$

$$\begin{aligned}\mathscr{X}|\quad \frac{\partial \widetilde{f}}{\partial \eta} = {} & \left(-ik_x\mathtt{R}\frac{2\hat{x}T}{\mu} + 2\hat{x}\sigma\frac{F'T}{\mu} + 2\hat{x}k_z^2T^2\right)\widetilde{u} - \frac{F''\mu'}{\mu}\widetilde{h} + \frac{2\hat{x}F''}{\mu}\widetilde{v} - \left(\frac{\mu'T'}{\mu} - \frac{T'}{T}\right)\widetilde{f} + \\ & \left(\frac{\mu'F''T'}{\mu T} - \frac{\mu''F''T'}{\mu} - \frac{\mu'F'''}{\mu}\right)\widetilde{\tau} + \left\langle \frac{FF''}{\mu}\widetilde{\tau} - \frac{\eta_c F''T}{\mu}\widetilde{u} - \frac{FT}{\mu}\widetilde{f} \right\rangle,\end{aligned} \tag{3.30}$$

$$\begin{aligned}\mathscr{Y}|\quad \frac{\partial \widetilde{p}}{\partial \eta} = {} & -\sigma\mu\widetilde{f} - 2\sigma T'\left(\mu' + \frac{2}{3}\frac{\mu}{T}\right)\widetilde{u} + 2\hat{x}\left(ik_x\mathtt{R} - k_z^2\mu T - \sigma F'\right)\widetilde{v} - \mu\widetilde{g} + \\ & \left(F''\mu'\sigma + \frac{4}{3}\frac{\mu'T'F'\sigma}{T} - \frac{4}{3}\frac{\mu F''\sigma}{T} - \frac{4}{3}ik_x\mathtt{R}\frac{\mu'T'}{T}\right)\widetilde{\tau} + \frac{4}{3}\frac{\mu}{T}\left(\sigma F' - ik_x\mathtt{R}\right)\widetilde{h} - \\ & 2T'\left(\mu' + \frac{2}{3}\frac{\mu}{T}\right)\widetilde{w} + (2\hat{x})^{1/2}\mathtt{G}F'\left(\frac{F'}{T}\widetilde{\tau} - 2\widetilde{u}\right) + \left\langle \frac{\mu}{2\hat{x}}\widetilde{f} + \left(- ik_x\mathtt{R}\eta_c T + \right.\right. \\ & \sigma\eta_c F'T + k_z^2\eta_c\mu T^2 - \frac{2\eta_c}{3\hat{x}}\frac{\mu'T'^2}{T} + \frac{2\eta_c}{3\hat{x}}\frac{\mu T'^2}{T^2} - \frac{2}{3\hat{x}}\frac{\mu T'}{T} - \frac{2\eta_c}{3\hat{x}}\frac{\mu T''}{T} + \frac{\eta_c}{2\hat{x}}F'T - \\ & \left.\left.\frac{FT}{2\hat{x}} - \frac{\eta_c FT'}{\hat{x}} - \sigma FT\right)\widetilde{u} + \left(\frac{4}{3}\frac{\mu'T'^2}{T^2} - \frac{4}{3}\frac{\mu T'^2}{T^3} + \frac{4}{3}\frac{\mu T''}{T^2} - F' + 2\frac{FT'}{T}\right)\widetilde{v} + \right. \\ & \left.\left(\frac{\mu'F''}{2\hat{x}} - \frac{2}{3\hat{x}}\frac{\mu''FT'^2}{T} + \frac{4}{3\hat{x}}\frac{\mu'FT'^2}{T^2} - \frac{2}{3\hat{x}}\frac{\mu'FT''}{T} - \frac{2}{3\hat{x}}\frac{\mu'F'T'}{T} - \frac{2}{3\hat{x}}\frac{\mu FT'^2}{T^3} + \right.\right.\end{aligned} \tag{3.31}$$

$$\frac{2}{3\hat{x}}\frac{\mu F'T'}{T^2}+\frac{2}{3\hat{x}}\frac{\mu FT''}{T^2}-ik_x\mathtt{R}F+\sigma FF'+\frac{FF'}{2\hat{x}}+\frac{1}{2\hat{x}}\frac{2F^2T'}{T}-\frac{\eta_c F'^2}{2\hat{x}}\Bigg)\widetilde{\tau}+$$
$$\left(\frac{2}{3\hat{x}}\frac{\mu FT'}{T^2}-\frac{4}{3\hat{x}}\frac{\mu' FT'}{T}-\frac{2}{3\hat{x}}\frac{\mu F'}{T}-\frac{F^2}{2\hat{x}}\right)\widetilde{h}-FT\widetilde{w}-\frac{2}{3\hat{x}}\frac{\mu F}{T}\frac{\partial\widetilde{h}}{\partial\eta}\Bigg\rangle, \tag{3.31}$$

$$\mathscr{L}|\ \frac{\partial\widetilde{g}}{\partial\eta}=2\hat{x}\left(-\frac{ik_x\mathtt{R}T}{\mu}+\frac{\sigma F'T}{\mu}+k_z^2T^2\right)\widetilde{w}+\left(-\frac{\mu'T'}{\mu}+\frac{T'}{T}\right)\widetilde{g}-$$
$$\frac{2\hat{x}k_z^2T^2}{\mu}\widetilde{p}+2\hat{x}k_z^2\left(\frac{\mu'T'T}{\mu}+\frac{T'}{3}\right)\widetilde{v}+\frac{2\hat{x}k_z^2}{3}T\left(-ik_x\mathtt{R}+F'\sigma\right)\widetilde{\tau}+$$
$$\left\langle\frac{FT'}{3}\left(1+\frac{2\mu'T}{\mu}\right)\widetilde{\tau}-\frac{FT}{\mu}\widetilde{g}-k_z^2\eta_cT'T\left(\frac{\mu'T}{\mu}+\frac{1}{3}\right)\widetilde{u}-\frac{k_z^2FT}{3}\widetilde{h}\right\rangle, \tag{3.32}$$

$$\mathscr{E}\rfloor\ \frac{\partial\widetilde{h}}{\partial\eta}=T'\left(-\frac{2\mu'}{\mu}+\frac{1}{T}\right)\widetilde{h}+\frac{2\hat{x}\mathtt{Pr}T'}{\mu}\widetilde{v}-2(\gamma-1)\mathtt{M}^2\mathtt{Pr}F''\widetilde{f}+$$
$$2\hat{x}T\left(-\frac{ik_x\mathtt{RPr}}{\mu}+\frac{\sigma\mathtt{Pr}F'}{\mu}+k_z^2T\right)\widetilde{\tau}+\Bigg\langle\frac{1}{\mu}\Bigg[\mathtt{Pr}FT'-(\gamma-1)\mathtt{M}^2\mathtt{Pr}\mu'F''^2-$$
$$T\frac{\partial}{\partial\eta}\left(\frac{\mu'T'}{T}\right)\Bigg]\widetilde{\tau}-\frac{\eta_c\mathtt{Pr}T'T}{\mu}\widetilde{u}-\frac{\mathtt{Pr}FT}{\mu}\widetilde{h}\Bigg\rangle. \tag{3.33}$$

The EV system (3.29)-(3.33) is solved with homogeneous boundary conditions: $\widetilde{u}=\widetilde{v}=\widetilde{w}=\widetilde{\tau}=0$ at $\eta=0$ and $\widetilde{u},\widetilde{v},\widetilde{w},\widetilde{\tau}\to 0$ as $\eta\to\infty$. For $\mathtt{M}=0$, the equations of Wu et al. (2011) for the incompressible case are recovered. The numerical procedure for solving the EV equations is described in Appendix A. This procedure is based on an iterative method that requires an accurate initial guess, and does not compute all the possible eigenvalue that could be computed using a global procedure.

3.4 Asymptotic equations

In most experiments where flows over concave surfaces have been investigated in incompressible and compressible conditions, the Görtler number has been larger than 10^2. This

motivated Wu et al. (2011) to study the asymptotic limit $\mathtt{G} \to \infty$, which revealed the necessary conditions for the inviscid instability and the different stages of the evolution of the incompressible Görtler vortices. We herein extend the analysis of Wu et al. (2011) to the compressible case with $\mathtt{M} = \mathscr{O}(1)$. A summary of the physical results extracted through the asymptotic analysis of this section is given in §3.4.5 on page 44. Even though this theoretical analysis unveils crucial physical characteristics which are not revealed by a purely numerical approach, it will become evident that the numerical solution of the LUBR equations is nevertheless needed for a thorough understanding of the flow and for its accurate computation, especially for $\mathtt{G} = \mathscr{O}(1)$, where the asymptotic analysis is invalid.

Figure 3.3 shows the different streamwise stages through which the perturbation evolves in the limit $\mathtt{G} \gg 1$. In this limit we can identify four main layers, namely the main layer ML,

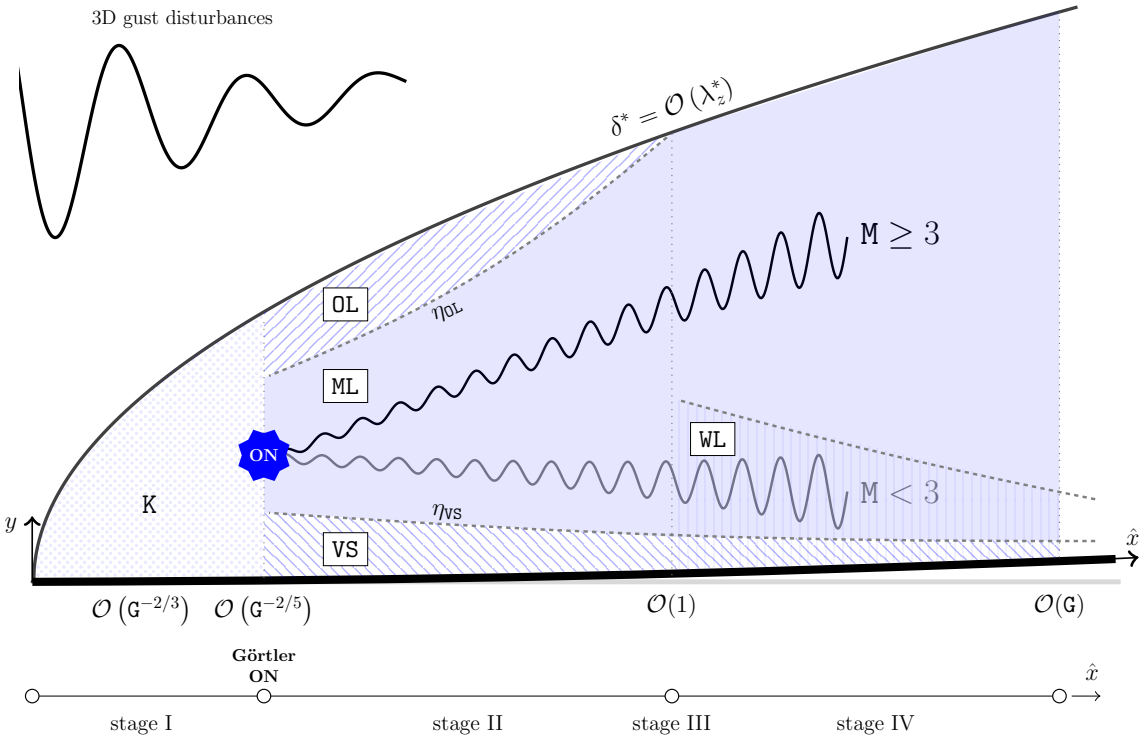

Fig. 3.3 Sketch of the boundary-layer asymptotic stages for $\mathtt{G} \to \infty$: Klebanoff modes K, main layer ML, viscous sublayer VS, outer layer OL and wall layer WL.

the outer layer OL, the viscous sublayer VS, and the wall layer WL.

3.4.1 Stage I. Pre-modal regime: $\hat{x} \leq \mathtt{G}^{-2/5}$

We first consider the region in the proximity of the leading edge, i.e., $\hat{x} \ll 1$, where the power-series expansion (B.7) is valid. By assuming that $\bar{w} = \mathscr{O}(1)$, $\eta = \mathscr{O}(1)$, $\eta_c = \mathscr{O}(1)$, and $T, T', F, F' = \mathscr{O}(1)$, an order of magnitude analysis of the terms in the $\mathscr{C}$ equation (3.9) leads to

$$\bar{u} = \mathscr{O}(\hat{x}), \qquad \bar{\tau} = \mathscr{O}(\hat{x}), \qquad \bar{v} = \mathscr{O}(1). \tag{3.34}$$

The terms of the $\mathscr{Y}$ equation (3.11) become of order

$$\underbrace{\mathscr{O}(1)}_{\text{unsteadiness}} + \underbrace{\mathscr{O}\left(\frac{1}{\hat{x}}\right)}_{\text{inertia}} + \underbrace{\mathscr{O}\left(\hat{x}^{1/2}\mathtt{G}\right)}_{\text{curvature}} = \underbrace{\frac{P_0'(\eta)}{(2\hat{x})^{3/2}}}_{\eta \text{ pressure gradient}} + \underbrace{\mathscr{O}\left(\frac{1}{\hat{x}}\right)}_{\text{diffusion}}, \tag{3.35}$$

by using the power-series expansion (B.7) for the pressure. When $\hat{x} \ll \mathtt{G}^{-2/3}$, the equations are steady and the curvature effects are negligible compared to the other terms. Therefore, the perturbation evolves as flat-plate Klebanoff modes, denoted by the letter K in figure 3.3, and the wall-normal gradient of the pressure perturbation is negligible because the term dominates as $\hat{x} \ll 1$. Further downstream where $\hat{x} = \mathscr{O}\left(\mathtt{G}^{-2/3}\right)$, curvature effects start to influence the other terms, including the pressure field, rendering the asymptotic series expansion (B.7) invalid. The gradient of the pressure $\overline{p}$ along η grows to an order-one magnitude as it balances the centrifugal term. Substituting the scaled variables

$$x^\dagger = \hat{x}\,\mathtt{G}^{2/3}, \qquad u^\dagger = \bar{u}\,\mathtt{G}^{2/3}, \qquad \tau^\dagger = \bar{\tau}\,\mathtt{G}^{2/3}, \tag{3.36}$$

into (3.9)-(3.13) and neglecting terms $\ll 1$, the perturbation field is described by

$$\begin{aligned}\mathscr{C}\rceil\ & \frac{\eta_c}{2x^\dagger}\frac{T'}{T}u^\dagger + \frac{\partial u^\dagger}{\partial x^\dagger} - \frac{\eta_c}{2x^\dagger}\frac{\partial u^\dagger}{\partial \eta} - \frac{T'}{T^2}\bar{v} + \frac{1}{T}\frac{\partial \bar{v}}{\partial \eta} - \frac{FT'}{2x^\dagger T^2}\tau^\dagger - \frac{F'}{T}\frac{\partial \tau^\dagger}{\partial x^\dagger} + \\ & \frac{F}{2x^\dagger T}\frac{\partial \tau^\dagger}{\partial \eta} + \bar{w} = 0,\end{aligned} \tag{3.37}$$

$$\mathscr{X}\rfloor\ -\frac{\eta_c}{2x^\dagger}F''u^\dagger+F'\frac{\partial u^\dagger}{\partial x^\dagger}+\frac{1}{2x^\dagger}\left(\frac{\mu T'}{T^2}-F-\frac{\mu' T'}{T}\right)\frac{\partial u^\dagger}{\partial\eta}-\frac{\mu}{2x^\dagger T}\frac{\partial^2 u^\dagger}{\partial\eta^2}+\frac{F''}{T}\bar{v}+$$
$$\frac{1}{2x^\dagger T}\left(FF''-\mu''F''T'+\frac{\mu' F''T'}{T}-\mu' F'''\right)\tau^\dagger-\frac{\mu' F''}{2x^\dagger T}\frac{\partial\tau^\dagger}{\partial\eta}=0, \tag{3.38}$$

$$\mathscr{Z}\rfloor\ F'\frac{\partial\bar{w}}{\partial x^\dagger}+\frac{1}{2x^\dagger}\left(\frac{\mu T'}{T^2}-F-\frac{\mu' T'}{T}\right)\frac{\partial\bar{w}}{\partial\eta}-\frac{\mu}{2x^\dagger T}\frac{\partial^2\bar{w}}{\partial\eta^2}=0, \tag{3.39}$$

$$\mathscr{E}\rfloor\ -\frac{\eta_c T'}{2x^\dagger}u^\dagger-\mathtt{M}^2\frac{(\gamma-1)}{x^\dagger}\frac{\mu F''}{T}\frac{\partial u^\dagger}{\partial\eta}+\frac{T'}{T}\bar{v}+\frac{1}{2x^\dagger}\left[\frac{FT'}{T}-\mathtt{M}^2(\gamma-1)\frac{\mu' F''^2}{T}-\right.$$
$$\left.\frac{1}{\mathtt{Pr}}\frac{\partial}{\partial\eta}\left(\frac{\mu' T'}{T}\right)\right]\tau^\dagger+F'\frac{\partial\tau^\dagger}{\partial x^\dagger}+\frac{1}{2x^\dagger}\left(\frac{\mu T'}{\mathtt{Pr}T^2}-F-\frac{2\mu' T'}{\mathtt{Pr}T}\right)\frac{\partial\tau^\dagger}{\partial\eta}-$$
$$\frac{1}{2x^\dagger\mathtt{Pr}}\frac{\mu}{T}\frac{\partial^2\tau^\dagger}{\partial\eta^2}=0. \tag{3.40}$$

It is sufficient to solve $\mathscr{C}$, $\mathscr{X}$, $\mathscr{Z}$, and $\mathscr{E}$ to find the velocity and temperature perturbations. The pressure $\bar{p}$ is solved a posteriori from $\mathscr{Y}$, which reads

$$\mathscr{Y}\rfloor\ \frac{1}{(2x^\dagger)^2}\left[FT-\eta_c F'T-\eta_c^2 F''T+\eta_c FT'+\frac{2F'}{(2x^\dagger)^{1/2}}\right]u^\dagger+\frac{\mu' T'}{3x^\dagger}\frac{\partial u^\dagger}{\partial x^\dagger}-$$
$$\frac{\mu}{6x^\dagger}\frac{\partial^2 u^\dagger}{\partial\eta\partial x^\dagger}+\frac{\eta_c\mu}{12x^{\dagger 2}}\frac{\partial^2 u^\dagger}{\partial\eta^2}+\frac{1}{12x^{\dagger 2}}\left(\eta_c\mu' T'+\mu-\frac{\eta_c\mu T'}{T}\right)\frac{\partial u^\dagger}{\partial\eta}+$$
$$\frac{1}{2x^\dagger}\left(F'+\eta_c F''-\frac{FT'}{T}\right)\bar{v}+F'\frac{\partial\bar{v}}{\partial x^\dagger}+\frac{1}{x^\dagger}\left(\frac{2}{3}\frac{\mu T'}{T^2}-\frac{2}{3}\frac{\mu' T'}{T}-\frac{F}{2}\right)\frac{\partial\bar{v}}{\partial\eta}-\frac{2}{3x^\dagger}\frac{\mu}{T}\frac{\partial^2\bar{v}}{\partial\eta^2}$$
$$+\frac{\mu' T'}{3x^\dagger}\bar{w}-\frac{\mu}{6x^\dagger}\frac{\partial\bar{w}}{\partial\eta}+\frac{1}{2x^\dagger}\frac{\partial\bar{p}}{\partial\eta}+\left[\frac{1}{(2x^\dagger)^2}\left(\eta_c F'^2-FF'+\eta_c FF''-\frac{F^2T'}{T}-\mu' F''-\right.\right.$$
$$\left.\eta_c\mu'' F''T'+\frac{\eta_c\mu' F''T'}{T}-\eta_c\mu' F'''\right)+\frac{1}{3x^{\dagger 2}T}\left(\mu'' T'^2F-\frac{\mu' T'^2F}{T}+\mu' T''F+\right.$$
$$\left.\left.\mu' T'F'\right)-\frac{F'^2}{(2x^\dagger)^{1/2}T}\right]\tau^\dagger-\frac{\mu' F''}{2x^\dagger}\frac{\partial\tau^\dagger}{\partial x^\dagger}+\mu'\left[\frac{T'F}{3x^{\dagger 2}T}-\frac{\eta_c F''}{(2x^\dagger)^2}\right]\frac{\partial\tau^\dagger}{\partial\eta}=0. \tag{3.41}$$

Equation (3.41) is decoupled from the other equations since, in the new scaling (3.36), the pressure term in $\mathscr{Z}$ is negligible, so the flow is governed by the boundary-layer equations, i.e., the effects of the spanwise viscous diffusion and of the spanwise pressure gradient are negligible (although the boundary-layer equations may also apply if a mean spanwise pressure gradient is imposed).

As the flow evolves further downstream we seek the location where the curvature effects begin to influence the perturbation velocity also through the pressure gradient along the z direction in the $\mathscr{Z}$ equation (3.12). The pressure has now grown to an unknown order of magnitude. This is found by balancing the curvature and the pressure terms of the $\mathscr{Y}$ equation (3.11) to obtain $\mathtt{G}\hat{x}^{1/2} \sim \bar{p}/\hat{x}$, hence $\bar{p} = \mathscr{O}\left(\mathtt{G}\,\hat{x}^{3/2}\right)$. The terms of the $\mathscr{Z}$ equation (3.12) become of order

$$\underbrace{\mathscr{O}(1)}_{\text{unsteadiness}} + \underbrace{\mathscr{O}\left(\frac{1}{\hat{x}}\right)}_{\text{inertia}} = \underbrace{\mathscr{O}\left(\mathtt{G}\,\hat{x}^{3/2}\right)}_{\text{pressure}} + \underbrace{\mathscr{O}\left(\frac{1}{\hat{x}}\right)}_{\text{diffusion}}, \tag{3.42}$$

from which it is inferred that the pressure comes into play in the $\mathscr{Z}$ equation when $\hat{x} = \mathscr{O}\left(\mathtt{G}^{-2/5}\right)$. A new scaling can be introduced for $\eta = \mathscr{O}(1)$, as follows

$$\breve{x} = \hat{x}\,\mathtt{G}^{2/5}, \qquad \breve{u} = \bar{u}\,\mathtt{G}^{2/5}, \qquad \breve{\tau} = \bar{\tau}\,\mathtt{G}^{2/5}, \qquad \breve{p} = \bar{p}\,\mathtt{G}^{-2/5}. \tag{3.43}$$

After substitution into the LUBR equations (3.9)-(3.13), the equations of motion become

$$\mathscr{C}] \quad \frac{\eta_c}{2\breve{x}}\frac{T'}{T}\breve{u} + \frac{\partial \breve{u}}{\partial \breve{x}} - \frac{\eta_c}{2\breve{x}}\frac{\partial \breve{u}}{\partial \eta} - \frac{T'}{T^2}\bar{v} + \frac{1}{T}\frac{\partial \bar{v}}{\partial \eta} + \bar{w} - \frac{FT'}{2\breve{x}T^2}\breve{\tau} - \frac{F'}{T}\frac{\partial \breve{\tau}}{\partial \breve{x}} + \frac{F}{2\breve{x}T}\frac{\partial \breve{\tau}}{\partial \eta} = 0, \tag{3.44}$$

$$\begin{aligned}\mathscr{X}] \quad & -\frac{\eta_c F''}{2\breve{x}}\breve{u} + F'\frac{\partial \breve{u}}{\partial \breve{x}} + \frac{1}{2\breve{x}}\left(\frac{\mu T'}{T^2} - \frac{\mu' T'}{T} - F\right)\frac{\partial \breve{u}}{\partial \eta} - \frac{\mu}{2\breve{x}T}\frac{\partial^2 \breve{u}}{\partial \eta^2} + \frac{F''}{T}\bar{v} + \\ & \frac{1}{2\breve{x}T}\left(FF'' - \mu'' F'' T' + \frac{\mu' F'' T'}{T} - \mu' F'''\right)\breve{\tau} - \frac{F''\mu'}{2\breve{x}T}\frac{\partial \breve{\tau}}{\partial \eta} = 0\end{aligned} \tag{3.45}$$

$$\mathscr{Y}| \quad \frac{2F'}{(2\breve{x})^{1/2}}\breve{u}+\frac{1}{2\breve{x}}\frac{\partial \bar{p}}{\partial \eta}-\frac{F'^2}{(2\breve{x})^{1/2}T}\breve{\tau}=0, \tag{3.46}$$

$$\mathscr{Z}| \quad F'\frac{\partial \bar{w}}{\partial \breve{x}}+\frac{1}{2\breve{x}}\left(\frac{\mu T'}{T^2}-F-\frac{\mu' T'}{T}\right)\frac{\partial \bar{w}}{\partial \eta}-\frac{\mu}{2\breve{x}T}\frac{\partial^2 \bar{w}}{\partial \eta^2}-k_z^2 T\breve{p}=0, \tag{3.47}$$

$$\begin{aligned}\mathscr{E}\rfloor \quad & -\frac{\eta_c T'}{2\breve{x}}\breve{u}-\mathtt{M}^2\frac{(\gamma-1)}{\breve{x}}\frac{\mu F''}{T}\frac{\partial \breve{u}}{\partial \eta}+\frac{T'}{T}\bar{v}+F'\frac{\partial \breve{\tau}}{\partial \breve{x}}+\frac{1}{2\breve{x}}\left(\frac{1}{\mathtt{Pr}}\frac{\mu T'}{T^2}-F-\frac{2}{\mathtt{Pr}}\frac{\mu' T'}{T}\right)\frac{\partial \breve{\tau}}{\partial \eta}+\\ & \frac{1}{2\breve{x}}\left[\frac{T'F}{T}-\mathtt{M}^2(\gamma-1)\frac{\mu'}{T}F''^2-\frac{1}{\mathtt{Pr}}\frac{\partial}{\partial \eta}\left(\frac{\mu' T'}{T}\right)\right]\breve{\tau}-\frac{\mu}{2\breve{x}\mathtt{Pr}T}\frac{\partial^2 \breve{\tau}}{\partial \eta^2}=0.\end{aligned} \tag{3.48}$$

In (3.44)-(3.48), the unsteady effects are still negligible and the perturbation is thus steady. Since we know that the Görtler vortices eventually acquire a modal form it can be inferred that, if (3.44)-(3.48) admit an asymptotic eigensolution, $\hat{x}=\mathscr{O}\left(\mathtt{G}^{-2/5}\right)$ is the location where the Görtler instability ensues (Wu et al., 2011).

3.4.2 Stage II. Asymptotic eigensolution regime: $\mathtt{G}^{-2/5} \ll \hat{x} \ll 1$

Following the incompressible case of Wu et al. (2011), we assume that the leading order asymptotic eigensolution for $\breve{x} \gg 1$ and $\eta=\mathscr{O}(1)$ for the middle layer ML is of the form

$$\breve{\mathbf{q}}=\breve{x}^{\varphi}\left[\left(\breve{x}^{-\alpha+1}U_E, V_E, W_E, \breve{x}^{-\alpha+3/2}P_E, \breve{x}^{-\alpha+1}T_E\right)+...\right]e^{\breve{\sigma}(\breve{x})}, \tag{3.49}$$

where the eigenvalue $\breve{\sigma}(\breve{x})$ is expanded at leading order as

$$\breve{\sigma}(\breve{x})=\breve{\sigma}_0\breve{x}^{\alpha}+..., \tag{3.50}$$

$\breve{\mathbf{q}}(\hat{x},\eta)=\{\breve{u},\bar{v},\bar{w},\breve{p},\breve{\tau}\}(\hat{x},\eta)$, $\mathbf{Q}_{\mathtt{E}}(\eta)=\{U_E,V_E,W_E,P_E,T_E\}(\eta)$, and $\breve{\sigma}$, α, φ are unknown constants. Substituting (3.49) and (3.50) into (3.47) yields

$$\breve{\sigma}_0\alpha F'\breve{x}^{\alpha}W_E-k_z^2\breve{x}^{-\alpha+5/2}TP_E=\mathscr{O}(1), \tag{3.51}$$

from which, equating the exponentials, $\alpha = 5/4$. A system of ODE for the eigenfunctions $\mathbf{Q}_{\mathrm{E}}(\eta)$ is then derived by substituting (3.49) and (3.50) into (3.44)-(3.48) and taking the limit $\check{x} \gg 1$, i.e., $\hat{x} \gg \mathtt{G}^{-2/5}$. The resulting inviscid equations are

$$\mathscr{C}\rceil \quad \alpha\check{\sigma}_0 U_E - \frac{T'}{T^2}V_E + \frac{1}{T}V_E' + W_E - \alpha\check{\sigma}_0\frac{F'}{T}T_E = 0, \tag{3.52}$$

$$\mathscr{X}| \quad \alpha\check{\sigma}_0 F' U_E + \frac{F''}{T}V_E = 0, \tag{3.53}$$

$$\mathscr{Y}| \quad 2\sqrt{2}F' U_E + P_E' - \frac{\sqrt{2}F'^2}{T}T_E = 0, \tag{3.54}$$

$$\mathscr{Z}| \quad \alpha\check{\sigma}_0 F' W_E - k_z^2 T P_E = 0, \tag{3.55}$$

$$\mathscr{E}\rfloor \quad \alpha\check{\sigma}_0 F' T_E + \frac{T'}{T}V_E = 0. \tag{3.56}$$

These equations can be rearranged to obtain an equation for V_E,

$$\frac{\mathrm{d}^2 V_E}{\mathrm{d}\eta^2} - \frac{2T'}{T}\frac{\mathrm{d}V_E}{\mathrm{d}\eta} + \left[\frac{2F''T'}{F'T} - \frac{F'''}{F'} + \frac{\sqrt{2}k_z^2}{(\check{\sigma}_0\alpha)^2}\left(\frac{2F''T}{F'} - T'\right)\right]V_E = 0, \tag{3.57}$$

subject to the boundary conditions

$$\eta = 0\rceil \quad V_E = 0, \tag{3.58}$$

$$\eta \to \infty\rfloor \quad \frac{\mathrm{d}V_E}{\mathrm{d}\eta} \to 0, \tag{3.59}$$

which correspond to the no-penetration and bounded conditions, respectively. Equation (3.57) is solved with the same numerical method used to solve the EV system (3.29)-(3.33). For $\mathtt{M} = 0$ the results agree with those of Wu et al. (2011). The first three eigenvalues $\check{\sigma}_0$

M	0	0.5	0.9	1.5	3	4
$\breve{\sigma}_0^{(1)}$	0.811	0.828	0.864	0.949	1.259	1.501
$\breve{\sigma}_0^{(2)}$	0.505	0.516	0.538	0.591	0.785	0.937
$\breve{\sigma}_0^{(3)}$	0.370	0.377	0.394	0.433	0.575	0.685
$\breve{\sigma}_1^{(1)}$	-1.567	-1.580	-1.608	-1.676	-1.927	-2.122
$\breve{\sigma}_1^{(2)}$	-1.656	-1.670	-1.700	-1.773	-2.042	-2.248
$\breve{\sigma}_1^{(3)}$	-1.709	-1.723	-1.754	-1.829	-2.105	-2.316
$\breve{\mathtt{B}}$	1.016	1.004	0.978	0.925	0.779	0.701

Table 3.1 The first three eigenvalues $\breve{\sigma}_0$ from (3.50) and $\breve{\sigma}_1$ from (3.75), and the wall-normal scaling coefficient $\breve{\mathtt{B}}$ used in (3.61) for different Mach numbers.

are shown in table 3.1 for different values of the Mach number M. There is a very mild influence of M in subsonic flow conditions while in supersonic flow conditions $\breve{\sigma}_0$ increases as M increases, so the Görtler vortices are more unstable as the compressibility effects intensify.

To study the flow in the vicinity of the wall, we take the mean-flow values at $\eta = 0$, i.e., $F = F' = F''' = T' = 0$, while F'', T, $T'' = \mathscr{O}(1)$. Locally, since $\eta = 0$ is a regular singular point, the solution V_E can be written as a Fröbenius series (Wu et al., 2011) which gives $V_E'(0) = 1$ when normalized. Additionally, the no-penetration condition requires $V_E(0) = 0$. Taking the derivative of (3.55) and substituting P_E' from (3.54) shows that the spanwise velocity component satisfies the no-slip condition, i.e., $W_E(0) = 0$. However, the streamwise velocity component does not satisfy the no-slip condition since, from (3.52) we find $U_E(0) \to -(\breve{\sigma}_0 \alpha T_0)^{-1}$, where $T_0 \equiv T(0)$. This is consistent with the inviscid nature of the governing equations (3.52)-(3.56) for $\hat{x} = \mathscr{O}\left(\mathtt{G}^{-2/5}\right)$ from which (3.57) is derived. In order for the streamwise velocity to satisfy the no-slip condition at the wall, a viscous sublayer VS is introduced in the near-wall region. Substituting (3.49) into (3.45) and balancing convection and diffusion in the limits $\eta \to 0$ and $\breve{x} \gg 1$ yields

$$\alpha \breve{\sigma}_0 F' U_E \sim \breve{x}^{-\alpha} \frac{\mu}{2T} U_E'', \tag{3.60}$$

from which

$$\eta \sim \breve{\mathtt{B}} \breve{x}^{-5/12}, \tag{3.61}$$

where $\breve{\mathrm{B}} \equiv [\mu_0/(2\lambda\alpha\breve{\sigma}_0 T_0)]^{1/3}$ and T_0, $\mu_0 \equiv \mu(0)$, $\lambda \equiv F''(0)$ arise from Taylor-expanding the mean flow at $\eta = 0$. The thickness of the VS is $\eta_{\text{VS}} = \mathscr{O}\left(\breve{x}^{-5/12}\right)$ where the constant of proportionality $\breve{\mathrm{B}}$ decreases as the Mach number increases, as shown in table 3.1. The wall-normal scaled variable for the VS becomes

$$\zeta_{\text{II}} = \breve{\mathrm{B}}^{-1}\breve{x}^{5/12}\eta. \tag{3.62}$$

An order of magnitude balance of the equations for $\eta \to 0$ reveals that $P_E = \mathscr{O}(\eta)$ from (3.55), $V_E = \mathscr{O}(\eta)$ from (3.52), and consequently $T_E = \mathscr{O}(\eta)$ from (3.56). Therefore, the solution in the VS expands as

$$\breve{\mathbf{q}} = \breve{x}^{\varphi}\left[\left(\breve{x}^{-1/4}u_s,\, \eta v_s,\, w_s,\, \breve{x}^{1/4}\eta p_s, \breve{x}^{-1/4}\eta\tau_s\right) + ...\right] e^{\breve{\sigma}(\breve{x})}, \tag{3.63}$$

where $\breve{\mathbf{q}}(\hat{x}, \zeta_{\text{II}}) = \{\breve{u}, \breve{v}, \breve{w}, \breve{p}, \breve{\tau}\}(\hat{x}, \zeta_{\text{II}})$. Starting from the system of equations (3.44)-(3.48) for $\eta = \mathscr{O}(1)$ and $\breve{x} = \mathscr{O}(1)$, introducing the change of variable (3.62) and the expansion (3.63), the system of equations for $\zeta_{\text{II}} = \mathscr{O}(1)$ and $\breve{x} \gg 1$ becomes

$$\mathscr{C}\rceil \quad \alpha\breve{\sigma}_0 u_s + \frac{1}{T}v_s' + w_s = 0, \tag{3.64}$$

$$\mathscr{X}| \quad \alpha\breve{\sigma}_0\left(\zeta_{\text{II}}u_s - u_s''\right) + \frac{1}{T}v_s = 0, \tag{3.65}$$

$$\mathscr{Y}| \quad p_s' = 0, \tag{3.66}$$

$$\mathscr{Z}| \quad \lambda\alpha\breve{\sigma}_0\left(\zeta_{\text{II}}w_s - w_s''\right) - k_z^2 T p_s = 0, \tag{3.67}$$

$$\mathscr{E}\rfloor \quad \tau_s'' = 0, \tag{3.68}$$

where the prime $'$ indicates the derivative with respect to ζ_{II}. The energy equation $\mathscr{E}$ in the VS does not contain the pressure and the velocity components. Equations (3.64)-(3.68) are rearranged to obtain an equation for $v_s(\zeta_{\text{II}})$,

$$\left(\frac{\mathrm{d}^2}{\mathrm{d}\zeta_{\text{II}}^2} - \zeta_{\text{II}}\right) v_s'' = 0, \tag{3.69}$$

subject to the boundary conditions

$$\zeta_{\text{II}} = 0\rceil \;\; v_s = 0, \quad v_s' = 0, \tag{3.70}$$

$$\zeta_{\text{II}} \to \infty\rfloor \;\; v_s' \to 1. \tag{3.71}$$

The first boundary condition, i.e., $v_s = 0$, represents the no-penetration condition, while the derivatives of the wall-normal velocity come from the continuity equation. Only three boundary conditions are needed since two constants of integration can be obtained from (3.71). The solution of (3.69) has the same form as in the incompressible case of Wu et al. (2011),

$$v_s = \mathtt{C}_s \int_0^{\zeta_{\text{II}}} \left(\zeta_{\text{II}} - \bar{\zeta}_{\text{II}}\right) \mathtt{Ai}\left(\bar{\zeta}_{\text{II}}\right) \mathrm{d}\bar{\zeta}_{\text{II}}, \tag{3.72}$$

where $\mathtt{C}_s = 1/\int_0^\infty \mathtt{Ai}\left(\zeta_{\text{II}}\right) \mathrm{d}\zeta_{\text{II}} = 3$ and Ai is the Airy function of the first kind. For $\zeta_{\text{II}} \to \infty$ the solution becomes $v_s \to \zeta_{\text{II}} + v_\infty$, where the transpiration velocity v_∞ is

$$v_\infty \equiv -\mathtt{C}_s \int_0^\infty \zeta_{\text{II}} \mathtt{Ai}\left(\zeta_{\text{II}}\right) \mathrm{d}\zeta_{\text{II}}. \tag{3.73}$$

For $\zeta_{\text{II}} \to \infty$ the VS solution must match the ML solution for $\eta = \mathscr{O}(1)$.

The transpiration velocity (3.73) thus induces a correction term of order $\mathscr{O}\left(\breve{x}^{-5/12}\right)$ in the ML. We can then further expand (3.49) and (3.50) to take this viscous correction into account. We obtain

$$\begin{aligned}\breve{\mathbf{q}} = &\breve{x}^{\varphi}\Big[\left(\breve{x}^{-1/4}U_E, V_E, W_E, \breve{x}^{-1/4}P_E, \breve{x}^{-1/4}T_E\right) + \\ &\breve{x}^{-5/12}\left(\breve{x}^{-1/4}U_E^{(1)}, V_E^{(1)}, W_E^{(1)}, \breve{x}^{-1/4}P_E^{(1)}, \breve{x}^{-1/4}T_E^{(1)}\right) + \ldots\Big] e^{\breve{\sigma}(\breve{x})},\end{aligned} \tag{3.74}$$

where the eigenvalue $\breve{\sigma}(\breve{x})$ expands as

$$\breve{\sigma}(\breve{x}) = \breve{\sigma}_0 \breve{x}^{5/4} + \breve{x}^{-5/12}\left(\breve{\sigma}_1 \breve{x}^{5/4}\right) + \dots . \tag{3.75}$$

Substituting (3.74) and (3.75) into (3.44)-(3.48) for $\hat{x} = \mathscr{O}\left(\mathtt{G}^{-2/5}\right)$ and $\eta = \mathscr{O}(1)$, and collecting the $\mathscr{O}\left(\breve{x}^{-5/12}\right)$ terms gives

$$\mathscr{C}\rceil \;\; \frac{5\breve{\sigma}_0}{4}U_E^{(1)} - \frac{T'}{T^2}V_E^{(1)} + \frac{1}{T}V_E'^{(1)} + W_E^{(1)} - \frac{5\breve{\sigma}_0}{4}\frac{F'}{T}T_E^{(1)} = \frac{2\breve{\sigma}_1}{3\breve{\sigma}_0 T}\left(\frac{F''}{F'} - \frac{T'}{T}\right)V_E, \tag{3.76}$$

$$\mathscr{X}\mid \;\; \frac{5\breve{\sigma}_0}{4}F'U_E^{(1)} + \frac{F''}{T}V_E^{(1)} = \frac{2\breve{\sigma}_1}{3\breve{\sigma}_0}\frac{F''}{T}V_E, \tag{3.77}$$

$$\mathscr{Y}\mid \;\; 2\sqrt{2}F'U_E^{(1)} + P_E'^{(1)} - \frac{\sqrt{2}F'^2}{T}T_E^{(1)} = 0, \tag{3.78}$$

$$\mathscr{Z}\mid \;\; \frac{5\breve{\sigma}_0}{4}F'W_E^{(1)} - k_z^2 T P_E^{(1)} - \frac{5\breve{\sigma}_1}{6}\frac{F'}{T}V_E' = -\frac{5\breve{\sigma}_1}{6}\frac{F''}{T}V_E, \tag{3.79}$$

$$\mathscr{E}\rfloor \;\; \frac{T'}{T}V_E^{(1)} + \frac{5\breve{\sigma}_0}{4}F'T_E^{(1)} = \frac{2\breve{\sigma}_1}{3\breve{\sigma}_0}\frac{T'}{T}V_E. \tag{3.80}$$

An equation for $V_E^{(1)}$ can be derived from (3.76)-(3.80)

$$\frac{\mathrm{d}^2 V_E^{(1)}}{\mathrm{d}\eta^2} - 2\frac{T'}{T}\frac{\mathrm{d}V_E^{(1)}}{\mathrm{d}\eta} + \left[2\frac{F''T'}{F'T} - \frac{F'''}{F'} + \frac{2\sqrt{2}k_z^2}{\left(\alpha\breve{\sigma}_0\right)^2}\frac{F''T}{F'} - \frac{\sqrt{2}k_z^2}{\left(\alpha\breve{\sigma}_0\right)^2}T'\right]V_E^{(1)} =$$
$$\frac{10\sqrt{2}k_z^2\breve{\sigma}_1}{3\left(\breve{\sigma}_0\alpha\right)^3}\left(\frac{F''T}{F'} - \frac{1}{2}T'\right)V_E, \tag{3.81}$$

subject to the boundary conditions

$$\eta = 0\rceil \;\; V_E^{(1)}(0) = \breve{\mathtt{B}}\, v_\infty, \tag{3.82}$$

$$\eta \to \infty \rfloor \quad \frac{\mathrm{d}V_E^{(1)}}{\mathrm{d}\eta} \to 0, \tag{3.83}$$

where (3.82) comes from the matching at $\mathscr{O}\left(\breve{x}^{-5/12}\right)$ of the wall-normal velocity in the ML for $\eta \to 0$ with the wall-normal velocity in the VS for $\zeta_{\text{II}} \to \infty$. Condition (3.83) comes from requiring that the solution be bounded. The eigenvalue $\breve{\sigma}_1$ can either be computed numerically from the solution of (3.81) with its boundary conditions (3.82) and (3.83) or from the solvability condition

$$\frac{10\sqrt{2}k_z^2\breve{\sigma}_1}{3\left(\alpha\breve{\sigma}_0\right)^3}\left(\int_0^\infty \frac{F''T}{F'}{V_E}^2\mathrm{d}\eta - \frac{1}{2}\int_0^\infty T'{V_E}^2\mathrm{d}\eta\right) = \frac{2\lambda\breve{\sigma}_0\alpha T}{\mu}v_\infty\left(1+2\int_0^\infty \frac{T'}{T}\frac{\mathrm{d}V_E}{\mathrm{d}\eta}\mathrm{d}\eta\right), \tag{3.84}$$

derived by multiplying (3.81) by V_E, integrating from zero to infinity, and matching the $\mathscr{O}\left(\hat{x}^{-5/12}\right)$ terms of (3.74) with (3.63), using (3.57) and (3.62). The numerical values of $\breve{\sigma}_1$ are shown in table 3.1. They are all negative, thus indicating decaying perturbations. Similar to the eigenvalues $\breve{\sigma}_0$, the effect of Mach number is very small for subsonic conditions, while in the supersonic regime $\breve{\sigma}_1$ grows in absolute value as compressible effects intensify as the Mach number increases.

The no-slip condition is now satisfied, but we still need to require that the ML solution respects the condition $V_E \to 0$ for $\eta \to \infty$. By requiring the solution to be bounded as the free stream is approached, condition (3.59) gives $V_E = \mathtt{C}_2$, where $\mathtt{C}_2$ is an undefined constant determined by numerical solution. Therefore an outer layer OL must be introduced to allow V_E to vanish as $\eta \to \infty$. Introducing the mean-flow simplification for $\eta \to \infty$, i.e., $F \to \eta - \beta$ and $T = 1$, into (3.52), (3.53), (3.55), and (3.56) we find $U_E = 0$, $T_E = 0$, $W_E = 0$, and $P_E = 0$, respectively. We then expand (3.43) as

$$\bar{u} = \breve{u}\mathtt{G}^{-2/5} + \mathscr{O}\left(\mathtt{G}^{-3/5}\right), \quad \bar{\tau} = \breve{\tau}\mathtt{G}^{-2/5} + \mathscr{O}\left(\mathtt{G}^{-3/5}\right), \quad \bar{p} = \breve{p}\mathtt{G}^{2/5} + \mathscr{O}\left(\mathtt{G}^{1/5}\right). \tag{3.85}$$

Substituting these expansions into the $\mathscr{Y}$ equation (3.11) and neglecting terms $\ll \mathtt{G}^{-2/5}$, the equation is balanced if $\eta_{\text{OL}} \sim \mathtt{G}^{1/5}/\left(2\breve{x}\right)^{1/2}$. It follows that the new $\mathscr{O}(1)$ wall-normal

coordinate for the OL is

$$y_0 = \mathtt{G}^{-1/5}\,(2\breve{x})^{1/2}\,\eta. \tag{3.86}$$

From (3.9) and (3.85), the scaling in the OL for $y_0 = \mathscr{O}(1)$ is

$$\bar{\mathbf{q}} = \left\{\mathtt{G}^{-3/5}\bar{u}_0,\, \bar{v}_0,\, \mathtt{G}^{-1/5}\bar{w}_0,\, \mathtt{G}^{1/5}\bar{p}_0,\, \mathtt{G}^{-3/5}\bar{\tau}_0\right\}, \tag{3.87}$$

where $\bar{\mathbf{q}}(\breve{x}, y_0) = \{\bar{u}, \bar{v}, \bar{w}, \bar{p}, \bar{\tau}\}(\breve{x}, y_0)$. Substituting (3.87) into the LUBR equations (3.9)-(3.13) and taking the limit $\eta \to \infty$ gives the OL system

$$\mathscr{C}\rceil \;\; (2\breve{x})^{1/2}\frac{\partial \bar{v}_0}{\partial y_0} + \bar{w}_0 = 0, \tag{3.88}$$

$$\mathscr{X}| \;\; \frac{\partial \bar{u}_0}{\partial y_0} = 0, \tag{3.89}$$

$$\mathscr{Y}| \;\; \frac{\bar{v}_0}{2\breve{x}} + \frac{\partial \bar{v}_0}{\partial \breve{x}} + \frac{1}{(2\breve{x})^{1/2}}\frac{\partial \bar{p}_0}{\partial y_0} = 0, \tag{3.90}$$

$$\mathscr{Z}| \;\; \frac{\partial \bar{w}_0}{\partial y_0} - k_z^2\bar{p}_0 = 0, \tag{3.91}$$

$$\mathscr{E}\rfloor \;\; \frac{\partial \bar{\tau}_0}{\partial y_0} = 0, \tag{3.92}$$

where, in order to satisfy the boundary condition $V_E \to 0$ as $\eta \to \infty$, $\bar{u}_0$ and $\bar{\tau}_0$ must be set to zero. The solution to (3.88)-(3.92) is

$$\{\bar{p}_0, \bar{w}_0, \bar{v}_0\} = \left\{g_0', k_z^2 g_0, |k_z| g_0/(2\breve{x})\right\} e^{-|k_z| y_0}, \tag{3.93}$$

where

$$g_0(\breve{x}) = \breve{x}^{\gamma+1/2}\left[V_{E,\infty} + \mathscr{O}\left(\breve{x}^{-5/12}\right)\right] e^{\breve{\sigma}(\breve{x})} \tag{3.94}$$

and $V_{E,\infty} = V_E(\eta \to \infty)$ is determined by solving (3.57) numerically.

3.4.3 Stage III. Fully developed regime: $\hat{x} = \mathscr{O}(1)$

As the instability develops further downstream the local boundary-layer thickness δ^* becomes of the same order as the spanwise wavelength λ_z^*, i.e., $\delta^* = \mathscr{O}(\lambda_z^*)$, and the spanwise viscous diffusion and the spanwise pressure gradient are at work. At this location the Görtler vortices are fully developed (Wu et al., 2011) with $\breve{x} = \mathscr{O}\left(\mathtt{G}^{2/5}\right)$, i.e., $\hat{x} = \mathscr{O}(1)$, $\eta_{\mathtt{OL}} = \mathscr{O}(1)$ and the OL merging with the ML. Stage III is therefore only composed of the ML and the VS. Equations (3.74), (3.75), and (3.85) suggest that the solution in the fully developed regime can be expanded in the WKBJ form (Wu et al., 2011)

$$\begin{aligned}\bar{\mathbf{q}} = &\Big\{ \left[\mathtt{G}^{-1/2}u_0, v_0, w_0, \mathtt{G}^{1/2}p_0, \mathtt{G}^{-1/2}\tau_0\right] + \\ &\mathtt{G}^{-1/6}\left[\mathtt{G}^{-1/2}u_1, v_1, w_1, \mathtt{G}^{1/2}p_1, \mathtt{G}^{-1/2}\tau_1\right] + \ldots \Big\} e^{\mathtt{G}^{1/2}\int^{\hat{x}}\hat{\sigma}(x)\mathrm{d}x},\end{aligned} \tag{3.95}$$

where

$$\hat{\sigma}(\hat{x}) = \hat{\sigma}_0 + \mathtt{G}^{-1/6}\hat{\sigma}_1 + \ldots, \tag{3.96}$$

and the second term of order $\mathscr{O}(\mathtt{G}^{-1/6})$ takes into account the effect of the VS. Substituting (3.95) into the LUBR equations (3.9)-(3.13) gives the system at leading order for $\hat{x} = \mathscr{O}(1)$ and $\eta = \mathscr{O}(1)$,

$$\mathscr{C}\rceil \quad \hat{\sigma}_0 u_0 - \frac{T'}{T^2}v_0 + \frac{1}{T}\frac{\partial v_0}{\partial \eta} + w_0 - \hat{\sigma}_0\frac{F'}{T}\tau_0 = 0, \tag{3.97}$$

$$\mathscr{X}\mid \quad \hat{\sigma}_0 F' u_0 + \frac{F''}{T}v_0 = 0, \tag{3.98}$$

$$\mathscr{Y}\mid \quad \frac{2F'}{(2\hat{x})^{1/2}}u_0 + \hat{\sigma}_0 F' v_0 - \frac{F'^2}{(2\hat{x})^{1/2}T}\tau_0 + \frac{1}{2\hat{x}}\frac{\partial p_0}{\partial \eta} = 0, \tag{3.99}$$

$$\mathscr{L}\rfloor \;\; \hat{\sigma}_0 F' w_0 - k_z^2 T p_0 = 0, \tag{3.100}$$

$$\mathscr{E}\rfloor \;\; \hat{\sigma}_0 F' \tau_0 + \frac{T'}{T} v_0 = 0. \tag{3.101}$$

We can rearrange (3.97)-(3.101) to find

$$\frac{\partial^2 v_0}{\partial \eta^2} - \frac{2T'}{T}\frac{\partial v_0}{\partial \eta} + \left[\frac{2F''T'}{F'T} - \frac{F'''}{F'} - 2\hat{x}k_z^2 T^2 + (2\hat{x})^{1/2}\frac{k_z^2}{\hat{\sigma}_0^2}\left(\frac{2F''T}{F'} - T'\right)\right] v_0 = 0, \tag{3.102}$$

subject to the boundary conditions

$$\eta = 0\rceil \;\; v_0 = 0, \tag{3.103}$$

$$\eta \to \infty\rfloor \;\; v_0 \to 0. \tag{3.104}$$

Note that v_0 vanishes as $\eta \to \infty$ since no outer layer is needed to bring the wall-normal velocity to zero like in stage II. Equation (3.102), also derived by Dando and Seddougui (1993), is solved with the same method used to solve (3.57) and the EV system (3.29)-(3.33). In the limit $\hat{x} \to 0$ the solution in the fully developed regime of stage III must be consistent with the solution of the asymptotic stage II. The dominant balance in (3.102) shows that, in order for all the terms except the third term in the brackets to remain $\mathscr{O}(1)$, $\hat{\sigma}_0 = \mathscr{O}\left(\hat{x}^{1/4}\right)$ and, from the exponential in (3.95),

$$\int^{\hat{x}} \hat{\sigma}_0(x)\mathrm{d}x \sim \frac{4}{5}\hat{x}^{5/4}, \tag{3.105}$$

which is consistent, at leading order, with the exponential in (3.74).

Changing the Mach number affects the boundary-layer thickness δ_{99}^*, i.e., the wall-normal location where $U^* = 0.99U_\infty^*$, and η through the mean temperature T. We therefore use the dimensionless wall-normal coordinate $y_{99} \equiv y^*/\delta_{99}^*$ when comparing results at different Mach numbers. Figure 3.4 (left) shows the growth rate of the perturbation along the streamwise direction for the first eigenvalue $\hat{\sigma}_0^{(1)}$. As `M` increases, the stabilizing effect of `M` begins

closer to the leading edge. Up to $\mathtt{M} = 2$, the growth rate at $\hat{x} \approx 15$ converges to a weakly varying function of the Mach number. The wall-normal location of the vortices, shown in the inset of figure 3.4 (left), decreases as the Mach number increases. However, for $\mathtt{M} > 3$ and high enough $\hat{x}$ the vortices location tends to a nearly constant value. Figure 3.4 (right) demonstrates that for $\hat{x} \ll 1$ the growth rate (3.96) from stage III matches asymptotically the growth rate (3.50) from stage II.

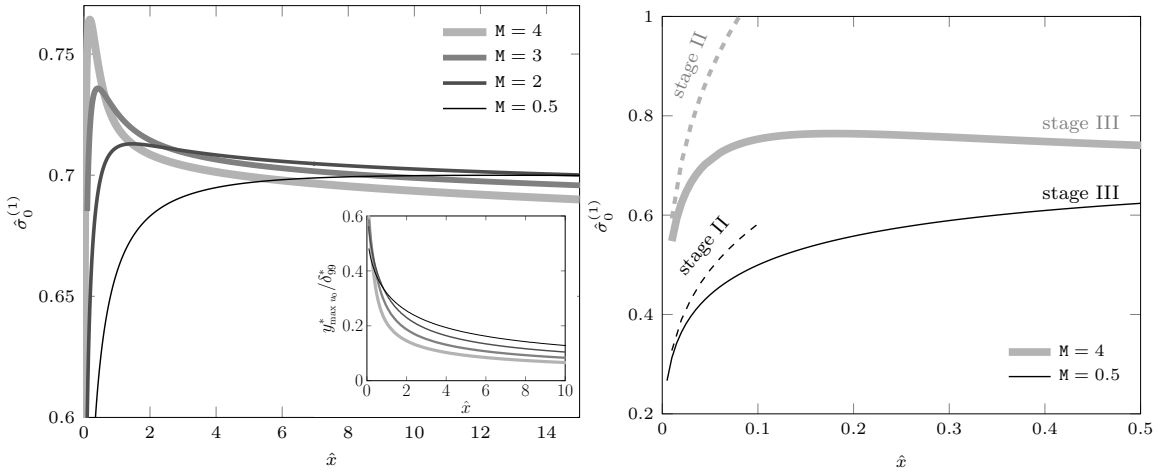

Fig. 3.4 The effect of the Mach number on $\hat{\sigma}_0^{(1)}$ (left) and detail of the graph on the left in the region $\hat{x} \ll 1$ for comparison with stage II (right). Inset: the wall-normal location of $\mathtt{G_V}$-vortices (right) for stage III.

In stage III, as for the asymptotic eigensolution regime of stage II, a VS has to be introduced in order to guarantee the no-slip condition at the wall will be satisfied because it is found that $u_0 \to -(\hat{\sigma}_0 T_0)^{-1}$ as $\eta \to 0$. Substituting (3.95) into the $\mathscr{X}$ equation (3.10) and balancing the convection and the diffusion terms in the limit $\eta \to 0$, the new $\mathscr{O}(1)$ wall-normal scaling variable, proportional to the VS thickness, becomes

$$\zeta_{\text{III}} = \mathtt{G}^{1/6} \hat{\mathtt{B}}^{-1} \hat{x}^{1/3} \eta, \tag{3.106}$$

where $\hat{\mathtt{B}}(\hat{x}) \equiv [\mu_0 / (2\lambda \hat{\sigma}_0 T_0)]^{1/3}$. A comparison with (3.62) shows that, by fixing G and $\hat{\mathtt{B}}$, if $\hat{x}$ increases the VS becomes thinner more rapidly in stage II $\left(\mathscr{O}\left(\hat{x}^{-5/12}\right)\right)$ than in stage III $\left(\mathscr{O}\left(\hat{x}^{-1/3}\right)\right)$ since ζ_{II} and ζ_{III} are of order one. The value of $\hat{\mathtt{B}}(\hat{x})$ approaches a constant for $\hat{x} > 5$. From (3.106) it can be noticed that, in order to maintain $\zeta_{\text{III}} = \mathscr{O}(1)$, η must increase

when G increases, i.e., the VS thickness is larger for flows over strong curvature. Substituting (3.95) into the LUBR equations (3.9)-(3.13), and balancing the convection and diffusion terms gives the expansion of the flow in the VS,

$$\bar{\mathbf{q}} = \left\{ \mathtt{G}^{-1/2} u_b, \mathtt{G}^{-1/6} \hat{\mathtt{B}} \hat{x}^{-1/3} v_b, w_b, \mathtt{G}^{-2/3} \hat{\mathtt{B}} \hat{x}^{-1/3} p_b, \mathtt{G}^{-1/2} \tau_b \right\} e^{\mathtt{G}^{1/2} \int^{\hat{x}} \hat{\sigma}(x) \mathrm{d}x}, \tag{3.107}$$

where $\bar{\mathbf{q}}(\hat{x}, \zeta_{\text{III}}) = \{\bar{u}, \bar{v}, \bar{w}, \bar{p}, \bar{\tau}\}(\hat{x}, \zeta_{\text{III}})$. By substituting (3.107) into the LUBR equations (3.9)-(3.13), we recover the system of equations for $\hat{x} = \mathscr{O}(1)$ and $\eta \to 0$,

$$\mathscr{C}\rceil \;\; \hat{\sigma}_0 u_b + \frac{1}{T} v_b' + w_b = 0, \tag{3.108}$$

$$\mathscr{X}| \;\; \hat{\sigma}_0 \left(\zeta_{\text{III}} u_b - u_b'' \right) + \frac{1}{T} v_b = 0, \tag{3.109}$$

$$\mathscr{Y}| \;\; p_b' = 0, \tag{3.110}$$

$$\mathscr{Z}| \;\; \lambda \hat{\sigma}_0 \left(\zeta_{\text{III}} w_b - w_b'' \right) - k_z^2 T p_b = 0, \tag{3.111}$$

$$\mathscr{E}\rfloor \;\; \tau_b' = 0, \tag{3.112}$$

where the prime $'$ indicates the derivative with respect to ζ_{III}. The equations are similar to the asymptotic eigensolution regime (3.64)-(3.68) and therefore v_b satisfies the Airy equation (3.69) along with the boundary conditions (3.70) and (3.71). A composite solution for the streamwise velocity u_c can be constructed from the solution in the ML and VS, i.e., u_0 and u_b, respectively, as

$$u_c = u_0 + u_b - u_{com}, \tag{3.113}$$

where

$$u_{com} = \lim_{\eta\to 0} u_0 = \lim_{\zeta_{\text{III}}\to\infty} u_b = -\frac{1}{\hat{\sigma}_0 T_0} \tag{3.114}$$

is the common solution.

The streamwise velocity u_b is computed by integrating (3.109) through the method of variation of parameters with the known velocity v_b as the forcing term. The solution is:

$$u_b(\zeta_{\text{III}}) = \mathtt{C}_1\mathtt{Ai} + \mathtt{C}_2\mathtt{Bi} - \mathtt{Ai}\int_0^{\zeta_{\text{III}}} \frac{\mathtt{f}\,\mathtt{Bi}}{\mathtt{W}}\mathrm{d}\bar{\zeta}_{\text{III}} + \mathtt{Bi}\int_0^{\zeta_{\text{III}}} \frac{\mathtt{f}\,\mathtt{Ai}}{\mathtt{W}}\mathrm{d}\bar{\zeta}_{\text{III}}, \tag{3.115}$$

where $\mathtt{Ai} = \mathtt{Ai}(\zeta_{\text{III}})$ and $\mathtt{Bi} = \mathtt{Bi}(\zeta_{\text{III}})$ are the two linearly independent solutions of the Airy equation, $\mathtt{f}(\zeta_{\text{III}}) = v_b(\zeta_{\text{III}})/(\hat{\sigma}_0 T_0)$ and $\mathtt{W}(\zeta_{\text{III}}) = \mathtt{Ai}\,\mathtt{Bi}' - \mathtt{Bi}\,\mathtt{Ai}'$ is the Wronskian. The constant $\mathtt{C}_2 = -0.2061$ is found first by numerically imposing the outer boundary condition (3.114) as the term proportional to $\mathtt{C}_1$ vanishes as $\zeta_{\text{III}} \to \infty$. Once $\mathtt{C}_2$ is known, the constant $\mathtt{C}_1 = 0.3571$ is found by imposing the first of (3.59).

The resulting solutions $\bar{u}_b$, $\bar{u}_0$, and $\bar{u}_c$ for $\mathtt{M} = 0.5$ and $\mathtt{M} = 3$ are displayed in figure 3.5. These results confirm that as the Mach number increases, but still remaining an order-one quantity, the vortices tend to move towards the wall when $\mathtt{G} \gg 1$. The requirement of a very high $\mathtt{G}$ value in figure 3.5 arises from the inner coordinate being proportional to $\mathtt{G}^{1/6}$ in (3.106) and is necessary to guarantee that the VS is thinner than the ML. The composite solution follows the inner VS solution near the wall and the outer ML solution away from the wall.

The viscous correction for $\hat{x} = \mathscr{O}(1)$ and $\eta = \mathscr{O}(1)$ is found by substituting the expansion (3.95) into the LUBR equations (3.9)-(3.13) and collecting the $\mathscr{O}\left(\mathtt{G}^{-1/6}\right)$ terms for $u_1, v_1, w_1, p_1, \tau_1$ in (3.95),

$$\mathscr{C}\rceil \quad \hat{\sigma}_0 u_1 - \frac{T'}{T^2}v_1 + \frac{1}{T}\frac{\partial v_1}{\partial \eta} + w_1 - \hat{\sigma}_0\frac{F'}{T}\tau_1 - \hat{\sigma}_1\frac{F'}{T}\tau_0 + \hat{\sigma}_1 u_0 = 0, \tag{3.116}$$

$$\mathscr{X}\rfloor \quad \hat{\sigma}_0 F' u_1 + \frac{F''}{T}v_1 + \hat{\sigma}_1 F' u_0 = 0, \tag{3.117}$$

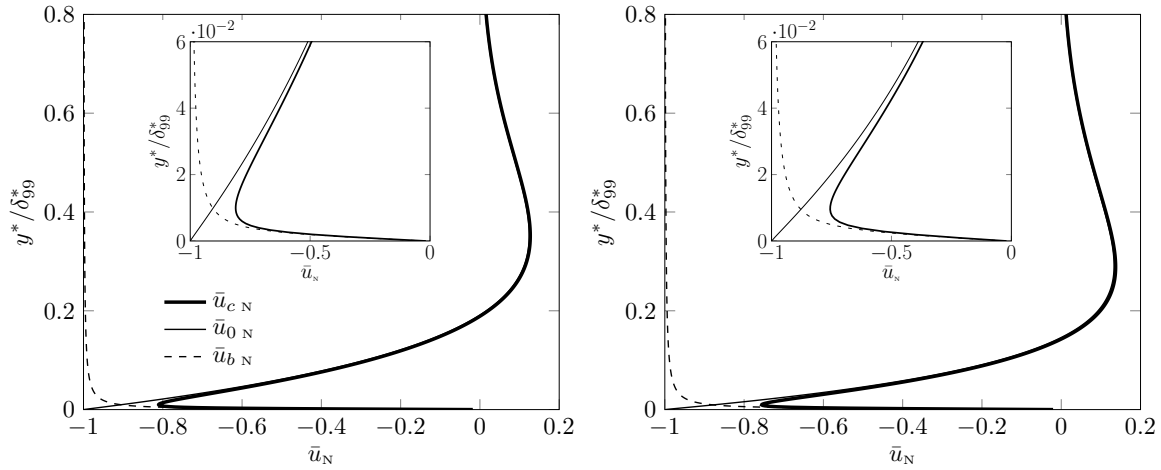

Fig. 3.5 Normalized profiles of the streamwise velocity perturbation for $\mathtt{M} = 0.5$ (left) and $\mathtt{M} = 3$ (right) from the eigensolution of stage III at $\mathtt{G} = 10^{15}$ and $\hat{x} = 1$. Insets: details of the solutions near the wall.

$$\mathscr{Y}\big| \quad \frac{2F'}{(2\hat{x})^{1/2}}u_1 + \hat{\sigma}_0 F' v_1 + \frac{1}{2\hat{x}}\frac{\partial p_1}{\partial \eta} - \frac{F'^2}{(2\hat{x})^{1/2}T}\tau_1 + \hat{\sigma}_1 F' v_0 = 0, \tag{3.118}$$

$$\mathscr{Z}\big| \quad \hat{\sigma}_0 F' w_1 - k_z^2 T p_1 + \hat{\sigma}_1 F' w_0 = 0, \tag{3.119}$$

$$\mathscr{E}\big\rfloor \quad \frac{T'}{T}v_1 + \hat{\sigma}_0 F' \tau_1 + \hat{\sigma}_1 F' \tau_0 = 0, \tag{3.120}$$

from which the equation for v_1 is derived

$$\frac{\partial^2 v_1}{\partial \eta^2} - 2\frac{T'}{T}\frac{\partial v_1}{\partial \eta} + \left[2\frac{F''T'}{F'T} - \frac{F'''}{F'} - 2\hat{x}k_z^2T^2 + \frac{2(2\hat{x})^{1/2}k_z^2}{\hat{\sigma}_0^2}\frac{F''T}{F'} - \frac{(2\hat{x})^{1/2}k_z^2}{\hat{\sigma}_0^2}T'\right]v_1 =$$
$$\frac{2(2\hat{x})^{1/2}k_z^2\hat{\sigma}_1}{\hat{\sigma}_0^3}\left(2\frac{F''T}{F'} - T'\right)v_0, \tag{3.121}$$

along with its boundary conditions

$$\eta = 0\big\rceil \quad v_1 = \hat{\mathrm{B}}\hat{x}^{-1/3}v_\infty, \tag{3.122}$$

$$\eta \to \infty \rfloor \quad \frac{\partial v_1}{\partial \eta} \to 0. \tag{3.123}$$

As for the asymptotic eigensolution regime, the boundary condition for $\eta \to 0$ stems from the matching with the ML solution. Applying the solvability condition to (3.121) gives

$$\left(1+2\int_0^\infty \frac{T'}{T}\frac{\partial v_0}{\partial \eta}\mathrm{d}\eta\right)\left(\frac{2\lambda\hat{\sigma}_0 T}{\mu}\right)^{-1/3}\hat{x}^{-1/3}v_\infty =$$
$$-\frac{2\,(2\hat{x})^{1/2}k_z^2\hat{\sigma}_1}{\hat{\sigma}_0^3}\left(\int_0^\infty T'v_0^2\mathrm{d}\eta - 2\int_0^\infty \frac{F''T}{F'}v_0^2\mathrm{d}\eta - 2\int_0^\infty \frac{F''T}{F'}v_0^2\mathrm{d}\eta\right). \tag{3.124}$$

The eigenvalue $\hat{\sigma}_1$ can either be calculated from the solvability condition or from the numerical integration of (3.121).

3.4.4 Stage IV. Wall layer regime: $\hat{x} \gg 1$

It has been shown by Hall (1983) and Wu et al. (2011) for the incompressible case that, contrary to the Klebanoff modes generated over flat plates, Görtler vortices move towards the surface as they develop downstream in the limit $\hat{x} \gg 1$ ($\delta^* \gg \lambda_z^*$). It will be shown in §4 that this is true only up to $\mathtt{M} \simeq 3$. For $\mathtt{M} \geq 3$, the perturbation initially tends to concentrate near the wall, but then, as $\hat{x}$ increases, it moves to the core of the boundary layer. Following the work of Wu et al. (2011), the eigenvalue problem for the inviscid regime (3.102) can be simplified in the limit $\hat{x} \gg 1$ and $\eta \to 0$. From the simplifications of the mean flow near the wall and introducing a new WL variable $\hat{\zeta}_{\text{III}} = (2\hat{x})^{1/2}\eta T_0$ to cancel the dependence on $\hat{x}$, (3.102) simplifies to

$$\frac{\partial^2 v_0}{\partial \hat{\zeta}_{\text{III}}^2} - \left(1 - \frac{2}{\hat{\zeta}_{\text{III}}\hat{\sigma}_0^2}\right)k_z^2 v_0 = 0. \tag{3.125}$$

This equation is the same as for the incompressible case and has a set of eigenvalues $\hat{\sigma}_0 = (k_z/n)^{1/2}$, with $n = 1,2,3,...$ (Denier et al., 1991). Applying the same procedure to (3.121), we find that $\hat{\sigma}_1 = \mathscr{O}\left(\hat{x}^{1/6}\right)$ for $\hat{x} \gg 1$ and $\eta \to 0$, which implies that, referring to (3.96), the viscous correction terms for the growth rate at $\eta = \mathscr{O}(1)$ become of leading order as the flow evolves to $\hat{x} = \mathscr{O}(\mathtt{G})$.

For $\hat{x} \gg 1$, we investigate the flow at $\hat{x} = \mathscr{O}(\mathtt{G})$, where the viscous correction term becomes of leading order. The streamwise and wall-normal variables rescale as

$$\tilde{x} = \frac{\hat{x}}{\mathtt{G}}, \qquad \zeta_{\text{IV}} = (2\tilde{x})^{1/2}\,\eta\,\mathtt{G}^{1/2} T_0, \tag{3.126}$$

respectively. From an order of magnitude analysis of the LUBR equations (3.9)-(3.13) the flow expands as

$$\bar{\mathbf{q}} = \left\{\tilde{u}_0, \tilde{v}_0, \mathtt{G}^{1/2}\tilde{w}_0, \mathtt{G}^{1/2}\tilde{p}_0, \mathtt{G}^{1/2}\tilde{\tau}_0\right\} e^{\mathtt{G}^{3/2}\int^{\tilde{x}} \hat{\sigma}(x)\mathrm{d}x}, \tag{3.127}$$

where $\bar{\mathbf{q}}(\tilde{x}, \zeta_{\text{IV}}) = \{\bar{u}, \bar{v}, \bar{w}, \bar{p}, \bar{\tau}\}(\tilde{x}, \zeta_{\text{IV}})$. Substituting (3.127) into the LUBR equations (3.9)-(3.13) and using the near-wall approximations for the mean flow, the system of equations for $\hat{x} = \mathscr{O}(\mathtt{G})$ becomes

$$\mathscr{C}] \quad \hat{\sigma}\tilde{u}_0 + (2\tilde{x})^{1/2}\frac{\partial \tilde{v}_0}{\partial \zeta_{\text{IV}}} + \tilde{w}_0 + \left[\frac{ik_x\mathtt{R}}{T} - \frac{\lambda\,\zeta_{\text{IV}}\hat{\sigma}}{(2\tilde{x})^{1/2}T^2}\right]\tilde{\tau}_0 = 0, \tag{3.128}$$

$$\mathscr{X}| \quad \left[-ik_x\mathtt{R} + \frac{\zeta_{\text{IV}}\hat{\sigma}}{(2\tilde{x})^{1/2}}\frac{\lambda}{T} + k_z^2\mu T\right]\tilde{u}_0 - \mu T\frac{\partial^2\tilde{u}_0}{\partial\zeta_{\text{IV}}^2} + \frac{\lambda}{T}\tilde{v}_0 - \frac{\lambda\mu'}{(2\tilde{x})^{1/2}}\frac{\partial\tilde{\tau}_0}{\partial\zeta_{\text{IV}}} = 0, \tag{3.129}$$

$$\begin{aligned}\mathscr{Y}| \quad & \frac{\zeta_{\text{IV}}}{\tilde{x}}\frac{\lambda}{T}\tilde{u}_0 + \left[\frac{\zeta_{\text{IV}}\hat{\sigma}}{(2\tilde{x})^{1/2}}\frac{\lambda}{T} - ik_x\mathtt{R} + k_z^2\mu T\right]\tilde{v}_0 - \mu T\frac{\partial^2\tilde{v}_0}{\partial\zeta_{\text{IV}}^2} + \frac{T}{(2\tilde{x})^{1/2}}\frac{\partial\tilde{p}_0}{\partial\zeta_{\text{IV}}} - \\ & \left[\frac{(\zeta_{\text{IV}}\lambda)^2}{(2\tilde{x})^{3/2}T} + \frac{\hat{\sigma}\mu'\lambda}{2\tilde{x}} + \frac{\zeta_{\text{IV}}\hat{\sigma}\mu'\lambda}{(2\tilde{x})^2} + \frac{\hat{\sigma}\mu\lambda}{6\tilde{x}T}\right]\tilde{\tau}_0 + \left[\frac{ik_x\mathtt{R}\mu}{3\,(2\tilde{x})^{1/2}} + \frac{\zeta_{\text{IV}}\hat{\sigma}\mu\lambda}{6\tilde{x}T}\right]\frac{\partial\tilde{\tau}_0}{\partial\zeta_{\text{IV}}} = 0,\end{aligned} \tag{3.130}$$

$$\mathscr{Z}| \quad \left[\frac{\zeta_{\text{IV}}\hat{\sigma}\lambda}{(2\tilde{x})^{1/2}T} - ik_x\mathtt{R} + k_z^2\mu T\right]\tilde{w}_0 - \mu T\frac{\partial^2\tilde{w}_0}{\partial\zeta_{\text{IV}}^2} - k_z^2 T\tilde{p}_0 = 0, \tag{3.131}$$

$$\mathscr{E}\rfloor \quad \left[\frac{k_z^2}{\mathtt{Pr}}\mu T - ik_x\mathtt{R} + \frac{\zeta_{\text{IV}}\hat{\sigma}\lambda}{(2\tilde{x})^{1/2}T}\right]\tilde{\tau}_0 - \frac{\mu T^2}{\mathtt{Pr}}\frac{\partial^2\tilde{\tau}_0}{\partial\zeta_{\text{IV}}^2} = 0. \tag{3.132}$$

These equations could be rearranged to eliminate $\tilde{w}_0$ and $\tilde{v}_0$. The boundary conditions are $\tilde{u}_0 = \tilde{v}_0 = \tilde{\tau}_0 = 0$ for $\zeta_{\text{IV}} = 0$ and $\tilde{u}_0$, $\tilde{v}_0$, $\tilde{\tau}_0 \to 0$ for $\zeta_{\text{IV}} \to \infty$. Finally, for $\tilde{x} = \mathscr{O}(1)$ and from the boundary-layer thickness $\delta^* = \mathscr{O}\left((\nu_\infty x^*/U_\infty^*)^{1/2}\right)$, we find that $\delta^*/\lambda_z^* = \mathscr{O}\left(\mathtt{G}^{1/2}\right)$, identified by Denier et al. (1991) as the most unstable regime for incompressible Görtler flow.

3.4.5 Physical summary

From the asymptotic analysis in the limit of large Görtler number, we can infer the following physical properties:

- as in the incompressible case, the unbalance between pressure and centrifugal forces triggers the Görtler instability at a streamwise location $\hat{x} = \mathscr{O}\left(\mathtt{G}^{-2/5}\right)$, i.e., when both the wall-normal and the spanwise pressure gradients are active in the wall-normal and spanwise momentum equations, respectively;
- in stage II, i.e., where the boundary-layer equations describe the flow as the spanwise viscous diffusion effects are negligible, increasing the Mach number causes:
  - the boundary-layer perturbation to intensify (table 3.1);
  - the perturbation to shift away from the wall;
- in stage III, i.e., further downstream where the flow is described by the boundary-region equations because the spanwise viscous diffusion and the spanwise pressure gradient are at work:
  - the growth rate decreases slightly downstream (figure 3.4);
  - increasing the Mach number has a stabilizing effect on the growth rate, which is more intense in supersonic flow conditions (figure 3.4);

- for $\mathtt{M} = \mathscr{O}(1)$, the vortices move towards the wall as the Mach number increases (figure 3.4 and figure 3.5);
- we have obtained a composite asymptotic solution, whose near-wall part is fully viscous and adiabatic, while the part in the boundary-layer core is inviscid.

3.5 Triple-deck equations

The previous paragraph focused on the cases for which $\kappa > 0.15$. As a consequence, also mentioned in §3.1, the highly-oblique TS waves investigated by Ricco and Wu (2007) did not occur. In this section only we evaluate the influence of curvature when $\kappa \ll 1$.

Due to the need to extend the investigation to steady flows we have scaled the streamwise coordinate as $\hat{x}$. However, since TS-waves are unsteady, we can scale our equations using $\bar{x}$ instead which allows for a straightforward comparison with Ricco and Wu (2007). The following transformation

$$\begin{aligned}
\bar{u}(\bar{x},\eta) &= \bar{u}(\hat{x},\eta)\, k_x\mathtt{R} \\
\bar{v}(\bar{x},\eta) &= \bar{v}(\hat{x},\eta) \\
\bar{w}(\bar{x},\eta) &= \bar{w}(\hat{x},\eta) \\
\bar{p}(\bar{x},\eta) &= \bar{p}(\hat{x},\eta) \\
\bar{\tau}(\bar{x},\eta) &= \bar{\tau}(\hat{x},\eta)\, k_x\mathtt{R} \\
\bar{x} &= \hat{x}\, k_x\mathtt{R}
\end{aligned} \tag{3.133}$$

applied to (3.9)-(3.13) allows to recover the LUBR equations of Ricco and Wu (2007), hereafter referred to as $\bar{x}$-LUBR equations, derived in a $(\bar{x},\eta)$ coordinate system with the curvature effect

$$\frac{\mathtt{G}}{(2\bar{x})^{1/2}}\left[2F'\bar{u}(\bar{x},\eta) - \frac{F'^2}{T}\bar{\tau}(\bar{x},\eta)\right]\frac{\kappa}{k_z} \tag{3.134}$$

added to the $\mathscr{Y}$ equation. Ricco and Wu (2007) demonstrated that the highly oblique TS-waves originate from a decaying Lam-Rott solution (Lam and Rott (1993); Saric et al. (2002)). In the double limits $\kappa \ll 1$ and $\bar{x} \gg 1$ the curvature term (3.134) becomes negligible, hence the Lam-Rott solution is not influenced by curvature effects, and the solution of Ricco and Wu (2007) is recovered. We now also demonstrate analytically that the dispersion relation derived from the triple-deck interactive regime is not influenced by curvature effects.

Starting from the main deck for which $\eta = \mathscr{O}(1)$, the variable $x_1 = \kappa\bar{x} = \mathscr{O}(1)$ is introduced and the solution expands as

$$\bar{\mathbf{q}}(\bar{x},\eta) = \left(u_1,\, \kappa^{-1/2}v_1,\, w_1,\, \kappa^{-5/2}p_1,\, \tau_1\right)E + ..., \tag{3.135}$$

where $E(\bar{x}) = e^{i\kappa^{-1/2}\int_0^{\bar{x}}\alpha_1(x_1)\mathrm{d}\check{x}}$, $\bar{\mathbf{q}} = \{\bar{u},\bar{v},\bar{w},\bar{p},\bar{\tau}\}$, $\mathbf{q_1}(x_1,\eta) = \{u_1,v_1,w_1,p_1,\tau_1\}(x_1,\eta)$, and $\alpha_1(\bar{x})$ is a complex wavenumber that can be found through a dispersion relation as follows.

Substituting (3.135) into the $\bar{x}$-LUBR equations, the additional curvature effect is negligible in the limit $\kappa \ll 1$, therefore the solution remains the same as in Ricco and Wu (2007)

$$\{u_1,v_1,w_1,\tau_1\} = \left\{\left(A(x_1)F''/T,\, -i\alpha_1 A(x_1)F',\, p_1(x_1)T/(i\alpha_1 F'),\, -A(x_1)T'/T\right)\right\}. \tag{3.136}$$

Moving to the lower deck, the wall-normal variable is rescaled as

$$\bar{\eta} = \kappa^{-1/2}\eta = \mathscr{O}(1) \tag{3.137}$$

and the solution expands as

$$\bar{\mathbf{q}}(x_1,\bar{\eta}) = \left(\bar{u}_1,\, \bar{v}_1,\, \kappa^{-1/2}\bar{w}_1,\, \kappa^{-5/2}\bar{p}_1,\, \kappa^{1/2}\bar{\tau}_1\right)E + \ldots. \tag{3.138}$$

Substituting (3.138) into the $\bar{x}$-LUBR equations and using the near wall approximations we find the system of equations

$$\mathscr{C}\rceil \;\; i\alpha_1\bar{u}_1 + \frac{1}{T_0}\frac{\partial \bar{v}_1}{\partial \bar{\eta}} + \bar{w}_1 = 0, \tag{3.139}$$

$$\mathscr{X}\rceil \;\; i(-1+\lambda\alpha_1\bar{\eta})\,\bar{u}_1 + \frac{\lambda}{T_0}\bar{v}_1 = \frac{\mu_0}{2\bar{x}_1 T_0}\frac{\partial^2 \bar{u}_1}{\partial \bar{\eta}^2}, \tag{3.140}$$

$$\mathscr{Y}\rceil \;\; \frac{\partial \bar{p}_1}{\partial \bar{\eta}} = 0, \tag{3.141}$$

$$\mathscr{Z}\rceil \;\; i(-1+\lambda\alpha_1\bar{\eta})\,\bar{w}_1 = T_0\bar{p}_1\frac{\mu_0}{2\bar{x}_1 T_0}\frac{\partial^2 \bar{w}_1}{\partial \bar{\eta}^2}, \tag{3.142}$$

which are independent on curvature effects. Equations (3.139)-(3.142) can be rearranged to obtain an equation for $\bar{v}_1(x_1,\bar{\eta})$

$$\left[\frac{\partial^2}{\partial \bar{\eta}^2} + i(1-\lambda\alpha_1\bar{\eta})\,\frac{2x_1T_0}{\mu_0}\right]\frac{\partial^2 \bar{v}_1}{\partial \bar{\eta}^2} = 0, \tag{3.143}$$

with solution (Ricco and Wu, 2007)

$$\frac{\partial \bar{v}_1}{\partial \bar{\eta}} = \int_{\eta_0}^{\hat{\eta}} \mathtt{Ai}(\breve{\eta})\mathrm{d}\breve{\eta}, \tag{3.144}$$

where $\hat{\eta} = \mathtt{C}\bar{\eta} + \eta_0$, $\eta_0 = -\mathtt{C}(\alpha_1\lambda)^{-1}$, and $\mathtt{C} = (2i\lambda\alpha_1 x_1 T_0/\mu_0)^{1/3}$.

Matching the solution of the main deck $\bar{v}_{\mathrm{MD}} = \kappa^{-1/2}v_1$ with the solution of the lower deck $\bar{v}_{\mathrm{LD}} = \bar{v}_1$ as

$$\lim_{\eta\to 0}\frac{\partial \bar{v}_{\mathrm{MD}}}{\partial \eta} = \lim_{\eta\to\infty}\frac{\partial \bar{v}_{\mathrm{LD}}}{\partial \eta}, \tag{3.145}$$

gives

$$\int_{\eta_0}^{\hat{\eta}} \mathtt{Ai}(\breve{\eta})\mathrm{d}\breve{\eta} = -i\lambda\alpha_1 A(x_1) \tag{3.146}$$

We now seek a balance equation at the wall. Rearranging (3.139)-(3.142) for $\bar{\eta} = 0$ and using the no-penetration condition $\bar{v}_1 = 0$,

$$\left.\frac{\partial^3 \bar{v}_1}{\partial \bar{\eta}^3}\right|_{\bar{\eta}=0} = \frac{2x_1 T_0^3}{\mu_0}\bar{p}_1. \tag{3.147}$$

Then, from (3.144) and using the chain rule

$$\frac{\partial^3 \bar{v}_1}{\partial \bar{\eta}^3} = \mathtt{C}^2\mathtt{Ai}'(\eta_0). \tag{3.148}$$

Therefore, the balance at the wall becomes

$$\mathtt{C}^2\mathtt{Ai}'(\eta_0) = \frac{2x_1 T_0^3}{\mu_0}\bar{p}_1, \tag{3.149}$$

which it will later be used to find the dispersion relation.

In the upper deck the wall-normal coordinate scales as $\tilde{\eta} = \kappa^{1/2}\eta$ and the solution becomes

$$\tilde{\mathbf{q}}(x_1, \tilde{\eta}) = \left(\kappa^{1/2}\tilde{u}_1,\, \kappa^{-1/2}\tilde{v}_1,\, \tilde{w}_1,\, \kappa^{-5/2}\tilde{p}_1,\, 0\right) E + \ldots. \tag{3.150}$$

Substituting (3.150) into the $\bar{x}$-LUBR equations we find the system of equations for the upper deck

$$\mathscr{C}\rceil \;\; i\alpha_1\tilde{u}_1 + \frac{\partial \tilde{v}_1}{\partial \tilde{\eta}} + \tilde{w}_1 = 0, \tag{3.151}$$

$$\mathscr{X}\rceil \;\; \tilde{u}_1 = 0, \tag{3.152}$$

$$\mathscr{Y}\rceil \;\; i\alpha_1\tilde{v}_1 + \frac{1}{2x_1}\frac{\partial \tilde{p}_1}{\partial \tilde{\eta}} = 0, \tag{3.153}$$

$$\mathscr{Z}\rceil \;\; i\alpha_1\tilde{w}_1 - \tilde{p}_1 = 0, \tag{3.154}$$

which, isolating $\tilde{p}_1$, gives a Laplace equation

$$\frac{1}{2x_1}\frac{\partial^2 \tilde{p}_1}{\partial \tilde{\eta}^2} - \tilde{p}_1 = 0, \tag{3.155}$$

and its relative solution $\tilde{p}_1 = p_1(x_1)e^{-(2x_1)^{1/2}\tilde{\eta}}$. Using (3.153), the wall-normal velocity is

$$\tilde{v}_1 = -\frac{ip_1}{\alpha_1(2x_1)^{1/2}}e^{-(2x_1)^{1/2}\tilde{\eta}}, \tag{3.156}$$

in which the curvature effects are also negligible in the limit $\kappa \ll 1$.

Matching the solution of the main deck $\bar{v}_{\text{MD}} = \kappa^{-1/2}v_1$ with the solution of the upper deck $\bar{v}_{\text{UP}} = \kappa^{-1/2}\tilde{v}_1$ as

$$\lim_{\eta\to 0}\bar{v}_{\text{UD}} = \lim_{\eta\to\infty}\bar{v}_{\text{MD}}, \tag{3.157}$$

gives

$$p_1 = A(x_1)\alpha_1^2(2x_1)^{1/2}. \tag{3.158}$$

Finally, knowing the solutions of the three decks, the dispersion relation is found by first substituting (3.158) into (3.149), which gives

$$\alpha_1 A = \mathtt{C}^2\mathtt{Ai}'\frac{\mu_0}{T_0^3}\frac{1}{\alpha_1(2x_1)^{3/2}}, \tag{3.159}$$

and then substituting (3.159) into (3.146) resulting in

$$\int_{\eta_0}^{\infty}\mathtt{Ai}(\breve{\eta})\mathrm{d}\breve{\eta} - (i\alpha_1)^{-1/3}\left[\frac{\lambda}{(2x_1)^{1/2}}\right]^{5/3}\left(\frac{\mu_0}{T_0^7}\right)^{1/3}\mathtt{Ai}' = 0. \tag{3.160}$$

Since the curvature effects are negligible for $\kappa \ll 1$, the dispersion relation (3.160) is the same as for the flat plate case of Ricco and Wu (2007). Numerically integrating (3.160) gives the local growth rate, proportional to $\mathtt{Im}(\alpha_1)$. The neutral curve is then identify by the streamwise location $\bar{x}_c$ where

$$\mathtt{Im}(\alpha_1) = 0. \tag{3.161}$$

This section was introduced to prove that the solution is independent on curvature for the high-frequency limit. Numerical results will be introduced in §4.4.

Chapter 4

Numerical results

In §4.1, we first present the results based on the LUBR equations valid for the entire evolution of the boundary-layer perturbation. We then discuss the comparison between the LUBR results with the results obtained through the EV framework valid for $\hat{x} \gg 1$ in §4.2 and the asymptotic results (ASY) valid for $\mathtt{G} \gg 1$ and $\hat{x} = \mathscr{O}(1)$ in §4.3. In §4.1.6, the LUBR results are compared qualitatively with the DNS results by Whang and Zhong (2003).

4.1 Unsteady boundary-region results

Using the LUBR equations, we investigate the dependence of the evolution of compressible Görtler vortices on four main parameters, i.e., the Mach number, the Görtler number, the ratio of the disturbance wavelengths in the free stream, and the frequency. In order to obtain realistic results, this parametric analysis is based on wind tunnel data of compressible flows.

4.1.1 Effect of Mach number

The effect of the Mach number is investigated while keeping the parameter $\mathtt{R}_u^* = U_\infty^*/\nu_\infty^*$ constant, which, in compressible flows experiments is referred to as the unit Reynolds number. As the free-stream mean velocity U_∞^* is changed, it directly affects both $\mathtt{M}$ and $\mathtt{R}_u^*$, p_∞^* affects $\mathtt{R}_u^*$ through a change of ν_∞^*, whereas T_∞^* changes $\mathtt{M}$ through the speed of sound $a_\infty^* = a_\infty^*(T_\infty^*)$ and $\mathtt{R}_u^*$ through ν_∞^*. The Reynolds number $\mathtt{R}_u^*$ is thus kept constant by selecting the correct

combination of U_∞^*, T_∞^*, and p_∞^* as the desired $\mathtt{M}$ is achieved. Figure 4.1 shows the influence of the free-stream temperature and pressure on the subsonic Mach number (left) and the free-stream kinematic viscosity (right).

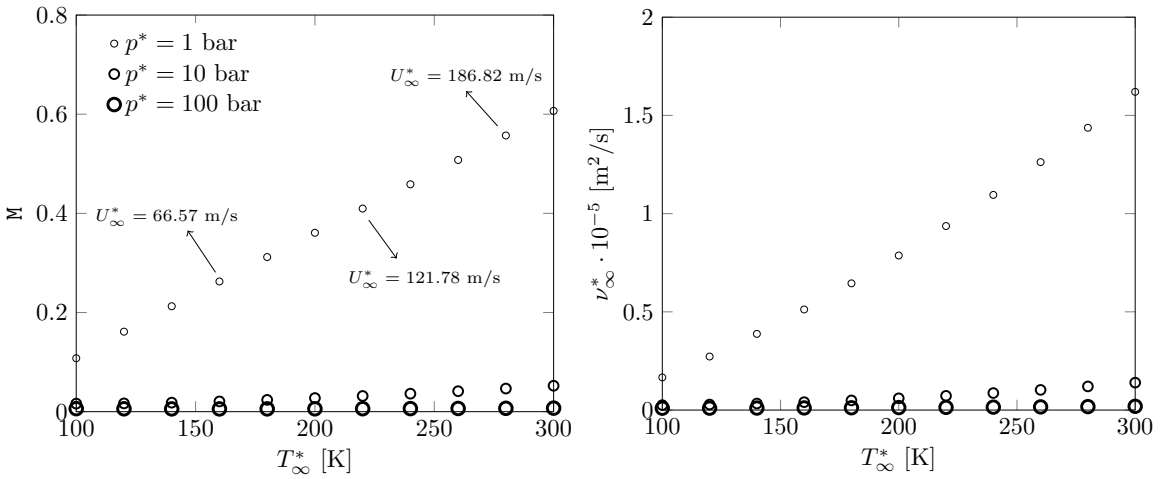

Fig. 4.1 Influence of pressure p_∞^* and temperature T_∞^* on the subsonic Mach number (left) and on the kinematic viscosity ν_∞^* of air (right) for $\mathtt{R}_u^* = 13 \cdot 10^6$ m^{-1}. The points in the two graphs correspond to the same flow conditions.

This approach has been used in several wind tunnel studies. Laufer (1954) conducted experiments in the supersonic wind tunnel of the Jet Propulsion Laboratory in the range $1.4 < \mathtt{M} < 4$, $\mathtt{R}_u^* = 13.3 \cdot 10^6$ m^{-1}, and a free stream dominated by vortical disturbances. No information on the pressure and temperature conditions was given in their article. Flechner et al. (1976) studied transitional boundary layers in the transonic tunnel at NASA Langley Research Center and maintained the stagnation temperature at 322 K. Three different Mach numbers $\mathtt{M} = 0.7, 0.8, 0.83$ were investigated through a change in the free-stream dynamic pressure while keeping $\mathtt{R}_u^* = 13.1 \cdot 10^6$ m^{-1}. This wind tunnel was equipped with a control system that allowed independent variation of Mach number, stagnation pressure, and temperature. We consider the cases of steady vortices ($f^* = 0$) in conditions similar to the experimental configuration of De Luca et al. (1993), i.e., with spanwise wavelength $\lambda_z^* = 8 \cdot 10^{-3}$m, corresponding to $\mathtt{R} = 1273.2$, and radius of curvature $r^* = 10$m, corresponding to $\mathtt{G} = 206.4$. The Mach number is limited to $\mathtt{M} \leq 4$ to maintain valid the assumptions of

ideal gas and constant Prandtl number. The dimensionless wall-normal coordinate $\bar{y} \equiv y^*/\delta^*_{99}$ is used when comparing results at different Mach numbers.

The maximum along $\bar{y}$ of the amplitude of the streamwise velocity perturbation $|\bar{u}(\hat{x})|_{\max} \equiv \max_{\bar{y}} |\bar{u}(\hat{x},\bar{y})|$ as a function of $\hat{x}$ is shown in figure 4.2 (left) for different $\mathtt{M}$. We recall that the velocities are normalized by the oncoming free-stream velocity U^*_∞. For $\hat{x} = \mathscr{O}(1)$, increasing $\mathtt{M}$ decreases the growth rate, i.e., the kinematic Görtler vortices ($\mathtt{G_V}$-vortices) become more stable, especially for supersonic flows. This confirms the asymptotic results for stage III. This is true only sufficiently downstream from the leading edge where the Görtler instability is fully developed and δ^* is comparable with λ^*_z. In the early stages of the streamwise-velocity perturbation where instead the spanwise viscous diffusion is negligible, the effect of the Mach number is reversed as shown in the inset of figure 4.2 (left). This confirms the theoretical results for stage II. The stabilizing effect of the Mach number when $\delta^* = \mathscr{O}(\lambda^*_z)$ is in accordance with early studies utilizing linearized theories for the primary instability (El-Hady and Verma, 1983; Hall and Malik, 1989; Hammerlin, 1961; Kobayashi and Kohama, 1977; Spall and Malik, 1989; Wadey, 1992). The most unstable Görtler vortices are therefore incompressible. However, this is true only during the initial stages of the evolution as the recent experimental study by Wang et al. (2018) showed that transition to turbulence is achieved more rapidly for compressible Görtler vortices compared to the slower transition of incompressible Görtler vortices because the secondary instability of nonlinearly evolving vortices is more intense in the compressible case.

In addition to $\mathtt{G_V}$-vortices, compressibility effects generate thermal Görtler vortices, hereinafter labeled $\mathtt{G_T}$-vortices. They originate due to the velocity-temperature coupling within the boundary layer even in the absence of free-stream temperature disturbances, similar to the thermal Klebanoff modes over a flat plate (Ricco and Wu, 2007). Figure 4.2 (right) reveals that the temperature perturbations also grow exponentially and are more stable sufficiently downstream, i.e., their growth rate decreases, as the Mach number increases. However, thanks to our receptivity framework we notice that in the proximity of the leading edge, where δ^* is smaller than λ^*_z, the temperature perturbations increase much more significantly with the Mach number than the velocity perturbations. We further note that

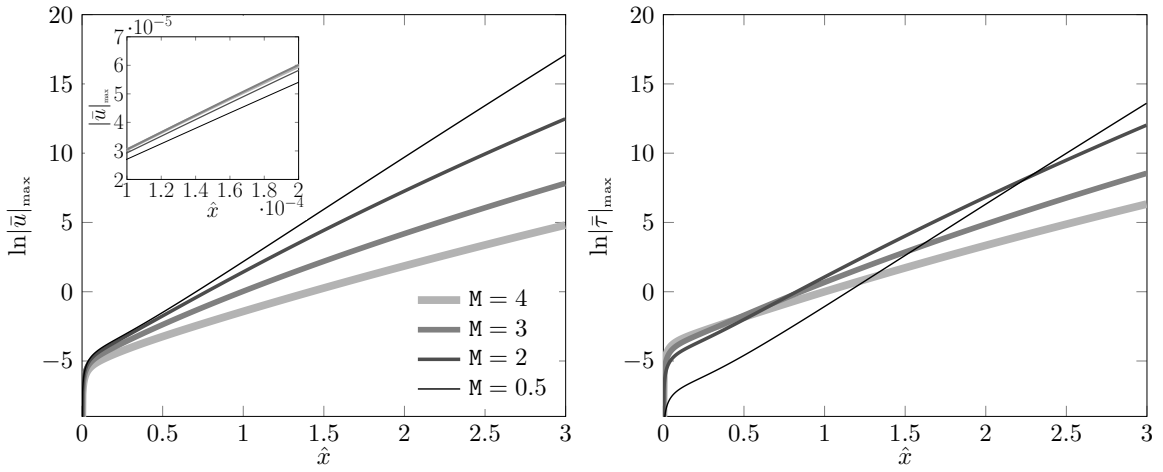

Fig. 4.2 The effect of the Mach number on the maximum streamwise velocity perturbation (left) and the maximum temperature perturbation (right) for a steady flow at $\mathtt{R} = 1273.2$, $\mathtt{G} = 206.4$ and $k_y = 1$.

the stabilizing effect of the Mach number occurs much further upstream for the $\mathtt{G_V}$-vortices than for the $\mathtt{G_T}$-vortices. Since further downstream the growth rate decreases with increasing $\mathtt{M}$, temperature perturbations for lower $\mathtt{M}$ become dominant when $\hat{x}$ is sufficiently high. This reversed influence of compressibility caused by the growing presence of spanwise viscous diffusion along the streamwise direction was also detected on thermal Klebanoff in the presence of wall heat transfer (Ricco et al., 2009). None of the previous theoretical frameworks could trace the evolution of both the velocity and the temperature perturbations from the leading edge and observe this effect of spanwise diffusion because local EV approaches were utilized without considering the influence of the base-flow receptivity to external disturbances on the evolution of the Görtler vortices.

The location of the maximum value of the perturbation amplitudes is monitored to identify the wall-normal position of the Görtler vortices. Early studies by Kobayashi and Kohama (1977), El-Hady and Verma (1983), and Ren and Fu (2015) show that the vortices lift away from the wall as the Mach number increases, although through EV approaches they could not trace the evolution of the vortices from the leading edge because the external forcing due to the free-stream disturbances plays a crucial role there. This effect of compressibility on Görtler vortices was also noticed by Spall and Malik (1989), Hall and Fu (1989), and Wadey (1992). Previous studies have shown that in the limit of large Mach number the vortices move

into a log-layer near the free stream. However, as we focus on $\mathtt{M} = \mathscr{O}(1)$, this lifting effect of the Mach number is not intense enough and the vortices are only confined in the core of the boundary layer. Thanks to our receptivity framework, we can follow the wall-normal location of $\mathtt{G_V}$-vortices and $\mathtt{G_T}$-vortices as they evolve from the leading edge. Figure 4.3 confirms that by increasing the Mach number the $\mathtt{G_V}$-vortices (left) and the $\mathtt{G_T}$-vortices (right) occur at larger wall-normal locations. The effect of $\mathtt{M}$ is stronger for the $\mathtt{G_V}$-vortices than on the $\mathtt{G_T}$-vortices and the $\mathtt{G_T}$-vortices are positioned closer to the free stream than the $\mathtt{G_V}$-vortices. The increase of boundary-layer thickness δ^*_{99} with $\mathtt{M}$ is also shown in the inset of Figure 4.3 (right).

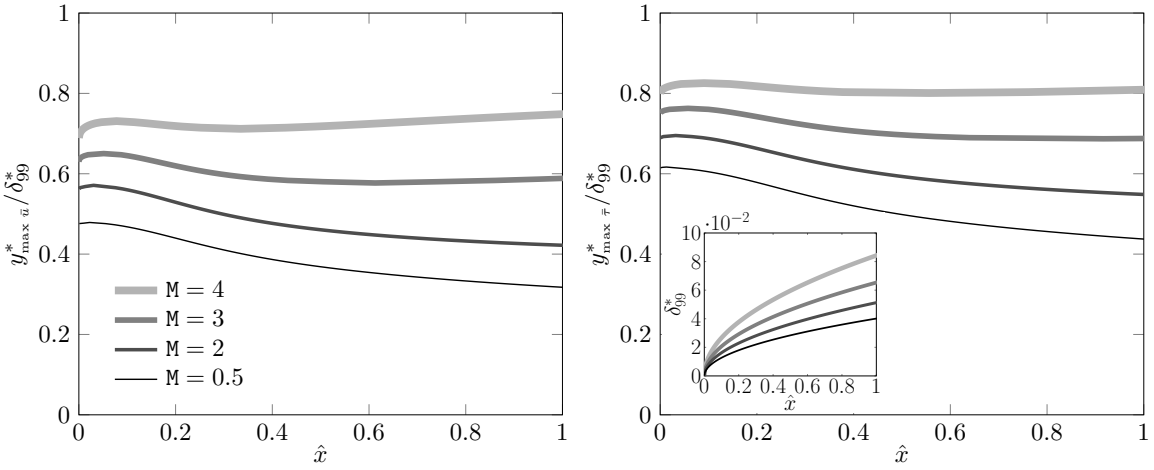

Fig. 4.3 The effect of the Mach number on the wall-normal location of $\mathtt{G_V}$-vortices (left) and $\mathtt{G_T}$-vortices (right) for a steady flow at $\mathtt{R} = 1273.2$, $\mathtt{G} = 206.4$ and $k_y = 1$. Inset: Boundary-layer thickness based on $\lambda^*_z = 8 \cdot 10^{-3}$m, expressed in meters.

As shown by Hall (1983) and Wu et al. (2011), incompressible Görtler vortices move closer to the surface as they evolve downstream and they become confined in the wall layer region. This behavior persists even for compressible flows as long as $\mathtt{M} < 3$. For $\mathtt{M} \geq 3$ the vortices are not confined near the wall but they evolve in the core of the boundary layer. The asymptotic results of stage III, which are based on the assumption $\mathtt{G} \gg 1$, cannot capture this behavior because vortices tend to shift towards the wall as $\mathtt{G}$ increases for any Mach number when $\mathtt{M} = \mathscr{O}(1)$.

Figure 4.4 shows the streamwise velocity perturbation profiles (left) and the spanwise velocity perturbation profiles (right) for $\mathtt{M} = 2$ and $\mathtt{M} = 4$. Both the streamwise and the

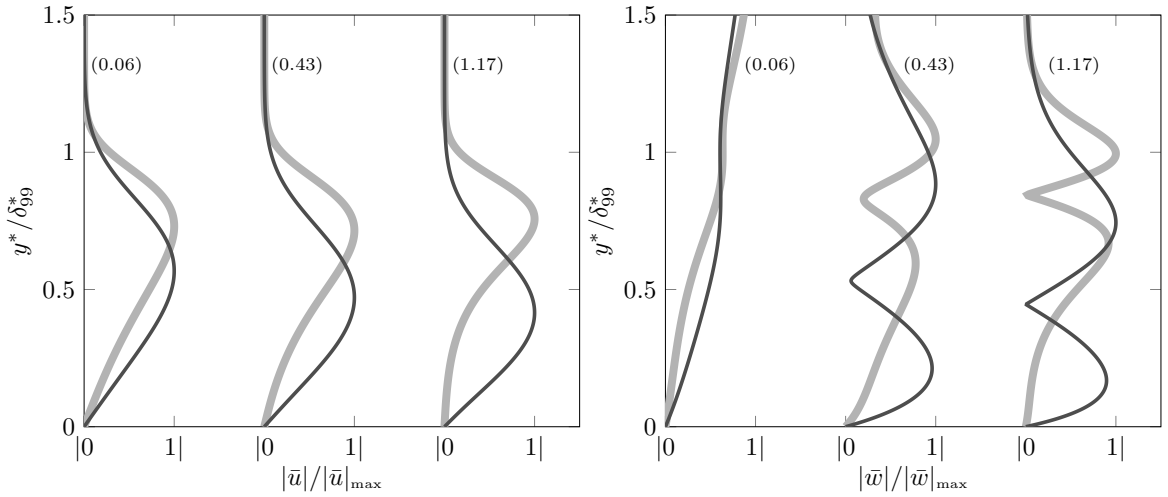

Fig. 4.4 The effect of the Mach number M, $\mathtt{M} = 2$ (—) and $\mathtt{M} = 4$ (▬), on the normalized profiles of the streamwise velocity perturbation (left) and the spanwise velocity perturbation (right) for a steady flow at $\mathtt{R} = 1273.2$, $\mathtt{G} = 206.4$ and $k_y = 1$. Numbers in the parenthesis correspond to the streamwise location $\hat{x}$.

spanwise velocity profiles show that the perturbations move towards the wall for $\mathtt{M} = 2$ and remain confined in the core of the boundary layer for $\mathtt{M} = 4$. For this higher Mach number, the velocity gradient at the wall tends to zero as $\hat{x}$ increases, generating a near-wall region where the flow is largely unperturbed. Consequently, for $\mathtt{M} > 3$ approximately the wall-shear stress of the perturbation is not a sound indicator for the growth of thermal Görtler vortices, while it is effective in the incompressible regime (Hall, 1983, 1990). Temperature profiles behave similarly to the streamwise velocity profiles and their peak shifts slightly towards the free stream.

4.1.2 Effect of Görtler number

In the context of steady vortices, we now analyze the effect of the Görtler number on the evolution of perturbations for $\mathtt{M} = 2$ and $\mathtt{M} = 4$. Keeping $\mathtt{R} = 1273.2$, radii of curvature $r^* = 5$m and $r^* = 10$m gives $\mathtt{G} = 412.8$ and $\mathtt{G} = 206.4$, respectively.

In §3.2.1 we introduced the parameter $\beta(\hat{x})$ (Viaro and Ricco, 2018) and the streamwise location $\hat{x}_\mathtt{K}$ where the perturbation shifts to Görtler vortices. The effect of G and M on $\hat{x}_\mathtt{K}$ is shown in table 4.1. The location $\hat{x}_\mathtt{K}$ decreases as G increases for all M and for subsonic

	$\mathtt{M}=0$	$\mathtt{M}=0.5$	$\mathtt{M}=2$	$\mathtt{M}=3$	$\mathtt{M}=4$
$\mathtt{G}=206.4$	0.083	0.083	0.08	0.095	0.099
$\mathtt{G}=412.8$	0.052	0.052	0.048	0.049	0.053
$\mathtt{G}=825.6$	0.033	0.033	0.031	0.031	0.032

Table 4.1 Streamwise locations $\hat{x}_{\mathtt{K}}$ for different values of the Görtler number $\mathtt{G}$ and the Mach number $\mathtt{M}$ for a steady flow with $\mathtt{R}=1273.2$ and $k_y=1$.

conditions there is no Mach number influence to the level of accuracy chosen. For supersonic conditions and low enough $\mathtt{G}$, $\hat{x}_{\mathtt{K}}$ increases with $\mathtt{M}$, but $\hat{x}_{\mathtt{K}}$ becomes independent on $\mathtt{M}$ in supersonic conditions if $\mathtt{G}$ is sufficiently large.

Klebanoff modes contribute to the initial growth of the perturbation and, for sufficiently small Görtler numbers, i.e., $\mathtt{G}<50$ for $\mathtt{M}=4$, they stabilize after a certain streamwise location, as shown in figure 4.5. Only when $\mathtt{G}$ is large enough the instability is characterized by the more energetic Görtler vortices. This is confirmed by the recent experimental study of Wang et al. (2018) where for low $\mathtt{G}$ values only weak streaky structures are present but when $\mathtt{G}$ increases the Görtler instability generates stronger vortices. Figure 4.5 also shows that, as the Görtler number increases, $\mathtt{G}_{\mathtt{T}}$-vortices (right) are more unstable than $\mathtt{G}_{\mathtt{V}}$-vortices (left) at $\mathtt{M}=4$.

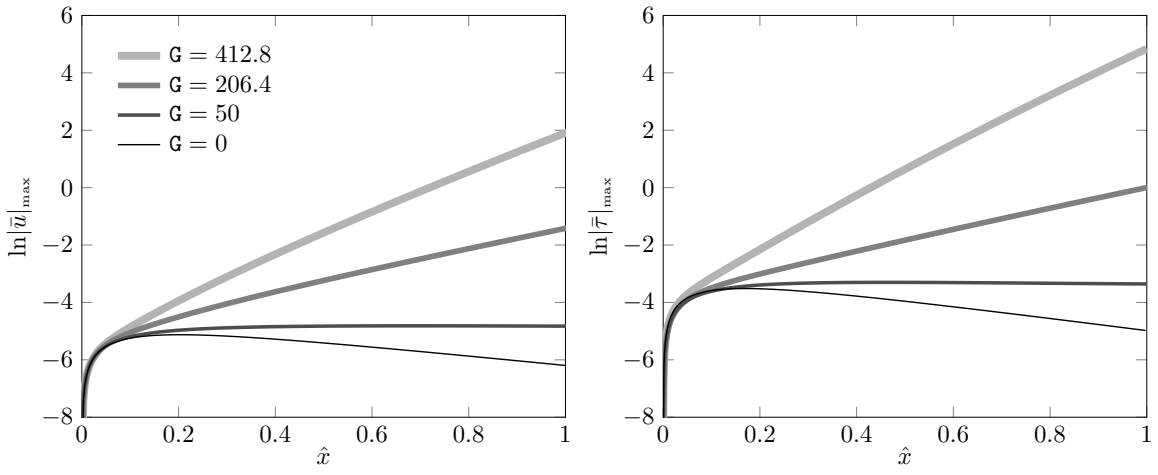

Fig. 4.5 The effect of the Görtler number $\mathtt{G}$ on the maximum streamwise velocity perturbation (left) and temperature perturbation (right) for a steady flow with $\mathtt{M}=4$, $\mathtt{R}=1273.2$ and $k_y=1$.

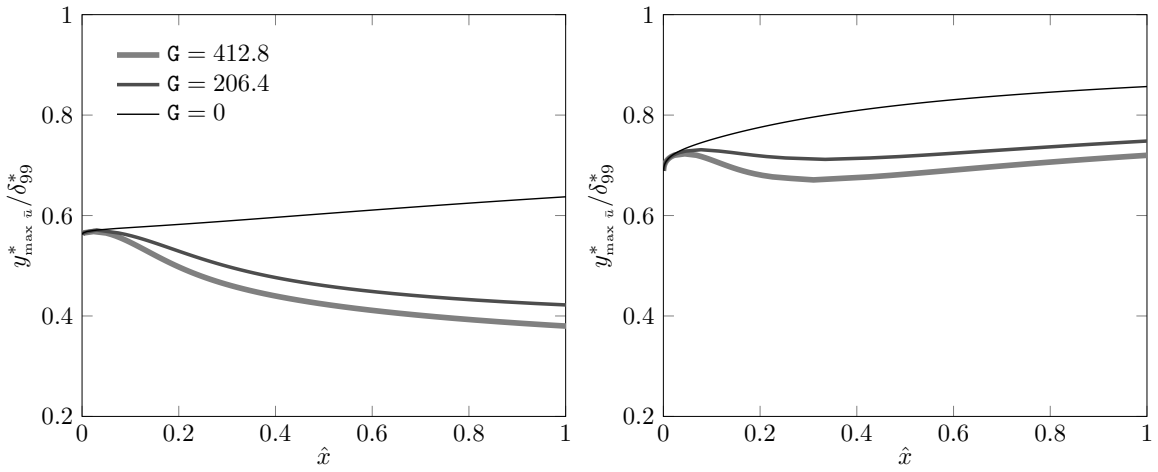

Fig. 4.6 The effect of the Görtler number G on the wall-normal location of $\mathtt{G}_\mathtt{V}$-vortices at M = 2 (left) and M = 4 (right) for a steady flow with R = 1273.2 and $k_y = 1$.

The location of $\mathtt{G}_\mathtt{V}$-vortices is shown in figure 4.6 for M = 2 (left) and M = 4 (right). When G increases the vortices move closer to the wall whereas when M increases they move away from the wall. High Mach number flows tend to behave more similarly to the flat-plate scenario.

The influence of the Mach number changes as the Görtler number increases. The asymptotic analysis reveals that for $\mathtt{G} \gg 1$ an increase of the Mach number makes the vortices move towards the wall. This was also noticed by Dando and Seddougui (1993) and it is confirmed by the LUBR results for high Görtler numbers. Table 4.2 schematically shows that, when $\hat{x}$ is held fixed and the Mach number is subsonic or mildly supersonic and increases, the vortices shift towards the boundary-layer core only when $\mathtt{G} = \mathscr{O}(1)$. In addition, the position of the vortices as $\hat{x}$ increases is affected by the Mach number being smaller or larger than 3 for $\mathtt{G} = \mathscr{O}(1)$, as shown in figure 4.3.

Figure 4.7 (top) shows the streamwise velocity and temperature perturbation profiles at different streamwise locations. These profiles highlight the unperturbed near-wall regions for M = 4 caused by $\mathtt{G}_\mathtt{V}$-vortices and $\mathtt{G}_\mathtt{T}$-vortices moving towards the free stream. The peaks in the profiles experience only a minor shift towards the wall as G increases due to the high Mach number. Like for the Mach number effects, the influence of G increases as the solution evolves downstream. The wall-normal velocity perturbation and the spanwise velocity perturbation

M	G	$\hat{x}$	Vortex dynamics
$\approx 1 \uparrow$	$\mathscr{O}(1)$	$\mathscr{O}(1)$	$\rightarrow$ boundary-layer core
$\approx 1 \uparrow$	$\gg 1$	$\mathscr{O}(1)$	$\rightarrow$ wall
≈ 1	$\uparrow$	$\mathscr{O}(1)$	$\rightarrow$ wall
< 3	$\mathscr{O}(1)$	$\mathscr{O}(1) \uparrow$	$\rightarrow$ wall
≥ 3	$\mathscr{O}(1)$	$\mathscr{O}(1) \uparrow$	$\rightarrow$ boundary-layer core

Table 4.2 Influence of G, M, and $\hat{x}$ on the location of the Görtler vortices. Upward arrows ($\uparrow$) indicate increasing values and horizontal arrows ($\rightarrow$) denote the vortices moving towards the wall or the boundary-layer core.

represent the weak crossflow of the Görtler instability. These profiles, shown in figure 4.7 (bottom) for different values of G, demonstrate that even though the free-stream vortical disturbance decreases exponentially in the streamwise direction, as described by (3.16) and (3.17), the perturbations inside the boundary layer soon become self-sustained when curvature effects become relevant. The wall-normal velocity profiles present a single peak at $\eta \approx 2$ whereas the spanwise velocity profiles, which are more affected by G, show the double-peak characteristic of the longitudinal counter-rotating $\mathrm{G_V}$-vortices. As in the case of the streamwise perturbation velocity, the solution for $\hat{x} = 0.06$ differs only slightly from the flat plate one, proving that the influence of curvature is still weak. The confinement of $\mathrm{G_V}$-vortices for into the core of the boundary layer is also visible from the crossflow velocity profiles of figure 4.7 (bottom).

Previous studies have investigated how changes of G affect the solution as M increases. The EV approach of El-Hady and Verma (1983) demonstrates that Görtler vortices are more sensitive to changes in G as M increases. On the contrary, we show that Görtler vortices are less sensitive to changes in G as M increases (e.g., refer to figure 4.6), which is in agreement with the results of Spall and Malik (1989).

4.1.3 Effect of the free-stream wavelength ratio

The effect of the free-stream wavelength ratio $k_y = \lambda_z^*/\lambda_y^*$ can only be studied through the receptivity formalism because k_y only appears in the initial and free-stream boundary

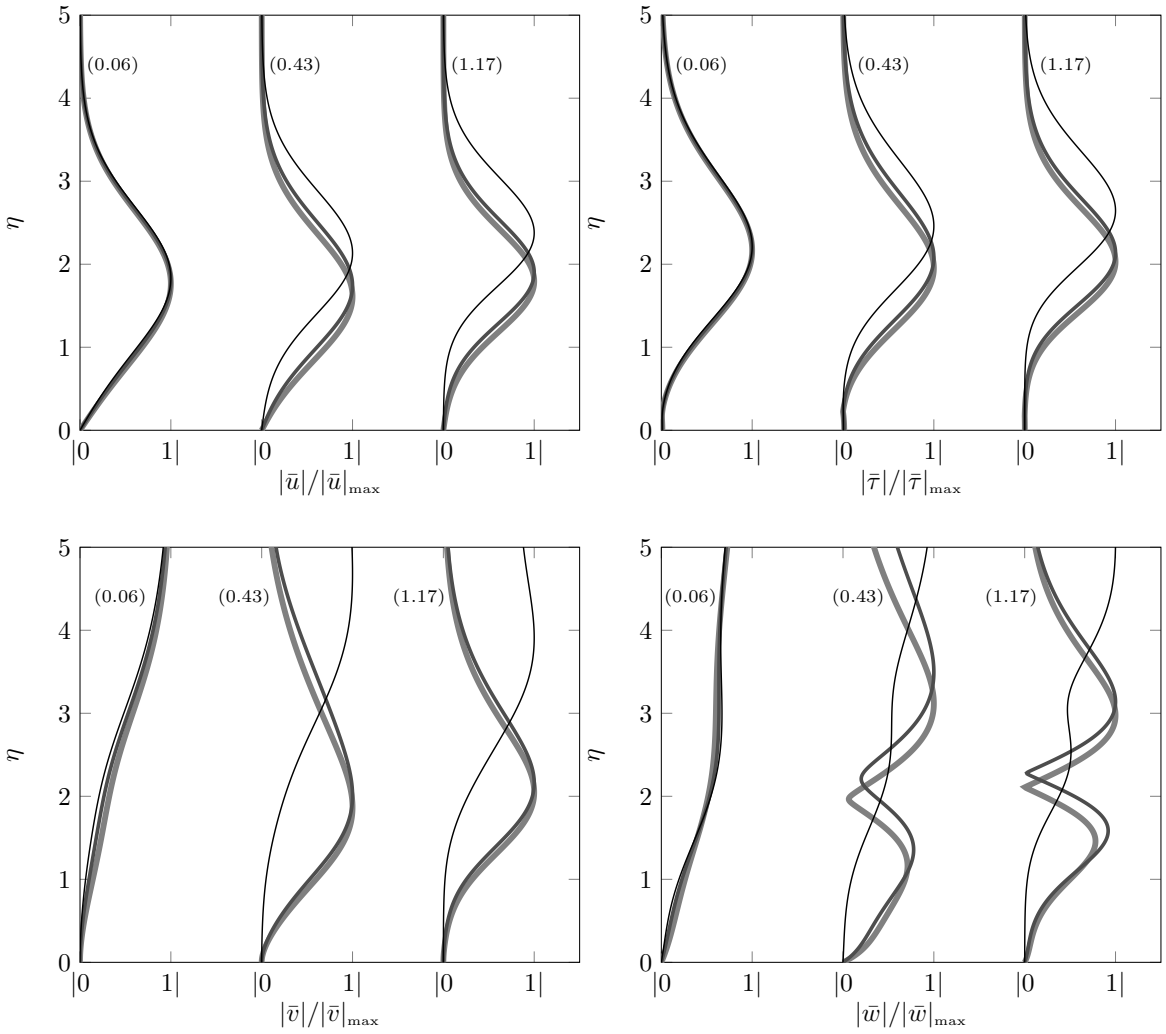

Fig. 4.7 The effect of the Görtler number $\mathtt{G}$, $\mathtt{G} = 0$ (—), $\mathtt{G} = 206.4$ (—) and $\mathtt{G} = 412.8$ (—), on the normalized profiles of the streamwise velocity perturbation (top left), the temperature perturbation (top right), the wall-normal velocity perturbation (bottom left) and the spanwise velocity perturbation (bottom right) for a steady flow at $\mathtt{R} = 1273.2$, $\mathtt{M} = 4$ and $k_y = 1$. Numbers in the parenthesis correspond to the streamwise location $\hat{x}$.

conditions, equations (3.20)-(3.24) and (3.14)-(3.19), respectively. Figure 4.8 shows the effect of k_y on the streamwise perturbation velocity (left) and the wall-normal location of $\mathtt{G_V}$-vortices (right) for $\mathtt{M} = 4$ and $\mathtt{G} = 206.4$. The weak effect of k_y increases at higher Mach numbers (not shown). The flow becomes slightly more stable as k_y increases, with the most unstable configuration achieved for $k_y = 0$. The growth rate of the streamwise velocity becomes nearly constant for sufficiently high $\hat{x}$. When the flow is more stable

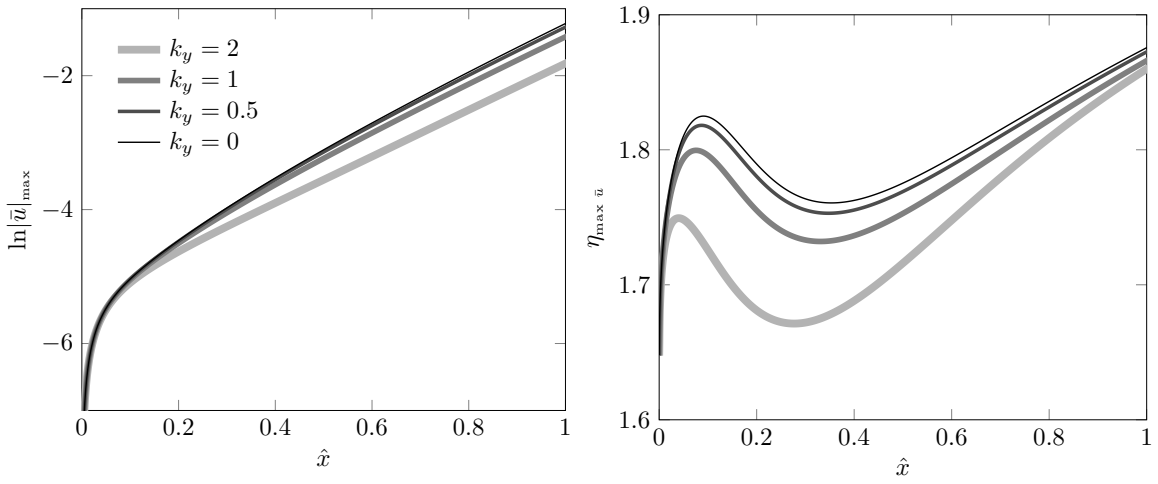

Fig. 4.8 The effect of k_y on the maximum streamwise velocity perturbation (left) and wall-normal location of $\mathtt{G_V}$-vortices (right) for a steady flow at $\mathtt{R} = 1273.2$, $\mathtt{G} = 206.4$ and $\mathtt{M} = 4$.

as k_y increases, the vortices initially tend to shift towards the wall but their wall-normal position becomes independent on k_y at sufficiently high values of $\hat{x}$, as shown in figure 4.8 (right). Contrary to the effect of Mach number and Görtler number, the influence of k_y on the wall-normal position of the vortices decreases as the streamwise location increases. Spall and Malik (1989) also noted that, for different initial conditions, the growth rates converged at sufficiently high scaled wavenumbers, i.e., sufficiently downstream, and that this convergence occurs closer to the leading edge as $\mathtt{G}$ increased. The normalized streamwise velocity and the temperature profiles experience no significant variations as k_y changes whereas the profiles of the crossflow velocities vary with k_y but only at small streamwise locations (not shown).

4.1.4 Effect of frequency

The effect of frequency at two different Mach numbers, $\mathtt{M} = 0.5$ and $\mathtt{M} = 3$, is investigated by keeping a constant dimensionless wavenumber $\kappa = k_z/(k_x \mathtt{R})^{1/2} = \mathscr{O}(1)$ which, for $\hat{x} = \mathscr{O}(1)$, is representative of the ratio $\delta^*/\lambda_z^* = \mathscr{O}(1)$, i.e., the spanwise and the wall-normal diffusion effects are of the same order. Flows at different Görtler numbers are also compared for $r^* = 5$m and $r^* = 10$m. For the subsonic case the Görtler numbers are $\mathtt{G} = 2494.7$ and $\mathtt{G} = 1247.3$, whereas, for the supersonic case, $\mathtt{G} = 479.4$ and $\mathtt{G} = 239.7$, respectively. The

M	G	f^* [Hz]	$\mathrm{F}\cdot 10^{-7}$	λ_z^* [m]	R	$k_x\cdot 10^{-5}$	κ	δ_c^* [m]
0.5	1247.3 | 2494.7	125	0.66	0.0029	5157.51	215	0.3000	0.002
		250	**1.32**			430	**0.2125**	
		500	2.64			860	0.1503	
3	239.7 | 479.4	500	3.75	0.005	1735.66	640	0.3000	0.009
		1000	**7.49**			1280	**0.2125**	
		2000	14.98			2560	0.1503	

Table 4.3 Flow parameters from wind tunnel data used for the analysis of the unsteady Görtler instability at $r^* = 5$m and $r^* = 10$m. Reference cases are in bold.

frequency is scaled as

$$\mathrm{F} \equiv \frac{f^*}{\mathrm{R}_u^* U_\infty^*}, \tag{4.1}$$

where the unit Reynolds numbers are $\mathrm{R}_u^* = 11\cdot 10^6$ m^{-1} and $\mathrm{R}_u^* = 2.18\cdot 10^6$ m^{-1} for a subsonic case (Flechner et al., 1976) and a supersonic case (Graziosi and Brown, 2002), respectively. For each Mach number, the effect of frequency is studied by doubling and halving a reference frequency from wind tunnel experiments for supersonic and subsonic flows. At $\mathrm{M} = 3$, the reference frequency $f^* = 1000$Hz ($\mathrm{F} = 7.5\cdot 10^{-7}$) comes from the work of Graziosi and Brown (2002), which corresponds to the maximum perturbation energy. Given that no experiments were found for $\mathrm{M} = 0.5$, the reference frequency $f^* = 250$Hz ($\mathrm{F} = 1.32\cdot 10^{-7}$) was inferred from the knowledge of frequencies at very low Mach numbers (Boiko et al., 2010b), $f^*_{\max} \approx 20$Hz, and at high Mach numbers (Graziosi and Brown, 2002), $f^*_{\max} \approx 10$kHz. This value additionally allows us to compare the same frequency, $f^* = 500$Hz, in the two Mach numbers considered. The parameters used to investigate the effect of frequency are summarized in table 4.3, along with the estimation of the boundary-layer displacement thickness $\delta_c^* = \delta_i^* + 1.192(\gamma-1)\mathrm{M}^2 x^*_{\max}/\mathrm{R}^{0.5}$ (Stewartson, 1964), where δ_i^* is the displacement thickness for incompressible flows and $x^*_{\max} = 2$m.

Figure 4.9 shows the stabilizing effect of increasing the frequency on the temperature perturbation while keeping a constant radius of curvature $r^* = 5$m. The stabilizing effect of doubling the reference frequencies is stronger compared to the destabilizing effect of halving them, for both Mach numbers and for $r^* = 10$m (not shown). The same conclusions can be

drawn for the maximum velocity perturbation $|\bar{u}(\hat{x})|_{\max}$, which also agree with the findings of Hall (1990) and Ren and Fu (2015).

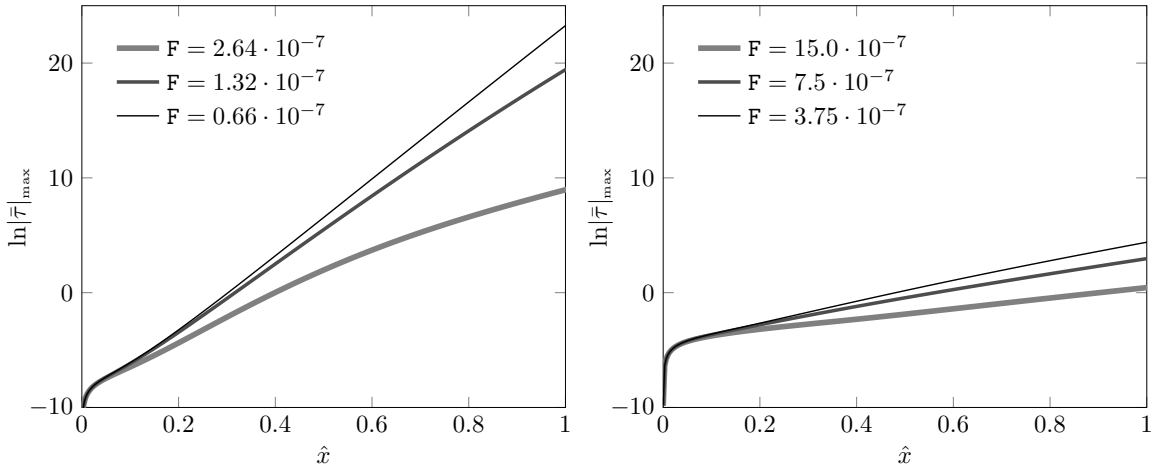

Fig. 4.9 The effect of the frequency F on the maximum temperature perturbation for a plate with $r^* = 5$m and $k_y = 1$, at $\mathtt{M} = 0.5$, $\mathtt{G} = 2494.7$ (left) and $\mathtt{M} = 3$, $\mathtt{G} = 479.4$ (right).

Frequency plays an important role on the location of Görtler vortices. As the main effect of increasing the frequency is to move the vortices away from the wall, figure 4.10 (left) shows that, even for low Mach numbers, $\mathtt{G}_\mathtt{T}$-vortices are not confined near the wall if the frequency is high enough. At high Mach numbers, the effect of frequency on the location of $\mathtt{G}_\mathtt{T}$-vortices is more intense and starts closer to the leading edge, as shown in figure 4.10 (right). $\mathtt{G}_\mathtt{V}$-vortices are located closer to the wall with a weaker dependence on the frequency than $\mathtt{G}_\mathtt{T}$-vortices (not shown).

To summarize, Görtler vortices tend to move towards the boundary-layer core when the perturbation is more stable, i.e., as F, M increase, or G decreases. However, as k_y increases, the perturbation is slightly more stable and Görtler vortices tend to move closer to the wall.

4.1.5 Growth rate and streamwise length scale of the perturbation

From the solution of the LUBR equations, the streamwise velocity of the perturbation $\bar{u} = \bar{u}(\hat{x}, \eta)$ can be used to compute the complex parameter $\sigma = \sigma_{\text{Re}} + i\,\sigma_{\text{Im}}$ as

$$\sigma(\hat{x}, \eta) = \frac{1}{\bar{u}} \frac{\partial \bar{u}}{\partial \hat{x}}\bigg|_{\eta}, \tag{4.2}$$

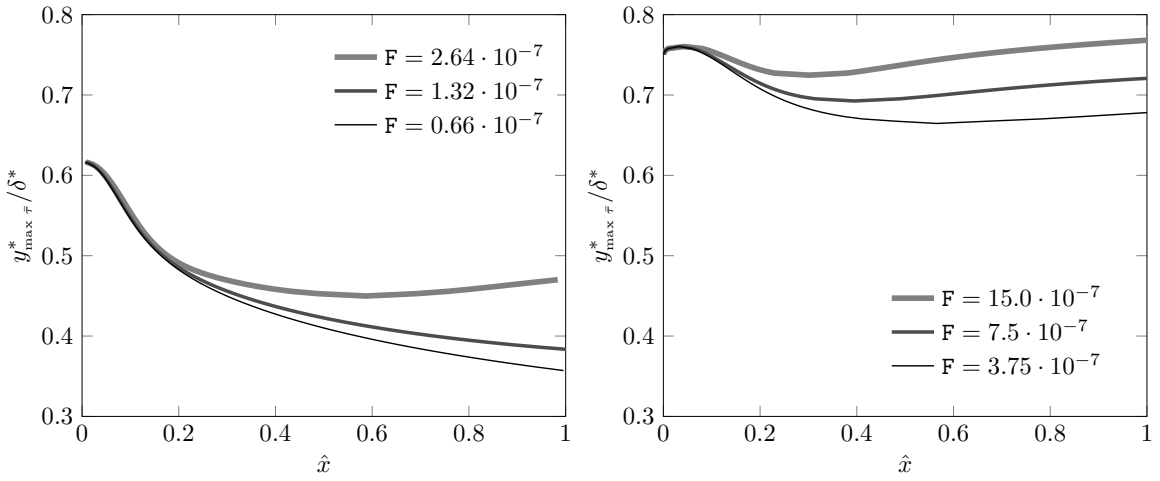

Fig. 4.10 The effect of the frequency $\mathtt{F}$ on the wall-normal location of $\mathtt{G_T}$-vortices for a plate with $r^* = 5$m and $k_y = 1$, at $\mathtt{M} = 0.5$, $\mathtt{G} = 2494.7$ (left) and $\mathtt{M} = 3$, $\mathtt{G} = 479.4$ (right).

where σ_{Re} is the growth rate and σ_{Im} is proportional to the inverse of the streamwise length scale. In the EV framework, applying the decomposition (3.26) to (4.2) gives $\sigma = \sigma_{\text{EV}}(\hat{x})$. However, figure 4.11 shows that the perturbation inside the boundary layer grows at different rates at different wall-normal locations η, with the maximum growth rate located at $\eta \approx 2$. The dependence on η is more intense closer to the leading edge and decreases at large $\hat{x}$.

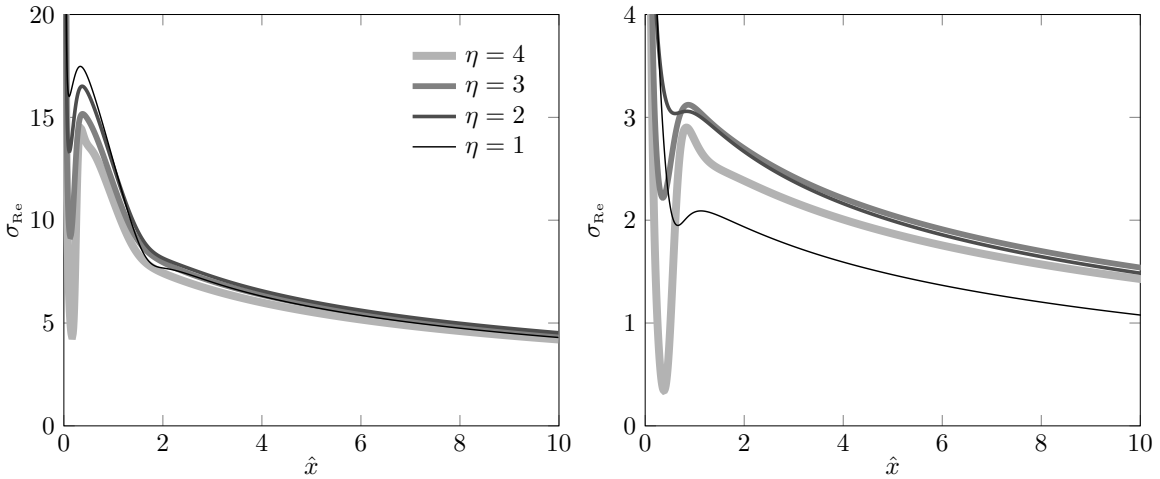

Fig. 4.11 Influence of η on $\sigma_{\text{Re}}(\hat{x}, \eta)$ for $\mathtt{M} = 0.5$, $\mathtt{G} = 1247.3$, $k_y = 1$, $\mathtt{F} = 1.32 \cdot 10^{-7}$ (left) and $\mathtt{M} = 3$, $\mathtt{G} = 239.7$, $k_y = 1$, $\mathtt{F} = 7.5 \cdot 10^{-7}$ (right).

However, even at values of $\hat{x} = 10$ the influence of η is still not negligible, especially in supersonic conditions. The relative difference $\Delta\sigma_{\text{Re}}$ between the maximum and minimum

value of $\sigma_{\mathrm{Re}}(\hat{x},\eta)$ at $\hat{x}=10$, i.e., $\Delta\sigma_{\mathrm{Re}}=(\sigma_{\mathrm{Re,max}}-\sigma_{\mathrm{Re,min}})/\sigma_{\mathrm{Re,max}}$, is $\Delta\sigma_{\mathrm{Re}}=7.2\%$ and $\Delta\sigma_{\mathrm{Re}}=29.9\%$ for $\mathtt{M}=0.5$ and $\mathtt{M}=3$, respectively. This is confirmed by figure 4.11 (right) where the lowest growth rate is for the perturbation closest to the wall.

The imaginary part of (4.2), $\sigma_{\mathrm{Im}}(\hat{x},\eta)$, can be used to define the streamwise length scale of the boundary-layer perturbation as

$$\lambda_{x,\mathrm{bl}}(x,\eta)\equiv\frac{2\pi}{\sigma_{\mathrm{Im}}(\hat{x},\eta)}\mathtt{R}, \tag{4.3}$$

which, as shown schematically in figure 3.1, is linked to λ_x through receptivity, the constant streamwise wavelength of the free-stream disturbance. The parameter

$$\mathscr{L}_x(x,\eta)\equiv\frac{\lambda_{x,\mathrm{bl}}}{\lambda_x}=\frac{k_x\,\mathtt{R}}{\sigma_{\mathrm{Im}}(\hat{x},\eta)} \tag{4.4}$$

can therefore be defined in order to show the influence of the oncoming disturbance to the perturbation inside the boundary layer. For all cases considered $\mathscr{L}_x<1$, which means that the streamwise boundary-layer length scale is always smaller than the streamwise free-stream wavelength. Figure 4.12 also shows that the streamwise length scale ratio $\mathscr{L}_x$ depends on η for $\mathtt{M}=0.5$ (left) and for $\mathtt{M}=3$ (right). For both configurations, $\mathscr{L}_x$ decreases with $\hat{x}$ near the leading edge, but then increases as the perturbation evolves, i.e., $\lambda_{x,\mathrm{bl}}$ approaches λ_x further downstream. As the Mach number increases $\mathscr{L}_x$ becomes closer to unity, as shown in figure 4.12 (right). Increasing the frequency also has the same effect (not shown). Therefore, the more unstable the perturbation is, the more $\lambda_{x,\mathrm{bl}}$ differs from λ_x.

4.1.6 Qualitative comparison with DNS data

The lack of experimental data for compressible Görtler flows makes it difficult to validate our results. We here carry out a qualitative comparison with the DNS data by Whang and Zhong (2003), who first studied the response of a hypersonic boundary layer ($\mathtt{M}=15$) over a concave surface to free-stream vortical and acoustic disturbances. As the Mach number in their simulations is much higher than ours due to the limitations of our code to relatively

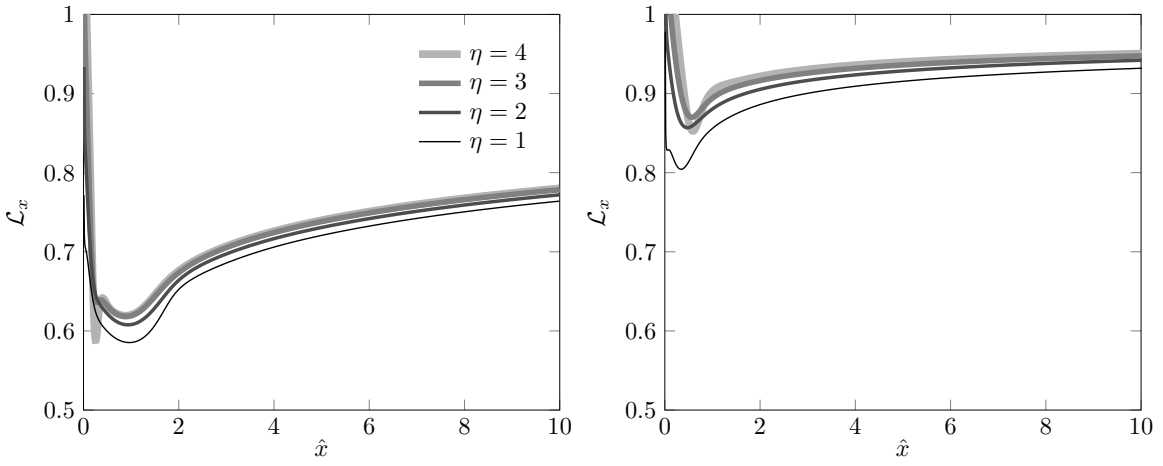

Fig. 4.12 Influence of η on $\mathscr{L}_x(x,\eta)$ for $\mathtt{M} = 0.5$, $\mathtt{G} = 1247.3$, $k_y = 1$, $\mathtt{F} = 1.32 \cdot 10^{-7}$ (left) and $\mathtt{M} = 3$, $\mathtt{G} = 239.7$, $k_y = 1$, $\mathtt{F} = 7.5 \cdot 10^{-7}$ (right).

small Mach numbers, quantitative agreement with our moderate supersonic data would not be possible. Nevertheless, our receptivity results are useful because they explain the physics of the instability observed by Whang and Zhong (2003) and we expect that a DNS simulation at $\mathtt{M} = 4$ would recover the results found with our LUBR simulations. In their work, the DNS data are compared with data from linear eigenvalue stability theory. As we have shown, this latter approach cannot fully capture the physics of the vortices, especially near the leading edge, where the effect of the free-stream perturbation is crucial.

Figure 4.13 presents the evolution of the amplitude of the steady streamwise and temperature perturbations obtained by Whang and Zhong (2003) (left) and by our LUBR simulations (right). Values are normalized by the first peak value of the streamwise velocity. The streamwise velocity perturbation and the temperature perturbation evolve in similar fashion, showing the initial algebraic growth due to the streaks, followed by viscous decay and by the Görtler instability downstream. These three phases have been reported by Viaro and Ricco (2018) to occur at sufficiently low Görtler number to detect a competing effect between the damping action of the viscous effects and the centrifugal instability. Consistently with our results on the effect of Mach number, the temperature perturbations become larger and larger than the velocity perturbations as the Mach number grows.

Whang and Zhong (2003) refer to the first growing phase as an early transient growth due to leading-edge effects and correctly identify the Görtler vortices as responsible for the subsequent instability following the intermediate decay. They also point out that, according to the linear stability theory, the region near the leading edge should be stable and the growth of disturbances should be absent. All these observations match our theoretical predictions. Our eigenvalue analysis indeed predicts decay near the leading edge where instead the direct forcing from the free stream creates a transient growth. We can then describe the initial growth reported by Whang and Zhong (2003) as the thermal and kinematic Klebanoff modes, which are always present from the leading edge at every Görtler number (Viaro and Ricco, 2018) and are caused by the free-stream receptivity, i.e., the continuous action of the free-stream vortical disturbances, and not only by a leading-edge effect as stated by Whang and Zhong (2003).

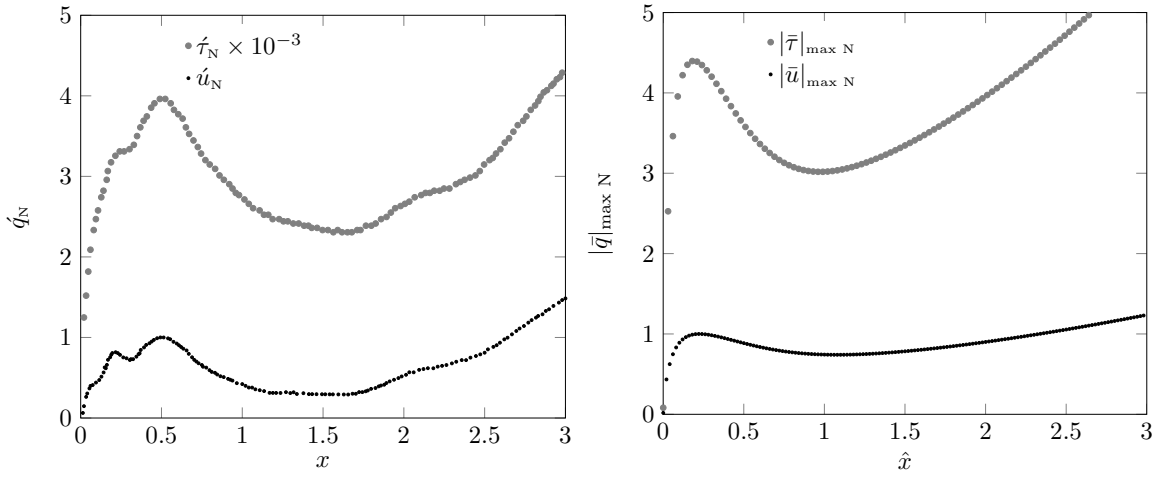

Fig. 4.13 Comparison of velocity and temperature perturbations relative to the DNS data of Whang and Zhong (2003) at $\mathtt{M} = 15$ (left) and the LUBR results at $\mathtt{M} = 4$ (right). Data are normalized by the peak of the perturbation velocity.

As we have shown, increasing the frequency has a stabilizing effect on the boundary-layer flow. This is consistent with the DNS results by Whang and Zhong (2003), shown in figure 4.14 (left) and compared with our LUBR results in figure 4.14 (right). For sufficiently high frequency, the Klebanoff modes do not turn into Görtler vortices downstream. For the cases presented in figure 4.14 only steady perturbations are subject to centrifugal instability.

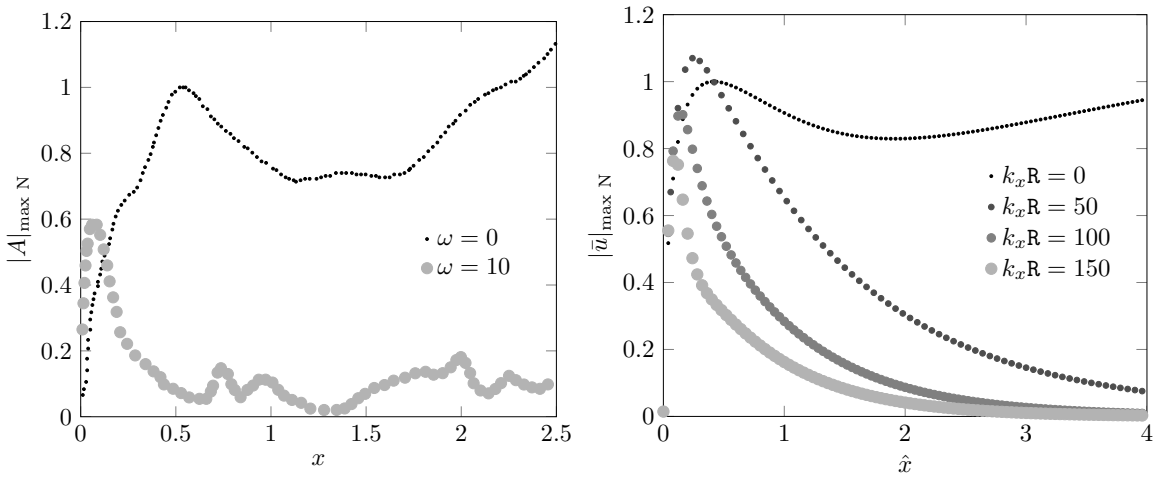

Fig. 4.14 Comparison of the influence of frequency relative to the DNS data of Whang and Zhong (2003) at $\mathtt{M} = 15$ (left) and the LUBR results at $\mathtt{M} = 4$ (right). Data are normalized by the peak value for the steady case.

4.1.7 Neutral stability curve

We now show the effect of the flow parameters on the neutral stability curves computed with the LUBR equations. This section focuses on incompressible flows and results can be found in (Viaro and Ricco, 2018).

Streamwise evolution of the perturbation energy

Figure 4.15 shows the streamwise evolution of the perturbation energy $\mathtt{E}(\hat{x})$ for both K-vortices and G-vortices in the case of a steady flow ($k_x\mathrm{R} = 0$) with $k_y = 2$. The maximum value of the energy $\mathtt{E}_{\max,\mathtt{G}_0} \equiv \max_{\hat{x}} |\mathtt{E}(\hat{x})|_{\mathtt{G}=0}$ for a flat plate scenario, $\mathtt{G} = 0$, is used to normalize the perturbation energy. The conditions for which the energy is maximum, $\mathtt{M}_1$ and $\mathtt{M}_2$, or minimum, $\mathtt{m}$, are associated with a stable flow for which $\varsigma = 0$. We can also identify three critical Görtler numbers, namely $\mathtt{G}_\mathrm{A}$, $\mathtt{G}_\mathrm{B}$, and $\mathtt{G}_\mathrm{C}$. For first one, $\mathtt{G} = \mathtt{G}_\mathrm{A} = 0$, the instability grows from the leading edge in the form of K-vortices as in figure 3.2, scenario $\boxed{1}$, until viscosity enters the play to dissipate it. The perturbation in the boundary layer is energized due to the centrifugal forces introduced by the curvature but Görtler vortices start to appear as boundary layer perturbations, after K-vortices have decayed, only at the second critical point $\mathtt{G} > \mathtt{G}_\mathrm{B} = 10.9$. The reference case of $\mathtt{G} = 12$, shown in figure 4.15, demonstrates that the

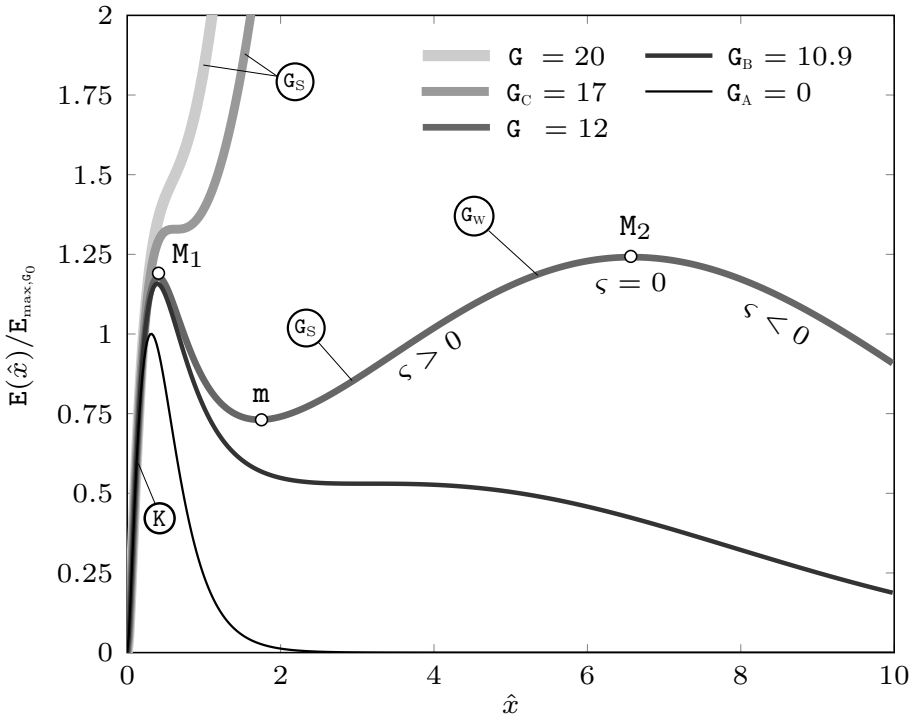

Fig. 4.15 Streamwise evolution of the perturbation energy $\mathtt{E}(\hat{x})$ for $k_y = 2$, $k_x\mathtt{R} = 0$, and $\mathtt{M} = 0$. $\mathtt{E}_{\mathrm{max},\mathtt{G}_0}$ identifies the maximum value of $\mathtt{E}$ for $\mathtt{G} = 0$.

perturbation initially grows as K-vortices until the stable point $\mathtt{M}_1$ is reached. Then, viscosity causes the instability to decay up to the location m where Görtler vortices appear as a second perturbation. Before reaching the second stability point identified by $\mathtt{M}_2$, Görtler vortices undergo their shift from strong growth (G$_\mathrm{s}$) to weak growth (G$_\mathrm{w}$) at the location $\hat{x} = \hat{x}_\mathtt{G}$. As curvature further increases, the third critical Görtler number $\mathtt{G} = \mathtt{G}_\mathrm{C} = 17$ marks the condition above which there is no viscous decay anymore, and the G-vortices grow directly from the K-vortices, as shown in figure 4.15 for $\mathtt{G} > \mathtt{G}_\mathrm{C}$. This last case is also represented in figure 3.2, scenario 2. In summary, whenever the Görtler number is within the two critical values $\mathtt{G}_\mathrm{B} < \mathtt{G} < \mathtt{G}_\mathrm{C}$ the boundary layer experiences two separate kinds of instability.

Regions of the neutral curves

An example of a typical neutral curve for $k_x\mathtt{R} = 0$ and $k_y = 2$ is shown in figure 4.16 in which the neutral curve is represented by the continuous black line. K-vortices turn directly into Görtler vortices at the streamwise location $\hat{x}_\mathtt{K}$ identified by the black dotted line whereas the

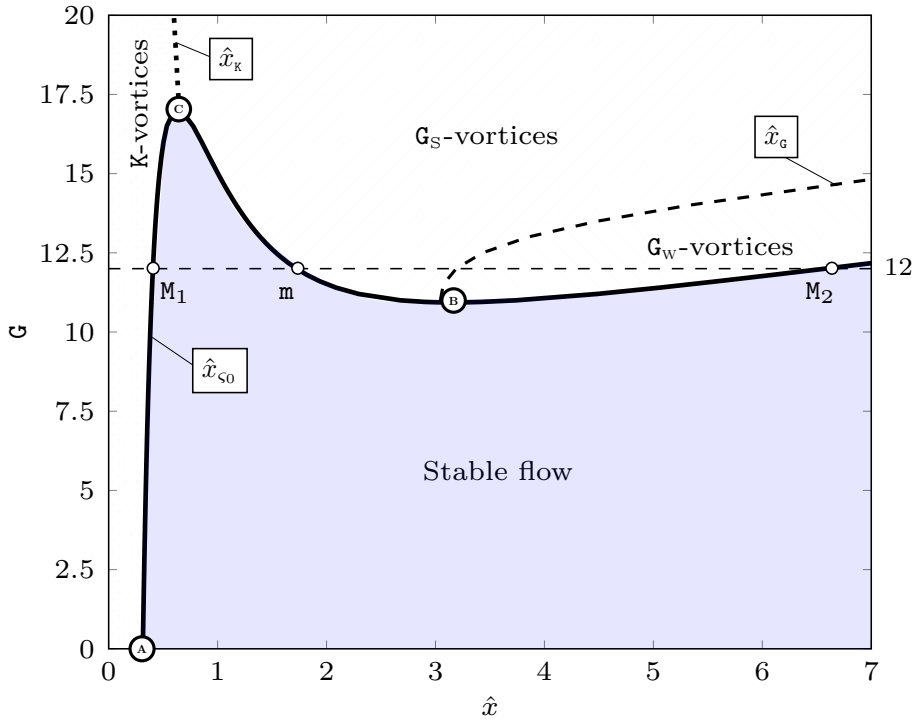

Fig. 4.16 Neutral stability curve, $\hat{x} = \hat{x}_{S_0}$ (▬), curve where K-vortices shift to G_s-vortices, $\hat{x} = \hat{x}_K$ (▪▪▪), and curve where G_s-vortices shift to G_w-vortices, $\hat{x} = \hat{x}_G$ (- - -), for $k_x R = 0$, $k_y = 2$.

strong growth of the Görtler vortices weakens at the streamwise location $\hat{x}_G$ identified by the black dashed line. Figure 4.16 also shows that the critical Görtler numbers previously introduced are related to the critical points A, B, and C, in the neutral curve. For a flat plate, K-vortices become stable after the streamwise location associated with point A. The neutral curve experiences a local minimum at a certain streamwise location $\hat{x}$ for $G_B = 10.9$, point B, representative of the Görtler number below which K-vortices are the only source of instability. Finally, point C represents the streamwise location where the neutral curve has a local maximum which corresponds to the Görtler number G_C above which Görtler vortices grow directly from K-vortices.

As the Görtler number increases the unstable region of the neutral curve expands rapidly due to the inviscid instability gaining strength from the curvature effects. Increasing the Görtler number also causes the minimum and maximum of the perturbation energy, m and M_1 respectively, to eventually combine for $G = G_c$, also represented in figure 4.15. By further

increasing the Görtler number, the boundary layer experiences a direct shift of instability from the K-vortices, always present near the leading edge, to the Görtler vortices at the location $\hat{x} = \hat{x}_{\mathrm{K}}$. It is important to point out that for the definition of ς the perturbation energy could have been computed with the integral of $|\bar{u}|$ defined over y. This would have caused a moderate shift of the neutral curves towards lower values of G but maintaining a similar shape.

The asymptotic analysis performed in §3.4 valid for $\mathrm{G} \gg 1$ demonstrates that the exponential growth of the perturbation is preceded by the existence of two pre-modal stages. In the first stage, $\hat{x}_{\mathrm{I}} = O\left(\mathrm{G}^{-2/3}\right)$, pressure is influenced by the effects of curvature but it is still not coupled to the velocity field. The second stage, $\hat{x}_{\mathrm{II}} = O\left(\mathrm{G}^{-2/5}\right)$, is characterized by the convection terms becoming comparable with the pressure perturbation gradient along the wall-normal direction. Here, the Görtler instability begins. These two stages are identified through the red lines in figure 4.17 which represents figure 4.16 for high values of the Görtler number near the leading edge. The validity of the parameter β to establish the shift between the two types of instabilities is confirmed by the fact that, as the Görtler number increases, $\hat{x}_{\mathrm{I}} < \hat{x}_{\mathrm{K}} < \hat{x}_{\mathrm{II}}$. Therefore, the approach we used agrees well with the asymptotic analysis at large Görtler numbers and we find that $\hat{x}_{\mathrm{K}} = O\left(\mathrm{G}^{-0.52}\right)$ for $10^4 < \mathrm{G} < 10^6$.

We conclude the analysis of the neutral curve regions by demonstrating that there is the possibility to experimentally verify the existence of the three critical points previously mentioned using the parameters of Boiko et al. (2010b) as a reference. In their experiments, Görtler instability was triggered by free-stream disturbances in the case of a unit Reynolds number $\mathrm{R}^*_{\mathrm{U}} = U^*_\infty/\nu^* = 6 \cdot 10^5$ m^{-1}, radius of curvature $r^* = 8.37$ m, and spanwise wavelengths $\lambda^*_z = 0.008, 0.012, 0.024$. All of their unstable points are within the region where the Görtler instability experiences a strong growth, as shown in figure 4.17. Table 4.4 proves that if the radius of curvature is properly adjusted, the location of the critical points would be acceptable to be measured experimentally.

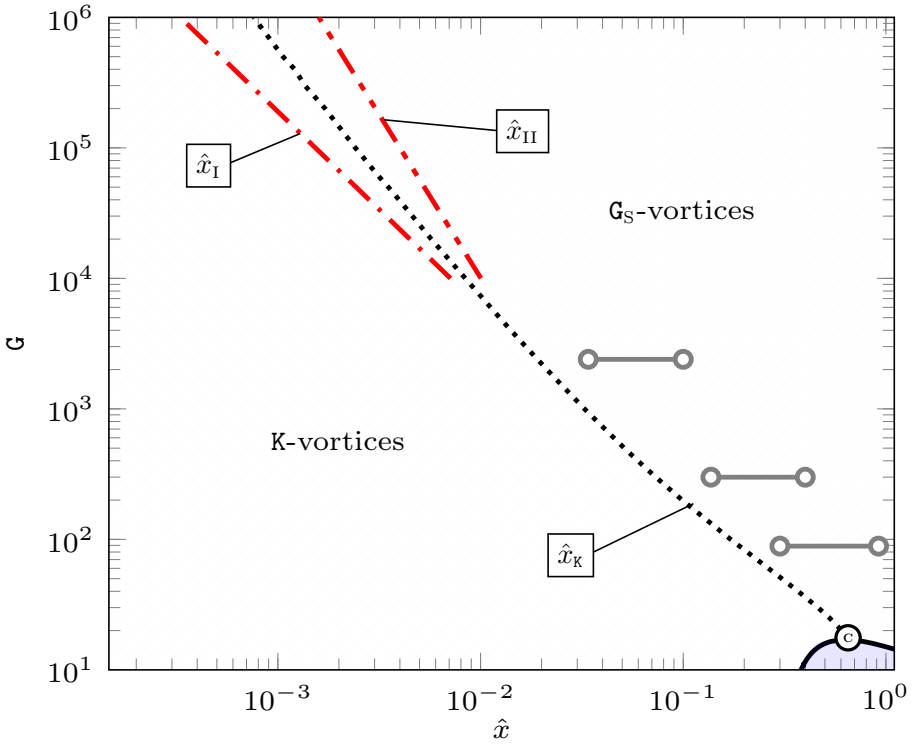

Fig. 4.17 Detail at large G numbers showing the experimental values of Boiko et al. (2010b) (○——○) and the asymptotic limits for $\mathrm{G} \gg 1$ of Wu et al. (2011), $\hat{x}_{\mathrm{I}} = O\left(\mathrm{G}^{-2/3}\right)$ (– · –) and $\hat{x}_{\mathrm{II}} = O\left(\mathrm{G}^{-2/5}\right)$ (– · · –).

Effect of frequency

The effect of frequency, introduced by the parameter $k_x\mathrm{R} = \mathrm{R}\lambda_z^*/\lambda_x^*$, on the neutral stability curves is shown in figure 4.18 for incompressible flows. The lines of $\hat{x}_{\mathrm{K}}$ have been omitted as they overlap for the majority of Görtler numbers. Sufficiently downstream from the leading edge, the neutral curves are independent on the parameter k_y, representative of the influence of the initial conditions directly associated to the oncoming disturbances of the free stream, and therefore only the case $k_y = 1$ is shown.

Since a significant increase of stability is caused by the increase of frequency, as demonstrated by figure 4.18, steady disturbances of the free stream are representative of the most unstable conditions. For the frequency parameter of $k_x\mathrm{R} = 6$, and following the evolution of the instability for $\mathrm{G} = 55$, it can be noticed that, after the decay of Görtler vortices, the boundary layer goes through a second region of instability followed by the final region of

λ_z^*	x_A^*	r_A^*	x_B^*	r_B^*	x_C^*	r_C^*
0.002	0.02	∞	0.04	0.68	0.19	1.06
0.004	0.08	∞	0.15	5.46	0.78	8.51
0.008	0.31	∞	0.61	43.68	3.01	68.06

Table 4.4 Estimation of the physical location (in meters) of three critical points in the case of $k_y = 2$ and $k_x\mathtt{R} = 0$ from the values found in Boiko et al. (2010b).

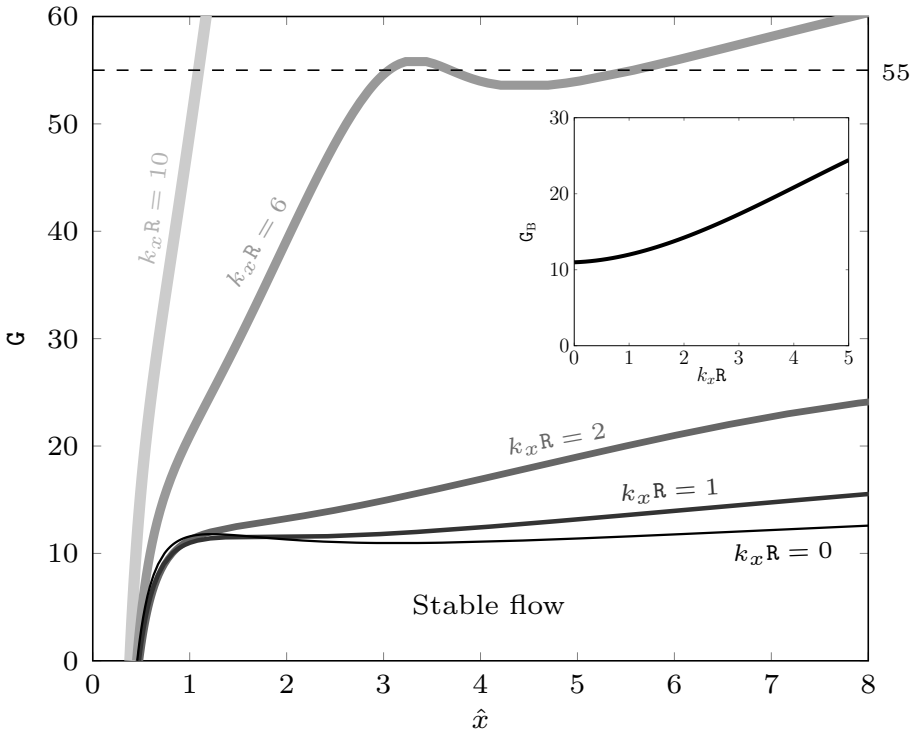

Fig. 4.18 The effect of the frequency parameter $k_x\mathtt{R}$ on the neutral stability curves $\varsigma = 0$ in the case of $\mathtt{M} = 0$ and $k_y = 1$. Inset: effect of $k_x\mathtt{R}$ on the critical Görtler number $\mathtt{G_B}$ in the case of $\mathtt{M} = 0$ and $k_y = 1$.

stability. This phenomenon, represented in figure 4.18, is characteristic of a range of Görtler numbers whenever $k_x\mathtt{R} > 2$ and becomes more prominent as frequency increases. However, as the LUBR equations are valid for $k_x \ll 1$, our focus is limited to disturbances with low frequencies, which are also the most critical cases.

The increase of the frequency parameter $k_x\mathtt{R}$ also causes the critical Görtler number $\mathtt{G_B}$ to increase, as shown in the inset of figure 4.18. Due to the fact that $\mathtt{G_B}$ is close to the streamwise location where the neutral curves become independent on the parameter k_y, the results in the

inset for different k_y would lie on the same curve and, therefore, only the case of $k_y = 1$ is shown.

When the flow is not steady, Goldstein (1983) demonstrated for a flat plate geometry that the leading-edge receptivity could cause the excitation of TS waves, which was also shown by Ricco and Wu (2007). As the streamwise location of the TS-waves neutral point increases with a decrease of frequency, we here analyze only the worst case scenario of $k_x\mathtt{R} = 10$, our highest frequency. An in-house code for spatial stability analysis (Ricco, 2009) was here used to investigate the streamwise location $\hat{x}$ where TS waves would start to grow over a flat plate with parameters taken from the experiments of Boiko et al. (2010b). Since we are interested in spatial stability cases, the Squire transformation (Squire, 1933) can be employed for the neutral conditions. We demonstrate that the three-dimensional TS waves remain stable unless $2\pi\delta^*/\lambda_z^* < 0.08$ approximately, with δ^* being displacement thickness. This value is associated to spanwise wavelengths larger than 0.4m, which are not physically relevant. The spanwise wavenumber typical of our conditions gives a value of $2\pi\delta^*/\lambda_z^* \approx 2.5$, and therefore we are in the range of stable TS waves. The possibility of TS waves appearing at smaller streamwise locations of the neutral curves could arise if we were to increase the frequency parameter $k_x\mathtt{R}$. However, this would cause the low-frequency assumption of our theoretical framework to become invalid. This limitation can be overcome through the use of a different asymptotic theory, e.g. the triple-deck. Alternatively, the complete linearized Navier-Stokes and continuity equations, which include the streamwise viscous effects and streamwise pressure gradient needed to capture the TS waves instability, should be adopted. This was done by Boiko et al. (2010b) but the receptivity to oncoming free-stream disturbances was not taken into account and this limits the accuracy of the analysis as shown by Wu et al. (2011) for incompressible flows and confirmed here by compressible flows.

Effect of the free-stream wavelength ratio

The influence of the parameter k_y, the wall-normal wavenumber directly linked to the initial conditions and, hence, the oncoming free stream, is shown in figure 4.19 for the steady, incompressible cases of $k_x\mathtt{R} = 0$, $\mathtt{M} = 0$. Based on our scaling, k_y also represents the ratio of

the spanwise wavelength λ_z^* over the wall-normal wavelength λ_y^*. From the most unstable case of $k_y = 0$, the stability region increases in a limited region sufficiently close to the leading edge as k_y increases, for different values of $k_x\mathtt{R} = 0$. The initial condition k_y do not affect the neutral curve after $\hat{x} = \hat{x}_s$. This streamwise location is here defined by the neutral points being confined within $\Delta\hat{x} < 0.0005$ as k_y changes. Hall (1990) also shows the independence of the neutral curves from the initial conditions for $\hat{x}$ high enough.

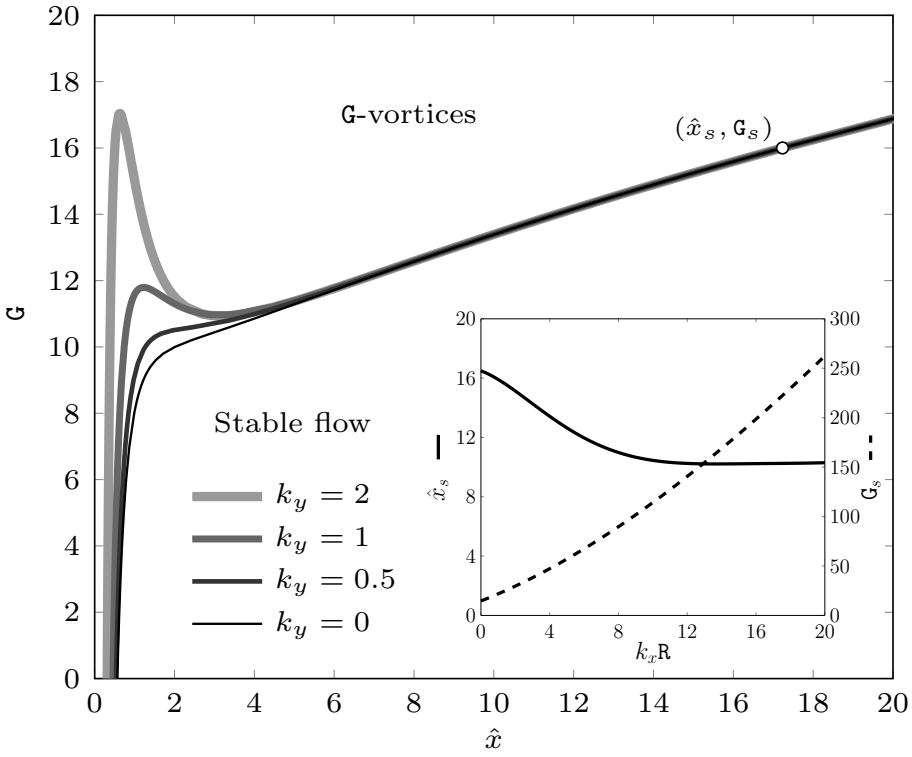

Fig. 4.19 The effect of the wall-normal wavenumber k_y on the neutral stability curves $\varsigma = 0$ for $\mathtt{M} = 0$ and $k_x\mathtt{R} = 0$. Inset: the effect of the frequency parameter $k_x\mathtt{R}$ on the streamwise location $\hat{x}_s$ and the corresponding Görtler number $\mathtt{G}_s$.

The inset of figure 4.19 shows that when $k_x\mathtt{R}$ increases the streamwise location $\hat{x}_s$ also increases, with the dependence on frequency becoming negligible for $k_x\mathtt{R} > 10$. In addition, the increase of $k_x\mathtt{R}$ also causes a monotonical increase of the Görtler number $\mathtt{G}_s$ related to $\hat{x}_s$. In terms of dimensional values, if we consider the parameters of the experiments performed by Boiko et al. (2010b), the location $\hat{x}_s = 10$ would be equivalent to $x^* \approx 22$m. As a result,

the neutral curves become independent on the initial conditions k_y at streamwise locations from the leading edge that are not relevant for real case scenarios.

This analysis on the influence of the initial conditions additionally confirms that the dynamics of the Görtler flow can only be correctly described by a receptivity framework that includes the influence of the free-stream characteristics.

Effect of Mach number

Figure 4.20 (left) shows the stabilizing effect of the Mach number on the neutral stability curves for the steady case of $k_x\mathtt{R} = 0$. The region of stability becomes bigger as the Mach increases. This is in agreement with previous studies on compressible neutral stability curves (El-Hady and Verma, 1983). Even in the case of a flat plate, the region of stability increases, but in all scenarios the Klebanoff modes remain the initial instability of the boundary layer. Figure 4.20 (left) also shows how the effect of the Mach number is stronger in supersonic conditions. Both critical Görtler numbers increase with the Mach number, as shown in figure 4.20, with $\mathtt{G}_\mathrm{C}$ being the one most affected.

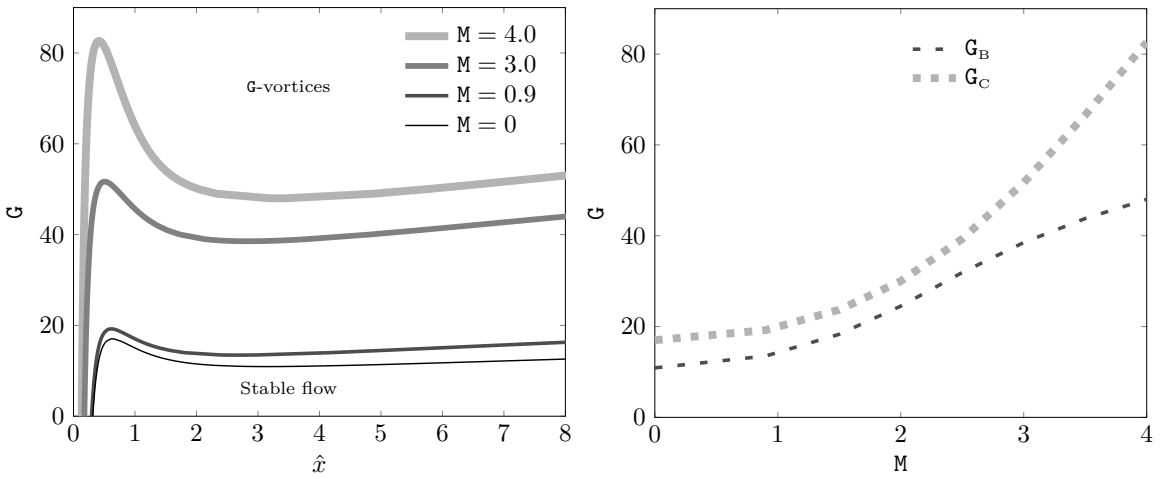

Fig. 4.20 Neutral stability curves, $\hat{x} = \hat{x}_{\varsigma_0}$ at different values of the Mach number for $k_x\mathtt{R} = 0$, $k_y = 2$ (left) and the influence of the Mach number on the critical Görtler numbers (right).

Comparison with previous theories and experiments

The neutral curves computed with the LUBR solution here presented are compared with experiments and previous theories at $k_x\mathtt{R} = 0$ and $k_y = 1$ for $\mathtt{M} = 0$ in figure 4.21 and $\mathtt{M} = 3$ in figure 4.22. Results are compared with previous theoretical frameworks plotted in dotted lines, and experimental results potted with marks. It is important to note that this comparison is qualitative, as the neutral curves were computed with different parameters. The dotted lines represent the location $\hat{x} = \hat{x}_{\mathtt{K}}$ where K-vortices shift into G-vortices.

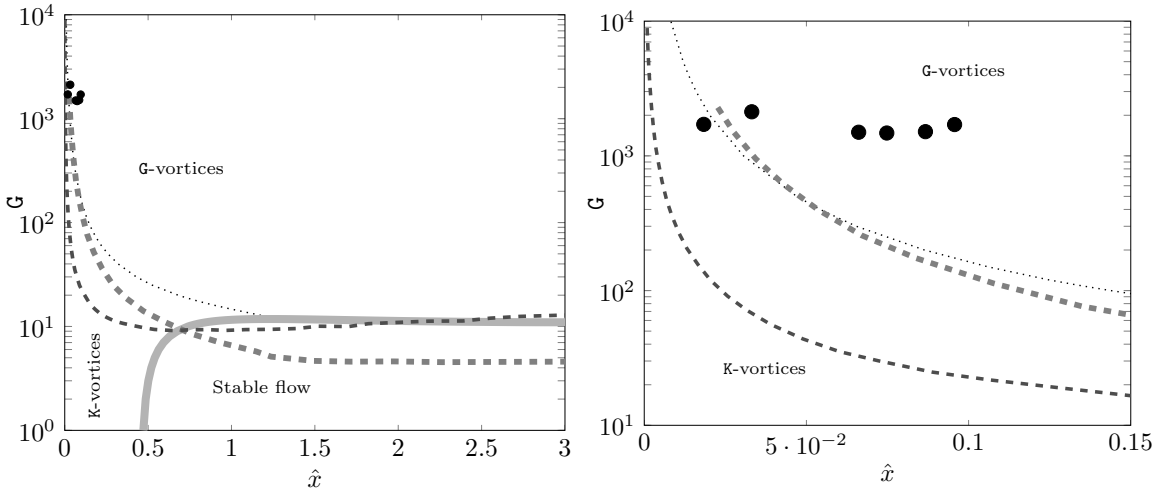

Fig. 4.21 Comparison of the LUBR neutral curve (—) at $k_x\mathtt{R} = 0$, $k_y = 1$ with previous theories (dashed) and experiments (marks) for $\mathtt{M} = 0$ (left) and its detail near the leading edge (right). Theories of Hall (1990) (- - -) and El-Hady and Verma (1983) (- - -), experiments Tani (1962) (●). Curves at which the K-vortices turn into G-vortices, $\hat{x} = \hat{x}_{\mathtt{K}}$ (·····).

Early attempts to compute neutral curves for Görtler flows for incompressible and compressible flows involved the use of an eigenvalue framework such as the one introduced by El-Hady and Verma (1983), in which the boundary-layer growth effect are included. Hall and Malik (1989) later derived similar equations, and, therefore, similar neutral curves, commenting that the limit of small wavenumbers, i.e., $\hat{x} \ll 1$ in our scaling, might be outside of the region where the equations were valid. This is confirmed by figure 4.21 and figure 4.22 in which the neutral curves computed from the EV framework of El-Hady and Verma (1983) are not capturing the unstable region near the leading edge where Klebanoff modes exist. The receptivity framework for incompressible flows proposed by Hall (1990) omits one of

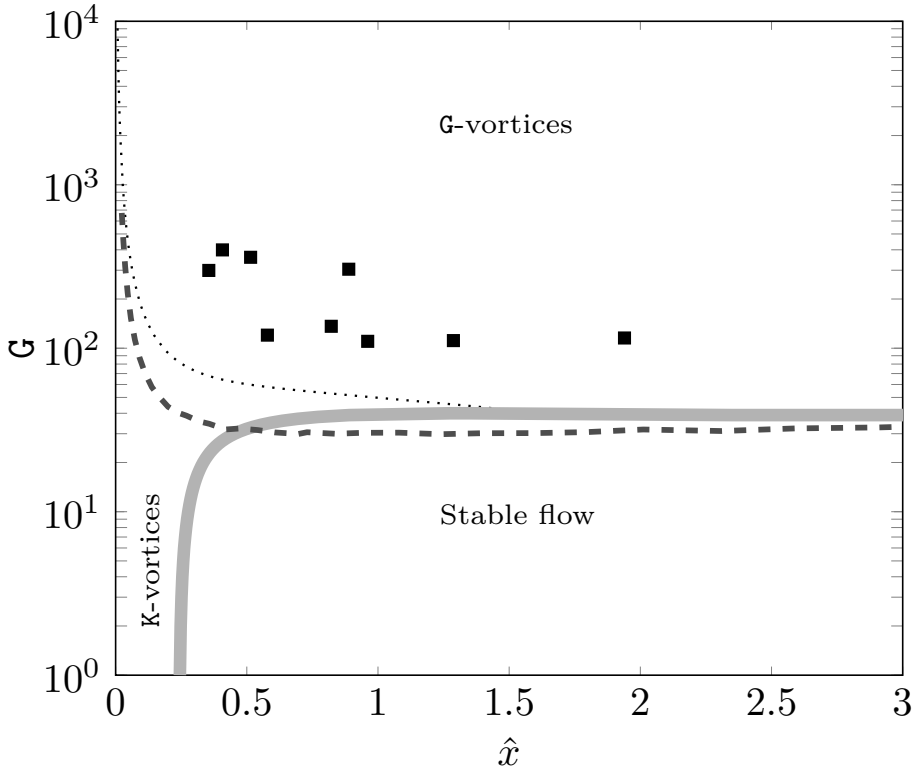

Fig. 4.22 Comparison of the LUBR neutral curve (▬) at $k_x\mathtt{R} = 0$, $k_y = 1$ with the previous theories of El-Hady and Verma (1983) (- - -) and experiments of Ciolkosz and Spina (2006) (■). Curves at which the K-vortices turn into G-vortices, $\hat{x} = \hat{x}_\mathtt{K}$ (·····).

the experimental points found in Tani (1962), as shown in figure 4.21 (right). This receptivity framework is an improvement of the work of Hall (1983) in which the initial conditions of the system of partial differential equation were imposed inside the boundary layer instead of taking into consideration the oncoming flow as in a receptivity study. However, it can be seen that not even the neutral curves of Hall (1990) can solve for the region of the Klebanoff modes. The neutral curves proposed with our LUBR solution demonstrate that the last point of the experiment of Tani (1962) is in the region of Klebanoff instabilities, very close to the leading edge.

For the supersonic case at $\mathtt{M} = 3$, the EV framework of El-Hady and Verma (1983) also fails to correctly reproduce the neutral curves for $\hat{x} \ll 1$. However, the agreement with the LUBR solution is stronger as $\hat{x}$ increases, as shown in figure 4.22. In this limit of high wavenumbers ($\hat{x} \gg 1$), the neutral curves also match the asymptotic results of Hall and Malik

(1989) (not shown). Our LUBR results also confirm the experiments at supersonic conditions of Ciolkosz and Spina (2006) in which they state that these points are representative of Görtler vortices. In the same paper, they also performed experiments at the same locations but in a flat plate scenario where no vortices were found. This is also in agreement with our neutral curve as the experimental points would lie in the sable region for $\mathtt{G} = 0$.

4.2 Eigenvalue results

We now compare the LUBR solution with the solutions of the parallel and non-parallel EV equations.

4.2.1 Growth rate and streamwise length scale of the boundary-layer perturbation

Figure 4.23 shows the comparison between the growth rate (left) and the streamwise length scale ratio (right) of the LUBR solution and EV solution. The most important point is that the receptivity process selects the most unstable modes, which, in the limit $\mathtt{G} \gg 1$, correspond to the first eigenvalues of table 3.1. The non-parallel EV solution (solid circles) is a better approximation for the growth rate and the streamwise length scale than the parallel EV solution (empty circles) at $\eta = 2$, where the growth rate is at its maximum. The non-parallel and parallel EV formulations show the strongest disagreement with the receptivity LUBR solution closer to the leading edge, where the solution has not yet acquired a modal form. In this region, the non-parallel effects, and the initial and free-stream boundary conditions thus play a key role in the dynamics of the perturbation. In the limit $\hat{x} \to 0$ the EV solution is invalid, with the growth rate becoming negative. Results show a tendency of the EV approach to overestimate the growth rate, which is in agreement with the results of Spall and Malik (1989). The agreement between the LUBR solution and the parallel EV solution is worse in the supersonic case than in the subsonic case. The use of the rigorous receptivity LUBR framework becomes therefore essential for supersonic flows.

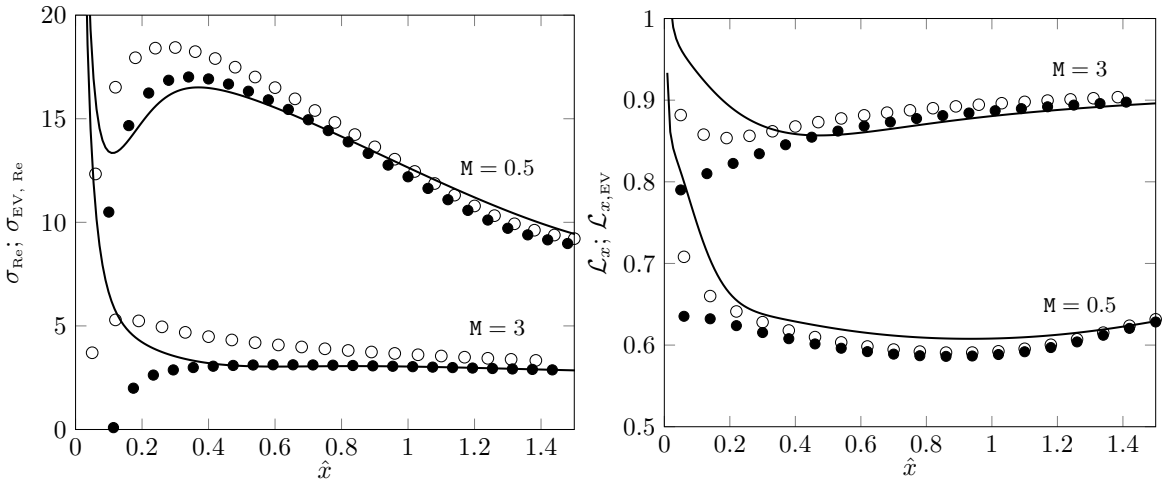

Fig. 4.23 Comparison between the LUBR $\sigma_{\mathrm{Re}}(\hat{x},\eta)$ (—) at $\eta = 2$, the non-parallel EV $\sigma_{\mathrm{EV,\,Re}}(\hat{x})$ (•), and the parallel EV $\sigma_{\mathrm{EV,\,Re}}(\hat{x})$ (○) (left) and comparison between the LUBR $\mathscr{L}_x(\hat{x},\eta)$ (—) at $\eta = 2$, the non-parallel EV $\mathscr{L}_{x,\mathrm{EV}}(\hat{x})$ (•), and the parallel EV $\mathscr{L}_{x,\mathrm{EV}}(\hat{x})$ (○) (right), for $\mathtt{M} = 3$, $\mathtt{G} = 1247.3$, $k_y = 1$, $\mathtt{F} = 1.32 \cdot 10^{-7}$ and $\mathtt{M} = 3$, $\mathtt{G} = 239.7$, $k_y = 1$, $\mathtt{F} = 7.5 \cdot 10^{-7}$.

4.2.2 Velocity and temperature profiles

The velocity and temperature EV profiles are compared with the LUBR profiles in figure 4.24 for $\mathtt{M} = 3$. Since the eigenfunctions are obtained to within an arbitrary undefined constant, the solutions are normalized by the maximum values at each streamwise location to be compared with the LUBR solutions. The non-parallel EV solution approximates the profiles well, especially as $\hat{x}$ increases. Under the parallel flow approximation, the maximum of the perturbations is slightly shifted upwards and the solution is overestimated in the region above the maximum, especially near the leading edge, where the non-parallel effects are most significant. As the wall is approached both the parallel and the non-parallel EV solutions agree well with the LUBR solution.

The crossflow profiles shown in figure 4.25 highlight the limit of the EV solution. Close to the leading edge there is a strong influence of the free-stream vortical disturbances which cannot be captured by the simplified EV framework. Therefore, a correct analysis of the flow in this region is only possible when the receptivity of the base flow to the external vortical disturbances is considered. The disagreement in the free stream is expected, but the solutions do not even match near the wall. The non-parallel EV solution begins to approximate the

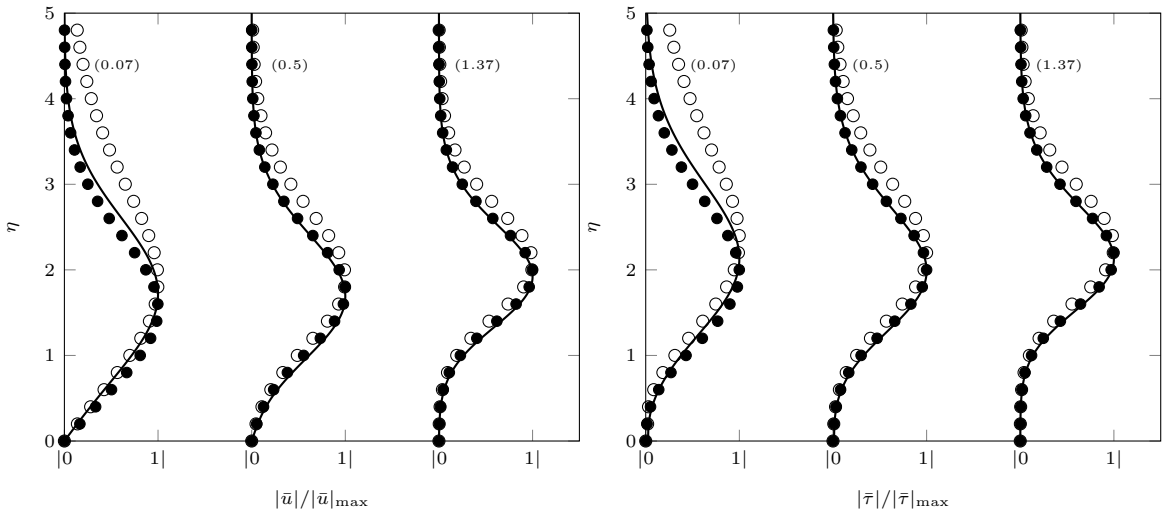

Fig. 4.24 Comparison between the LUBR solution (—), the non-parallel EV solution (•), and the parallel EV solution (○) for the streamwise velocity profiles (left) and temperature profiles (right) at $\mathtt{M} = 3$, $\mathtt{F} = 7.5 \cdot 10^{-7}$, $\mathtt{G} = 239.73$, $k_y = 1$. Numbers in the parenthesis correspond to the streamwise location $\hat{x}$.

crossflow perturbations well only for sufficiently high $\hat{x}$. We previously demonstrated how the growth rate is not only a function of $\hat{x}$, as shown by the decomposition (3.26), but it does also change with η even for large streamwise locations. Similarly, figures 4.24 and 4.25 demonstrate that the eigensolutions are not a simple function of η but do depend on the streamwise location $\hat{x}$.

4.2.3 Receptivity coefficient

Since we employ a receptivity framework, we here define a receptivity coefficient $\mathtt{A}$ that links the perturbation in the boundary layer with the oncoming free-stream disturbances. We start by introducing the eigenvalue solution (EV) in a form similar to (3.26)

$$\bar{u}_e(\hat{x},\eta) = \widetilde{u}_e(\eta)\, e^{\int_{\hat{x}_\mathrm{M}}^{\hat{x}} \sigma_{\mathrm{EV,\,Re}}(x)\mathrm{d}x}, \tag{4.5}$$

where $\sigma_{\mathrm{EV}}(\hat{x})$ is a complex number with its real part $\sigma_{\mathrm{EV,\,Re}}(\hat{x}) \equiv \Re\{\sigma_{\mathrm{EV}}(\hat{x})\}$ representative of the local growth rate. The streamwise location $\hat{x}_\mathrm{M}$ represents the point where the solution is in the modal form. The eigenfunction $\widetilde{u}_e$ is then normalized by its maximum value along η,

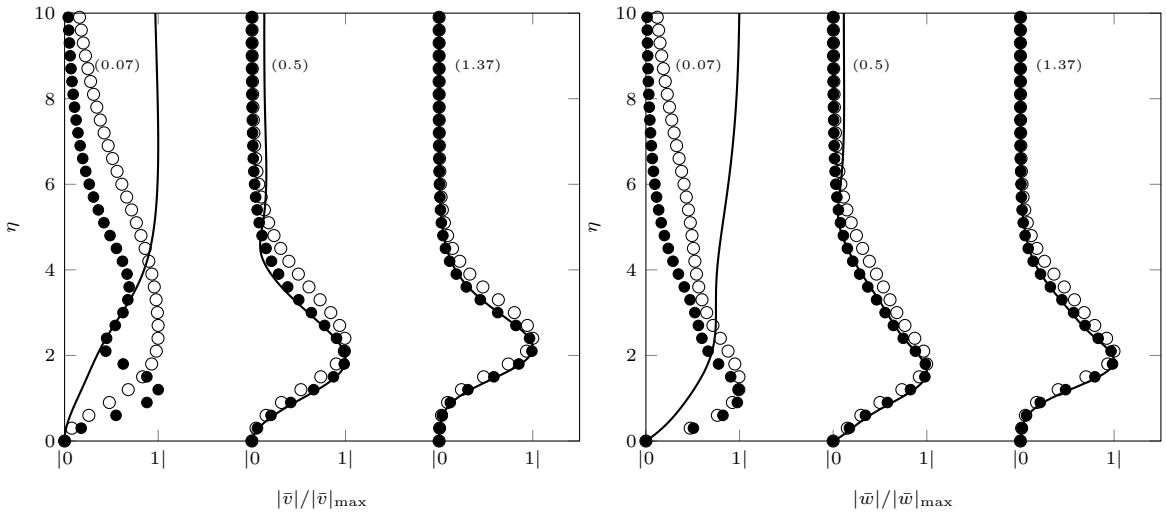

Fig. 4.25 Comparison between the LUBR solution (—), the non-parallel EV solution (●), and the parallel EV solution (○) for the wall-normal velocity profiles (left) and spanwise velocity profiles (right) at $\mathtt{M} = 3$, $\mathtt{F} = 7.5 \cdot 10^{-7}$, $\mathtt{G} = 239.73$, $k_y = 1$. Numbers in the parenthesis correspond to the streamwise location $\hat{x}$.

and applying the absolute value we find that

$$|\bar{u}_e(\hat{x},\eta)| = \mathtt{A}\,\frac{|\widetilde{u}_e(\eta)|}{|\widetilde{u}_e(\eta)|_{\max}}\, e^{\int_{\hat{x}_\mathrm{M}}^{\hat{x}} \sigma_{\mathrm{EV,\,Re}}(x)\mathrm{d}x}, \tag{4.6}$$

where $\mathtt{A}$ remains undetermined due to the fact that the eigenfunction is computed to within an undefined constant. We can further simplify (4.6) by considering only the maximum value along η, which gives

$$|\bar{u}_e(\hat{x})|_{\max} = \mathtt{A}\, e^{\int_{\hat{x}_\mathrm{M}}^{\hat{x}} \sigma_{\mathrm{EV,\,Re}}(x)\mathrm{d}x}. \tag{4.7}$$

Next, the amplitude of the streamwise velocity $\bar{u}(\hat{x},\eta)$ from the LUBR solution can be similarly expressed as

$$|\bar{u}(\hat{x})|_{\max} = \mathtt{A}(\hat{x})\, e^{\int_{\hat{x}_\mathrm{M}}^{\hat{x}} \sigma_{\mathrm{EV,\,Re}}(x)\mathrm{d}x}, \tag{4.8}$$

from which $\mathtt{A}(\hat{x})$, the streamwise-dependent receptivity coefficient, is implicitly defined. The maximum amplitude of the streamwise velocity perturbation of the LUBR solution can then be obtained given the EV solution and $\mathtt{A}(\hat{x})$, as shown by (4.8). This allows us to investigate how the perturbation inside the boundary layer is influenced by the oncoming free-stream disturbances as the parameters $k_x\mathtt{R}$, k_y and $\mathtt{G}$ are modified. It is important to

stress that the receptivity coefficient $\mathtt{A} = \mathtt{A}(\hat{x})$ would be constant only if the growth rate of the EV solution could entirely predict the changes in the streamwise direction associated to the LUBR solution. In other terms, $\sigma_{\mathrm{EV,\,Re}}(\hat{x})$ should be equal to $|\bar{u}'(\hat{x})|_{\max}/|\bar{u}(\hat{x})|_{\max}$, i.e., the growth rate computed from the LUBR solution. However, this condition cannot become true as the influence of the oncoming free-stream flow are not taken into account by the EV solution.

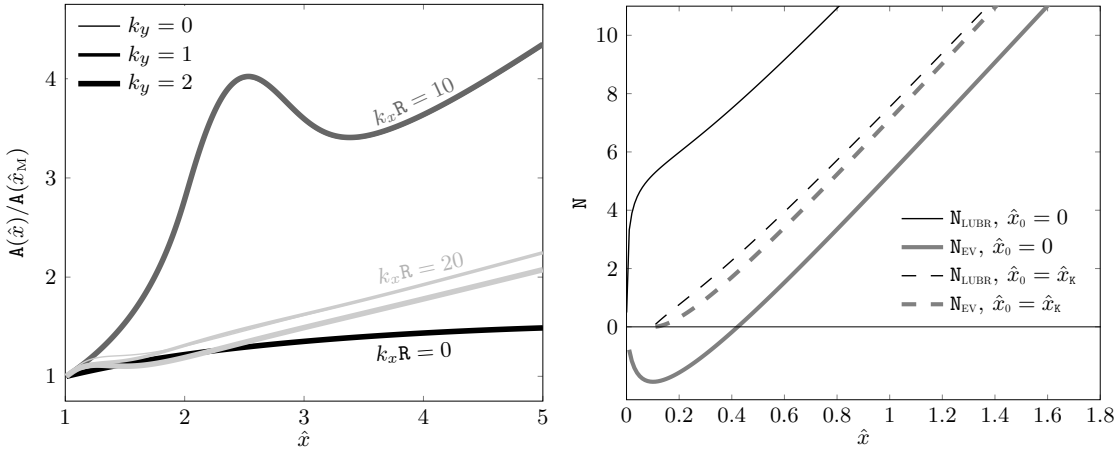

Fig. 4.26 Values of the normalized coefficient $\mathtt{A}(\hat{x})$ for different frequencies $k_x\mathtt{R}$ and k_y in the case of $\mathtt{G} = 300$ (left). Influence of the starting locations on the amplification factor $\mathtt{N}$ for the LUBR and EV approaches at $k_y = 1$, $k_x\mathtt{R} = 0$ and $\mathtt{G} = 300$ (right).

The influence of k_y and the frequency parameter $k_x\mathtt{R}$ on the normalized $\mathtt{A}(\hat{x})$ are shown in figure 4.26 (left) whereas table 4.5 defines the values $\mathtt{A}(\hat{x}_{\mathrm{M}})$ used to normalize the receptivity coefficient. The increase of frequency causes the perturbations inside the boundary layer to be more influenced by the oncoming free-stream flow. Only for $\hat{x}$ sufficiently large and $k_x\mathtt{R} = 0$ the receptivity coefficient becomes nearly constant. Boiko et al. (2017) also noted the strong influence of frequency on their receptivity coefficient based on optimal disturbances. Furthermore, we notice that the effect of the initial conditions k_y increases with the increase of frequency. In addition, the increase of $\mathtt{G}$ causes both the influence of k_y to decrease and the dependence of $\mathtt{A}(\hat{x})$ on $\hat{x}$ to be less strong. This means that $|\bar{u}(\hat{x})|_{\max}$ approaches a pure exponential evolution for a larger range of $\hat{x}$, which is in agreement to the exponential solution (4.5) being valid for $\mathtt{G} \gg 1$.

$k_x\mathtt{R}$	$k_y = 0$	$k_y = 1$	$k_y = 2$
0	66.60	60.56	47.48
10	13.51	15.40	14.06
20	0.31	0.44	0.54

Table 4.5 Receptivity coefficient $\mathtt{A}(\hat{x}_{\mathrm{M}})$ for $\mathtt{G} = 300$.

This analysis, performed for incompressible flows, can also be easily extended to include compressibility effects.

4.2.4 N-factor

The amplification factor, alternatively labeled N-factor, has been thoroughly used in engineering applications for the prediction of transition (Jaffe et al., 1970; Van Ingen, 1956). From our receptivity analysis, we here comment the effect of the disturbances in the free stream on this parameter, defined as

$$\mathtt{N}(\hat{x}) \equiv \int_{\hat{x}_0}^{\hat{x}} \sigma(x)\mathrm{d}x, \tag{4.9}$$

where σ indicates the growth rate calculated from the LUBR solution or the EV solution and is associated to $\mathtt{N}_{\mathrm{LUBR}}$ or $\mathtt{N}_{\mathrm{EV}}$, respectively. Engineers are used to associate the streamwise location of transition to the value of $\mathtt{N} = 9$, but this is an ambiguous estimation as demonstrated by figure 4.26 (right) since the receptivity coefficient strongly depends on the initial location where it is computed. In addition, when $\hat{x}$ is held fixed, the N-factor computed from the LUBR solution is much larger than the N-factor computed with the EV solution. This disagreement accentuates if we start the computation of the N-factor from $\hat{x} = \hat{x}_0 = 0$, which is caused by the EV approach being unable to solve the strong initial growth of the K-vortices near the leading edge. On the other hand, when the computation of the N-factor begins at $\hat{x} = \hat{x}_0 = \hat{x}_{\mathrm{K}}$, i.e., where the amplification of Görtler vortices starts, the agreement between the LUBR and EV solutions improves. An improvement is also noticed when $\hat{x}_0$ lies in the modal-growth region. Nonetheless, we point out that $\hat{x}_0$ is still defined arbitrarily and, therefore, whenever the N-factor is used to predict transition a careful verification on the conditions related to its calculation must be performed. Even with the rigorous theoretical framework here introduced

for Görtler flows the N-factor approach remains unreliable for the prediction of transition, even though transition is not a direct consequence of Görtler vortices. Problems related with the amplification factor approach have also been noted in the past by Smith (1955), Malik et al. (1999) and Boiko et al. (2017).

4.3 Asymptotic results

The asymptotic exponents $\breve{\sigma}(\breve{x})$ in (3.75) denote the earliest growth of the Görtler vortices triggered by the external free-stream disturbances. As the instability evolves, they turn into the fully developed local eigenmodes $\sigma_{\text{EV}}(\hat{x})$ of (3.26). From (3.95) the streamwise velocity of the stage III solution multiplied by $\mathtt{G}^{-1/2}$ can be compared with the LUBR streamwise velocity $\bar{u}$. Figure 4.27 shows that the growth rate and the streamwise velocity profiles computed from the LUBR equations, the latter normalized by their peak values, tend to the asymptotic solution as G increase. This is in accordance with the $\mathtt{G} \gg 1$ limit of the asymptotic analysis, although it occurs at very high Görtler and at high $\hat{x}$.

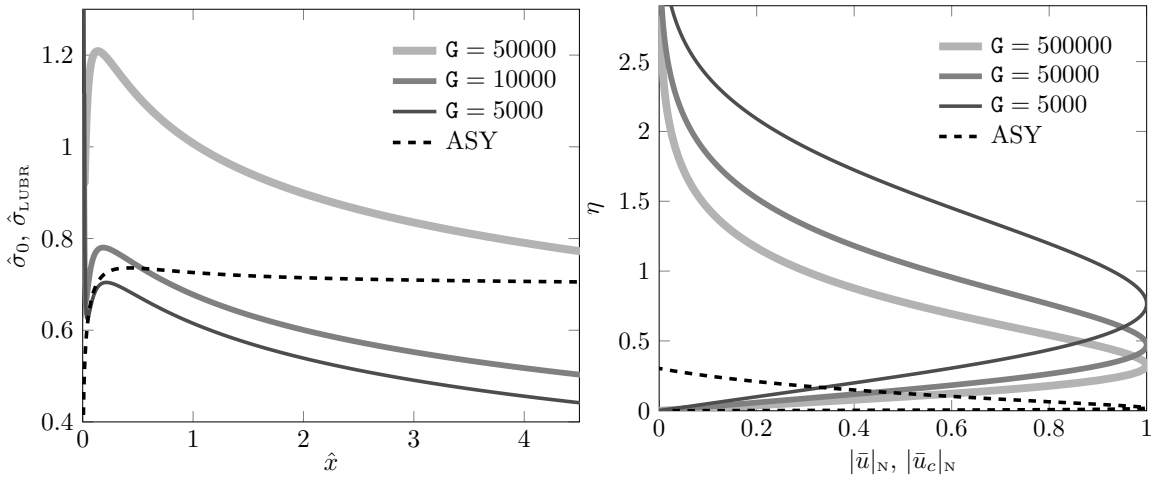

Fig. 4.27 Comparison between the composite solution $\bar{u}_c$ from the asymptotic stage III (- - -) and the LUBR results of the growth rates at $\eta = 2$ (left) and of the normalized streamwise velocity profiles at $\hat{x} = 1$ (right) for $\mathtt{G} = 5000$ (—), $\mathtt{G} = 10000$ (—), $\mathtt{G} = 50000$ (—), and $\mathtt{M} = 3$.

4.4 Triple-deck results

Following the theoretical analysis introduced in §3.5, the highly oblique TS-waves found in Ricco and Wu (2007) for the flat plate case, i.e. $\mathtt{G} = 0$, are here also reproduced and compared with cases for which $\mathtt{G} > 0$. Numerical results of the critical streamwise location $\bar{x}_c$ where the TS-waves start to grow are summarized in Table 4.6. These values are computed from the solution of the LUBR equations (3.9)-(3.13) and following the procedure of Ricco and Wu (2007). It can be noted that the effect of curvature on the solution only appears for $\kappa \geq 0.02$ and $\mathtt{G} \geq 2397.3$ approximately. This is consistent with the analytical results in §3.5 derived for $\kappa \ll 1$ and $\mathtt{G} = \mathscr{O}(1)$. Figure 4.28, graphically shows the results of Table 4.6 along with the triple-deck solution of (3.161).

G	*0*	*47.95*	*95.9*	*239.73*	*2397.3*	*23973*
κ						
0.0025	41.07	41.07	41.07	41.07	41.07	41.07
0.01	15.02	15.02	15.02	15.02	15.02	15.02
0.02	7.11	7.11	7.11	7.11	7.13	7.15
0.03	9.74	9.74	9.74	9.74	9.77	10.08

Table 4.6 Numerical values of the streamwise location $\bar{x}_c$ for different values of the Görtler number $\mathtt{G}$ and κ, for $\mathtt{M} = 3$.

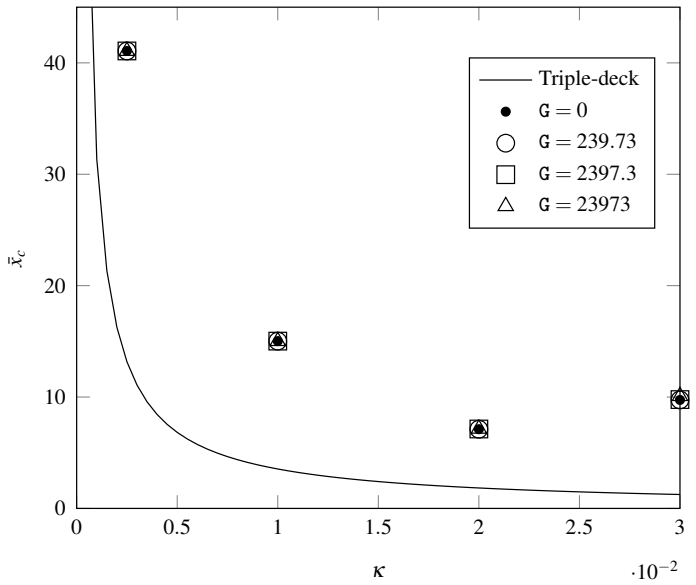

Fig. 4.28 Graphical representation of the streamwise location $\bar{x}_c$ as a function κ for different values of $\mathtt{G}$, for $\mathtt{M} = 3$.

Chapter 5

Conclusions

For the first time, we have investigated the complete evolution of compressible Görtler vortices over slightly streamwise-concave surfaces triggered by small-amplitude free-stream disturbances of the gust type. Although only kinematic perturbations exist in the free stream, the boundary layer is reigned by both velocity and temperature Görtler vortices that grow significantly downstream through the inviscid unbalance between centrifugal and pressure effects.

We have solved the boundary-region equations to investigate the receptivity of the base flow to free-stream vortical disturbances and we have also adopted two eigenvalue frameworks, based on the parallel and non-parallel flow assumptions, and a high-Görtler-number asymptotic formalism, which has been revelatory of the different stages of evolution of the Görtler instability from the leading edge. We have carried out a complete parametric study on the effects of frequency, ratio of free-stream wavelengths, Mach number, and Görtler number on the evolution of the Görtler vortices, focusing particularly on the growth rates, streamwise length scale, and position of the velocity and temperature perturbations. We have used the LUBR solution to solve the problem related to the neutral stability curves.

The crucial point is that both the initial conditions from the proximity of the leading edge and the outer free-stream boundary conditions are determined by the oncoming free-stream flow. This link is clearly elucidated in mathematical form in the milestone essay by Leib et al. (1999), from which the work by Ricco and Wu (2007) and Wu et al. (2011) take inspiration.

It is evident from the analysis that both conditions play a cardinal role in the development and growth of the Görtler vortices. Despite the fact that the eigenvalue approach accounts neither for the initial conditions, because it is a local approximation, nor for the free-stream forcing, because it is based on an homogeneous system, it does correctly determine the growth rate and streamwise length scale of the vortices sufficiently downstream from the leading edge. The receptivity boundary-region solutions thus match the eigenvalue solutions once the free-stream disturbance has decayed. However, it is only through the rigorous receptivity framework that the amplitude of the Görtler vortices can be uniquely computed and linked to the amplitude of the free-stream perturbation at each streamwise location. Furthermore and arguably most importantly, the eigenvalue formulation leads to completely incorrect results not only in the very proximity of the leading edge, but also at locations comparable with the streamwise wavelength of the free-stream flow. These streamwise stations may not be close to the leading edge and only the receptivity can inform us on where the agreement between the two solutions is of good quality. This proves that the inclusion of the correct initial and free-stream forcing is essential to compute the flow from the leading edge, especially in supersonic conditions. It also means that, even if an amplitude were assigned to the eigenvalue solution in order to use it for downstream computations and thus somehow bypass the modeling of the receptivity process from the leading edge, the shape of the velocity, temperature, and pressure profiles would be incorrect. It is unknown at this stage how this mismatch may affect the subsequent computation of the nonlinear stages and of the flow breakdown to turbulence. All these considerations are of course also true for the incompressible case studied by Wu et al. (2011) and for the hypersonic cases at very high Mach numbers, which falls outside the scope of the present work.

The asymptotic analysis based on the limit of high Görtler number is also recipient of the same comments devoted to the eigenvalue approach, but it is an extremely powerful tool for elucidating the physics of the Görtler instability, for example for distinguishing between the inviscid core and the wall-attached thin viscous region, which together lead to the construction of an accurate semi-analytical velocity profile. This and other physical properties could only be revealed through the asymptotic approach and not through the full

receptivity boundary-region approach. As we are driven towards both a thorough physical understanding of the flow and accurate flow computations, this trident approach has proved to be an invaluable, and arguably indispensable, tool for our receptivity study.

We of course look forward to high-quality experimental studies on compressible Görtler flows forced by free-stream vortical disturbances, for the primary intent to attain quantitative comparisons. We recognize that these laboratory endeavors are tasks of remarkable difficulty for the achievement of a specified and fully measurable free-stream flow and for accurate measurements of the velocity and temperature profiles within the boundary layer. The nonlinear extension of the present work and the intimately linked secondary instability are certainly research avenues of utmost interest that we are going to pursue.

References

Boiko, A., Ivanov, A., Kachanov, Y., and Mischenko, D. (2010a). Investigation of weakly-nonlinear development of unsteady Görtler vortices. *Thermophys. Aeromech.*, 17(4):455–481.

Boiko, A., Ivanov, A., Kachanov, Y., and Mischenko, D. (2010b). Steady and unsteady Görtler boundary-layer instability on concave wall. *Europ. J. Mech. B/Fluids*, 29(2):61–83.

Boiko, A., Ivanov, A., Kachanov, Y., Mischenko, D., and Nechepurenko, Y. (2017). Excitation of unsteady Görtler vortices by localized surface nonuniformities. *Theor. Comput. Fluid Dyn.*, 31(1):67–88.

Borodulin, V., Ivanov, A., Kachanov, Y., and Mischenko, D. (2017). Systematic study of distributed excitation of unsteady Görtler modes by freestream vortices. *Eur. J. Mech. - B/Fluids*.

Cebeci, T. (2002). *Convective Heat Transfer*. Springer-Verlag, Berlin Heidelberg.

Chen, F., Malik, M., and Beckwith, I. (1992). Gortler instability and supersonic quiet nozzle design. *AIAA J.*, 30(8):2093–2094.

Choudhari, M. (1996). Boundary layer receptivity to three-dimensional unsteady vortical disturbances in the free stream. *AIAA Paper 96-0181*.

Ciolkosz, L. and Spina, E. (2006). An experimental study of Görtler vortices in compressible flow. *AIAA Paper*, (4512):1–21.

Dando, A. and Seddougui, S. (1993). The compressible Görtler problem in two-dimensional boundary layers. *IMA J. Appl. Math.*, 51(1):27–67.

De Luca, L., Cardone, G., Aymer de la Chevalerie, D., and Fonteneau, A. (1993). Görtler instability of a hypersonic boundary layer. *Exp. Fluids*, 16:10–16.

Denier, J., Hall, P., and Seddougui, S. (1991). On the receptivity problem for Görtler vortices: vortex motions induced by wall roughness. *Phil. Trans. R. Soc. Lond. A*, 335(1636):51–85.

El-Hady, N. and Verma, A. (1983). Growth of Görtler vortices in compressible boundary layers along curved surfaces. *J. Eng. Applied Sc.*, 2(3):213–238.

Finnis, M. and Brown, A. (1997). The linear growth of Görtler vortices. *Int. J. Heat and Fluid Flow*, 18(4):389–399.

Flechner, S., Jacobs, P., and Whitcomb, R. (1976). A high subsonic speed wind tunnel investigation of winglets on a representative second-generation jet transport wing. *NASA TN D-8264*.

Floryan, J. (1991). On the Görtler instability of boundary layers. *Prog. in Aerosp. Sci.*, 28(3):235–271.

Floryan, J. and Saric, W. (1982). Stability of Görtler vortices in boundary layers. *AIAA J.*, 20(3):316–324.

Ginoux, J. (1971). Streamwise vortices in reattaching high-speed flows: a suggested approach. *AIAA J.*, 9(4):759–760.

Goldstein, M. (1978). Unsteady vortical and entropic distortions of potential flows round arbitrary obstacles. *J. Fluid Mech.*, 89:433–468.

Goldstein, M. (1983). The evolution of Tollmien-Schlichting waves near a leading edge. *J. Fluid Mech.*, 127:59–81.

Görtler, H. (1940). Uber eine Dreidimensionale Instabilitat Laminarer Grenzschichten am Konkaven Wanden. *Naschr Wiss Gas, Gottingen Math Phys Klasse*, 2(1).

Graziosi, P. and Brown, G. (2002). Experiments on stability and transition at Mach 3. *J. Fluid Mech.*, 472:83–124.

Gulyaev, A., Kozlov, V., Kuzenetsov, V., Mineev, B., and Sekundov, A. (1989). Interaction of a laminar boundary layer with external turbulence. *Fluid Dynamics. Translated from Izv, Akad. Navk. SSSR Mekh. Zhid. Gaza 6, vol. 5, pp. 55-65.*, 24(5):700–710.

Hall, P. (1983). The linear development of Görtler vortices in growing boundary layers. *J. Fluid Mech.*, 130:41–58.

Hall, P. (1990). Görtler vortices in growing boundary layers: the leading edge receptivity problem, linear growth and the nonlinear breakdown stage. *Mathematika*, 37(74):151–189.

Hall, P. and Fu, Y. (1989). On the Görtler vortex instability mechanism at hypersonic speeds. *Theor. Comp. Fluid Dyn.*, 1(3):125–134.

Hall, P. and Malik, M. (1989). The growth of Görtler vortices in compressible boundary layers. *J. Eng. Math.*, 23(3):239–251.

Hammerlin, G. (1961). Über die Stabilität einer kompressiblen Strömung längs einer konkaven Wand bei verschiedenen Wand-temperaturverhältnissen. *Deutsche Versuchsanstalt für Luftfahrt*, (176).

Hewitt, R. E. and Duck, P. W. (2014). Three-dimensional boundary layers with short spanwise scales. *J. Fluid Mech.*, 756:452–469.

Hewitt, R. E. and Duck, P. W. (2018). Localised streak solutions for a blasius boundary layer. *J. of Fluid Mech.*, 849:885–901.

Jaffe, N., Okamura, T., and Smith, A. (1970). Determination of spatial amplification factors and their application to predicting transition. *AIAA paper*, 8(2):301–308.

Kemp, N. (1951). The laminar three-dimensional boundary layer and a study of the flow past a side edge. *MSc Thesis, Cornell University*.

Kobayashi, R. and Kohama, Y. (1977). Taylor-Görtler instability of compressible boundary layers. *AIAA J.*, 15(12):1723–1727.

Kottke, V. (1988). On the instability of laminar boundary layers along concave walls towards Görtler vortices. In *Propagation in Systems Far from Equilibrium*, pages 390–398. Springer.

Lam, S. and Rott, N. (1993). Eigen-Functions of linearized unsteady boundary layer equations. *J. Fluids Eng.*, 115:597–602.

Laufer, J. (1954). Factors affecting transition Reynolds numbers on models in supersonic wind tunnels. *J. Aero. Sc.*, 21:497–498.

Leib, S., Wundrow, D., and Goldstein, M. (1999). Effect of free-stream turbulence and other vortical disturbances on a laminar boundary layer. *J. Fluid Mech.*, 380:169–203.

Li, F., Choudhari, M., Chang, C.-L., Greene, P., and Wu, M. (2010). Development and breakdown of gortler vortices in high speed boundary layers. In *48th AIAA Aero. Sc. Meeting*, page 705.

Liepmann, H. (1945). Investigation of boundary layer transition on concave walls. *NACA Wartime Rep. W87*.

Malik, M., Li, F., Choudhari, M., and Chang, C. (1999). Secondary instability of crossflow vortices and swept-wing boundary layer transition. *J. Fluid Mech.*, 399:85–115.

Mangalam, S., Dagenhart, J., Hepner, T., and Meyers, J. (1985). The Görtler instability on an airfoil. *AIAA Paper*, 85-0491.

Marensi, E. and Ricco, P. (2017). Growth and wall-transpiration control of nonlinear unsteady Görtler vortices forced by free-stream vortical disturbances. *Phys. Fluids*, 29(11):114106.

Matsubara, M. and Alfredsson, P. (2001). Disturbance growth in boundary layers subjected to free-stream turbulence. *J. Fluid Mech.*, 430:149–168.

Mayle, R. (1991). The role of laminar-turbulent transition in gas turbine engines. *J. Turbom.*, 113(4):509–537.

Ovchinnikov, V., Choudhari, M., and Piomelli, U. (2008). Numerical simulations of boundary-layer bypass transition due to high-amplitude free-stream turbulence. *J. Fluid Mech.*, 613:135–169.

Ren, J. and Fu, S. (2015). Secondary instabilities of Görtler vortices in high-speed boundary layer flows. *J. Fluid Mech.*, 781:388–421.

Ricco, P. (2009). The pre-transitional Klebanoff modes and other boundary layer disturbances induced by small-wavelength free-stream vorticity. *J. Fluid Mech.*, 638:267–303.

Ricco, P., Tran, D.-L., and Ye, G. (2009). Wall heat transfer effects on Klebanoff modes and Tollmien-Schlichting waves in a compressible boundary layer. *Phys. Fluids*, 21(024106).

Ricco, P., Walsh, E., Brighenti, F., and McEligot, D. (2016). Growth of boundary-layer streaks due to free-stream turbulence. *Int. J. Heat Fluid Flow*, 61:272–283.

Ricco, P. and Wu, X. (2007). Response of a compressible laminar boundary layer to free-stream vortical disturbances. *J. Fluid Mech.*, 587:97–138.

Saric, W. (1994). Görtler vortices. *Annu. Rev. Fluid Mech.*, 26(1):379–409.

Saric, W., Reed, H., and Kerschen, E. (2002). Boundary-layer receptivity to freestream disturbances. *Ann. Rev. Fluid Mech.*, 34:291.

Schneider, S. (2008). Development of hypersonic quiet tunnels. *J. Spacecr. Rock.*, 45-4:641–664.

Smith, A. (1955). On the growth of Taylor-Görtler vortices along highly concave walls. *Quart. J. Math.*, 13(3):233–262.

Spall, R. and Malik, M. (1989). Görtler vortices in supersonic and hypersonic boundary layers. *Phys. Fluids*, 1(11):1822–1835.

Squire, H. (1933). On the stability for three-dimensional disturbances of viscous fluid flow between parallel walls. In *Proc. R. Soc. Lond. A*, volume 142, pages 621–628. The Royal Society.

Stewartson, K. (1964). *The theory of laminar boundary layers in compressible fluids*. Oxford, Claredon Press.

Swearingen, J. and Blackwelder, R. (1983). Parameters controlling the spacing of streamwise vortices on concave walls. *AIAA Paper*, (83-0380).

Tani, I. (1962). Production of longitudinal vortices in the boundary layer along a concave wall. *J. Geophys. Res.*, 67(8):3075–3080.

Tollmien, W. (1929). Uber die Entstehung der Turbulenz 1. Mitteilung. in Math. Phys. Kl. (pp. 21–44). Nach. Ges. Wiss. Göttingen (Translated into English as NACA TM 609 (1931)).

Van Ingen, J. (1956). A suggested semi-empirical method for the calculation of the boundary layer transition region. *Technische Hogeschool Delft, Vliegtuigbouwkunde, Rapport VTH-74*.

Viaro, S. and Ricco, P. (2018). Neutral stability curves of low-frequency Görtler flow generated by free-stream vortical disturbances. *J. Fluid Mech.*, 845(R1).

Volino, R. and Simon, T. (1995). Bypass transition in boundary layers including curvature and favorable pressure gradient effects. *J. Turbomach.*, 117(1):166–174.

Wadey, P. (1992). On the linear development of Görtler vortices in compressible boundary layers. *Europ. J. Mech. B/Fluids*, 11:705–717.

Wang, Q.-C., Wang, Z.-G., and Zhao, Y.-X. (2018). Visualization of Görtler vortices in supersonic concave boundary layer. *J. Visual.*, 21(1):57–62.

Whang, C. and Zhong, X. (2002). Receptivity of Görtler vortices in hypersonic boundary layers. *AIAA Paper 2002-0151*.

Whang, C. and Zhong, X. (2003). Leading edge receptivity of Görtler vortices in a Mach 15 flow over a blunt wedge. *AIAA Paper 2003-0790*.

Wu, X. and Moin, P. (2009). Direct numerical simulation of turbulence in a nominally zero-pressure-gradient flat-plate boundary layer. *J. Fluid Mech.*, 630:5–41.

Wu, X., Zhao, D., and Luo, J. (2011). Excitation of steady and unsteady Görtler vortices by free-stream vortical disturbances. *J. Fluid Mech.*, 682:66–100.

Xu, D., Zhang, Y., and Wu, X. (2017). Nonlinear evolution and secondary instability of steady and unsteady Görtler vortices induced by free-stream vortical disturbances. *J. Fluid Mech.*, 829:681–730.

Appendix A

Numerical methodology

We here describe the numerical procedures used for the two theoretical frameworks, i.e., the LUBR framework and the eigenvalue framework. Through a careful grid convergence analysis, the numerical results have been compared successfully with the results of Ricco and Wu (2007) for the compressible flow over a flat plate and of Wu et al. (2011) for the incompressible flow over concave surfaces.

LUBR framework

The code used to solve the LUBR equations for the optimal curvilinear coordinate system is a modification of the code used by Ricco and Wu (2007) for a Cartesian coordinate system. The code was also modified to introduce the independent variable $\hat{x}$ instead of $\bar{x}$. The parabolic nature of the equations allows using a marching scheme. The equations (3.9)-(3.13), complemented by the boundary conditions (3.14)-(3.19) and the initial conditions (3.20)-(3.24), are solved with a second-order finite-difference scheme, central in η and backward in $\hat{x}$. In reference to figure A.1, the derivatives of a fluid property $\mathbf{q}(\hat{x},\eta) = \{u, v, w, \tau\}$ are

$$\frac{\partial q}{\partial \eta} \approx \frac{q_{j+1} - q_{j-1}}{2\Delta\eta}, \quad \frac{\partial^2 q}{\partial \eta^2} \approx \frac{q_{j+1} - 2q_j - q_{j-1}}{(\Delta\eta)^2}, \quad \frac{\partial q}{\partial \hat{x}} \approx \frac{\frac{3}{2}q_{i,j} - 2q_{i-1,j} + \frac{1}{2}q_{i-2,j}}{\Delta\hat{x}}. \tag{A.1}$$

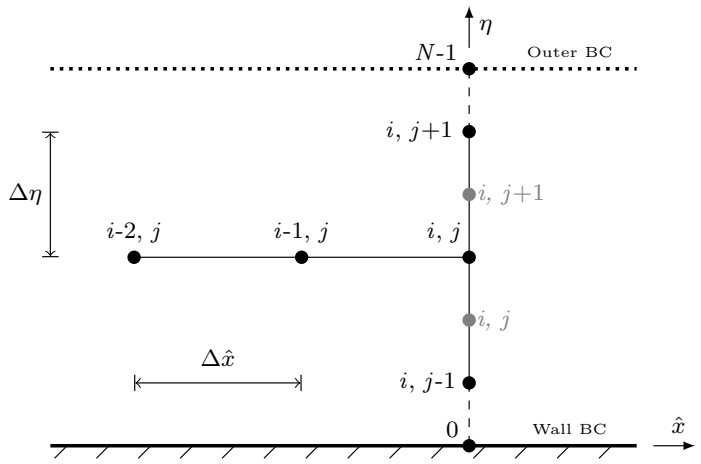

Fig. A.1 Sketch of the regular grid (black) and staggered grid (gray) used for the numerical scheme.

If the pressure is computed on the same grid as the velocity components, pressure decoupling phenomenon occurs. Therefore, the pressure is computed on a grid staggered in η as

$$p \approx \frac{p_{j+1} + p_j}{2}, \qquad \frac{\partial p}{\partial \eta} \approx \frac{p_{j+1} - p_j}{\Delta \eta}, \tag{A.2}$$

where the pressure at the wall does not have to be specified and it is calculated a posteriori by solving the z-momentum equation at $\eta = 0$. Due to the linearity of the equations, the system is in the form $\mathbf{Ax} = \mathbf{b}$. In a grid with N points along η, $\mathbf{A}$ is a $(N-2) \times (N-2)$ block-tridiagonal matrix where each block is a 5×5 matrix associated to the 5 unknowns $(\bar{u}, \bar{v}, \bar{w}, \bar{p}, \bar{\tau})$. Therefore, the wall-normal index j of the vectors and matrix runs from 1 through $N-2$. The numerical procedure used to solve the linear system can be found in the book of Cebeci (2002) on pages 260-264.

Eigenvalue framework

The eight first-order equations of the EV framework are discretized using a second-order implicit finite-difference scheme. The original homogeneous system is solved by enforcing the normalized boundary condition $\tilde{f} = 1$, instead of $\tilde{u} = 0$, at $\eta = 0$. The initial guess for the eigenvalue $\sigma(\hat{x})$ is taken from the LUBR solution and iterated using the Newton's method until the original homogeneous boundary condition $\tilde{u} = 0$ is recovered. For this reason it is

more computationally expensive than solving for the LUBR equations, which only require a small streamwise discretization (Spall and Malik, 1989). The typical value for the number of grid points N in the wall-normal direction and the streamwise discretization $\Delta\hat{x}$ is $N \approx 3000$ with $\eta_{\max} \approx 30$ and $\Delta\hat{x} \approx 0.1$.

Appendix B

Upstream behaviour of the LUBR equations

In the limit of $\hat{x} \to 0$ the LUBR solution can be obtained analytically for $\eta = \mathscr{O}(1)$ and $\eta \to \infty$. Summing these two solutions and subtracting their common parts, i.e., the values in the region along η where both solutions are valid, we obtain the upstream perturbation profiles that are uniformly valid for all η (3.20)-(3.24). These profiles provide the initial conditions for the LUBR equations (3.9)-(3.13). Details on this analysis are found in Leib et al. (1999), in which the initial conditions are equivalent, after rescaling in the $(\hat{x}, \eta)$ coordinates, to the ones here summarized in the following steps:

1. The first step consists in writing the LUBR equations in terms of the variable

$$y^{(0)} = (2\hat{x})^{1/2}(k_x \mathrm{R})^{1/2}\overline{\eta}. \tag{B.1}$$

in the limit $\eta \to \infty$. Their solution that matches with the flow in the region IV of figure 3.1 outside the boundary layer is (Leib et al., 1999)

$$\bar{u} = 0, \tag{B.2}$$

$$\bar{v} = \frac{ie^{ik_x \mathrm{R}\hat{x}}}{(2\hat{x})^{1/2}\,(k_y - i|k_z|)} \left[e^{ik_y(2\hat{x})^{1/2}\bar{\eta} - (k_y^2 + k_z^2)\hat{x}} - e^{-|k_z|(2\hat{x})^{1/2}\bar{\eta}} \right] +$$

$$\frac{|k_z|}{(2\hat{x})^{1/2}} e^{ik_x \mathrm{R}\hat{x} - |k_z|(2\hat{x})^{1/2}\bar{\eta}} \int_0^{\hat{x}} g(\check{x}) \mathrm{e}^{-ik_x \mathrm{R}\check{x}} \mathrm{d}\check{x}, \tag{B.3}$$

$$\bar{w} = \frac{e^{ik_x \mathrm{R}\hat{x}}}{k_y - i|k_z|} \left[k_y e^{ik_y (2\hat{x})^{1/2}\bar{\eta} - (k_y^2 + k_z^2)\hat{x}} - i|k_z| e^{-|k_z|(2\hat{x})^{1/2}\bar{\eta}} \right] +$$

$$k_z^2 e^{ik_x \mathrm{R}\hat{x} - |k_z|(2\hat{x})^{1/2}\bar{\eta}} \int_0^{\hat{x}} g(\check{x}) \mathrm{e}^{-ik_x \mathrm{R}\check{x}} \mathrm{d}\check{x}, \tag{B.4}$$

$$\bar{p} = g(\hat{x}) e^{-|k_z|(2\hat{x})^{1/2}\bar{\eta}}, \tag{B.5}$$

$$\bar{\tau} = 0. \tag{B.6}$$

The limit of (B.2)-(B.6) for $\hat{x} \to 0$ represent the first part of the upstream perturbation profiles.

2. The second step consists in substituting the power series solution

$$\bar{\mathbf{q}}(\hat{x}, \eta) = \sum_{n=0}^{\infty} (2\hat{x})^{n/2} \left[2\hat{x}\, U_n(\eta), V_n(\eta), W_n(\eta), (2\hat{x})^{-1/2} P_n(\eta), 2\hat{x}\, T_n(\eta) \right] \tag{B.7}$$

for $\eta = \mathscr{O}(1)$ and $\hat{x} \to 0$ into the LUBR equations (3.9)-(3.13) and equating the terms of like powers of $\hat{x}$. We obtain the system of ordinary differential equations for the leading terms in the power series, $n = 0$,

$$\mathscr{C}] \quad \left(\frac{\eta_c T'}{T} + 2 \right) U_0 - \eta_c U_0' - \frac{T'}{T^2} V_0 + \frac{1}{T} V_0' + W_0 - \left(\frac{F T'}{T^2} + \frac{2F'}{T} \right) T_0 + \frac{F}{T} T_0' = 0, \tag{B.8}$$

$$\mathscr{X}| \quad \left(2F' - \eta_c F''\right) U_0 - \left[F + \left(\frac{\mu}{T} \right)' \right] U_0' - \frac{\mu}{T} U_0'' + \frac{F''}{T} V_0 + \left[\frac{F F''}{T} - \left(\frac{\mu' F''}{T} \right)' \right] T_0$$
$$- \frac{\mu' F''}{T} T_0' = 0, \tag{B.9}$$

$$\mathscr{Y}| \quad P_0' = 0, \tag{B.10}$$

$$\mathscr{Z}| \quad \left(F+\frac{\mu' T'}{T}-\frac{\mu T'}{T^2}\right) W_0' + \frac{\mu}{T} W_0'' = 0, \tag{B.11}$$

$$\mathscr{E}\rfloor \quad -\eta_c T' U_0 - \frac{2M^2(\gamma-1)\mu F''}{T} U_0' + \frac{T'}{T} V_0 + \left[\frac{FT'+2TF'}{T} - \frac{1}{\mathtt{Pr}}\left(\frac{\mu' T'}{T}\right)' - \frac{\mathtt{M}^2(\gamma-1)F''^2\mu'}{T}\right] T_0 - \left(F+\frac{2\mu' T'}{\mathtt{Pr}T}-\frac{\mu T'}{\mathtt{Pr}T^2}\right) T_0' - \frac{\mu}{\mathtt{Pr}T} T_0'' = 0, \tag{B.12}$$

and the system of ordinary differential equations for the second-order terms in the power series, $n = 1$,

$$\mathscr{C}\rceil \quad \left(\frac{\eta_c T'}{T}+3\right) U_1 - \eta_c U_1' - \frac{T'}{T^2} V_1 + \frac{1}{T} V_1' + W_1 - \left(\frac{FT'}{T^2}+\frac{3F'}{T}\right) T_1 + \frac{F}{T} T_1' = 0, \tag{B.13}$$

$$\mathscr{X}| \quad (3F' - \eta_c F'') U_1 - \left[F + \left(\frac{\mu}{T}\right)'\right] U_1' - \frac{\mu}{T} U_1'' + \frac{F''}{T} V_1 + \left[\frac{FF''}{T} - \left(\frac{\mu' F''}{T}\right)'\right] T_1 - \frac{\mu' F''}{T} T_1' = 0, \tag{B.14}$$

$$\mathscr{Y}| \quad P_1' = \left[\eta_c(TF' - FT - FT') + \eta_c^2 F'' T - \frac{4\mu' T'}{3}\right] U_0 + \frac{1}{3}\left[\mu - \eta_c T\left(\frac{\mu}{T}\right)'\right] U_0' - \frac{\eta_c \mu}{3} U_0'' + \left(-F' - \eta_c F'' + \frac{FT'}{T}\right) V_0 + \left[F + \frac{4}{3}\left(\frac{\mu}{T}\right)'\right] V_0' + \frac{4\mu}{3T} V_0'' - \frac{2\mu' T'}{3} W_0 + \frac{\mu}{3} W_0' + \left[FF' + \frac{F^2 T'}{T} + 3\mu' F'' - \eta_c (FF')' + \eta_c T\left(\frac{\mu' F''}{T}\right)' - \frac{4}{3}\left(\frac{\mu' T' F}{T}\right)'\right] T_0 + \left(\eta_c \mu' F'' - \frac{4\mu' T' F}{3T}\right) T_0', \tag{B.15}$$

$$\mathscr{Z}| \quad -F' W_1 + \left(F + \frac{\mu' T'}{T} - \frac{\mu T'}{T^2}\right) W_1' + \frac{\mu}{T} W_1'' + k_z^2 T P_0 = 0, \tag{B.16}$$

$$\mathscr{E}\rfloor \quad -\eta_c T' U_1 - \frac{2\mathtt{M}^2(\gamma-1)\mu F''}{T}U_1' + \frac{T'}{T}V_1 + \left[\frac{FT'+3TF'}{T} - \frac{1}{\mathtt{Pr}}\left(\frac{\mu' T'}{T}\right)'\right.$$
$$\left. -\frac{\mathtt{M}^2(\gamma-1)F''^2\mu'}{T}\right]T_1 - \left(F + \frac{2\mu' T'}{\mathtt{Pr}T} - \frac{\mu T'}{\mathtt{Pr}T^2}\right)T_1' - \frac{\mu}{\mathtt{Pr}T}T_1'' = 0. \tag{B.17}$$

These two systems must be solved by imposing the wall no-slip conditions on the velocity and a null temperature gradient at the wall. The boundary conditions for $\eta \to \infty$ are found by expanding (B.2)-(B.6) for $\hat{x} \to 0$ and $\eta = \mathscr{O}(1)$. It follows that

$$\bar{v} \to -\overline{\eta} - \frac{i}{2}(2\hat{x})^{1/2}(k_y + i|k_z|)\left(\overline{\eta}^2 + 1\right)$$
$$+ \frac{|k_z|}{(2\hat{x})^{1/2}}\left[1 - |k_z|(2\hat{x})^{1/2}\overline{\eta}\right]\int_0^{\hat{x}} g(\check{x})\mathrm{e}^{-ik_x \mathtt{R}\check{x}}\mathrm{d}\check{x} + \dots, \tag{B.18}$$

$$\bar{w} \to 1 + (2\hat{x})^{1/2} i\,(k_y + i|k_z|)\,\overline{\eta} + k_z^2 \int_0^{\hat{x}} g(\check{x})\mathrm{e}^{-ik_x \mathtt{R}\check{x}}\mathrm{d}\check{x} + \dots. \tag{B.19}$$

The small-$\hat{x}$ asymptote of the unknown function $g(\hat{x})$ must now be found. We do this by matching (B.18) with the large-η limit of V_0 in (B.7). Introducing the viscosity-induced transpiration velocity V_c as

$$V_c = -\lim_{\eta\to\infty}(V_0 - \overline{\eta}), \tag{B.20}$$

we find that for $\hat{x} \to 0$

$$g(\hat{x}) \to -\frac{V_c}{|k_z|(2\hat{x})^{1/2}} + g_1 + \dots, \tag{B.21}$$

where the constant g_1 is unknown at this point. Matching with the solution for pressure (5.31) of Leib et al. (1999) shows that $P_0 \to -V_c/|\kappa|$ and $P_1 \to g_1 + V_c\overline{\eta}$ for $\eta \to 0$. After substitution of (B.21) into (B.19) and comparing with the form of the power series, one finds that the boundary conditions for $\eta \to \infty$ of W_0 and W_1 are $W_0 \to 1$ and $W_1 \to i(k_y + i|k_z|)\overline{\eta} - V_c|k_z|$, respectively. The boundary conditions on U_0 and U_1 are also easily found by comparing (5.20) of Leib et al. (1999) and $\bar{\tau} = 0$ with the power series solution. Therefore, U_0 and $U_1 \to 0$ for $\eta \to \infty$. No boundary condition needs to be specified on the vertical velocity component, but the large-η asymptote of V_1 is useful for determining the constant g_1. Indeed, setting $U_1 = 0$ in the continuity

equation (B.13) and using the large-η limit of W_1, one finds that for $\eta \to \infty$

$$V_1 = -i\,(k_y + i|k_z|)\left(\frac{\eta^2}{2} - \beta_c \eta\right) + V_c|k_z|\eta + c_1, \tag{B.22}$$

where c_1 is a constant depending on k_y and k_z. Matching the above expression with the $\mathscr{O}((2\hat{x})^{1/2})$ term of (B.18) yields

$$g_1 = \frac{2c_1}{|k_z|} + 2V_c\beta_c + \frac{i}{|k_z|}\left(\beta_c^2 + 1\right)(k_y + i|k_z|). \tag{B.23}$$

3. Finally, comparing (B.7) with the small-x expansion (B.2)-(B.6), we find their common parts, denoted by $\overline{v}_c$, $\overline{w}_c$ and $\overline{p}_c$, as follows:

$$\overline{v}_c = -\overline{\eta} - V_c + (2\hat{x})^{1/2}\left[-\frac{i}{2}(k_y + i|k|)\left(\overline{\eta}^2 + 1\right) + V_c|k_z|\overline{\eta} + \frac{1}{2}|k_z|g_1\right], \tag{B.24}$$

$$\overline{w}_c = 1 + (2\hat{x})^{1/2}\left[i(k_y + i|k_z|)\overline{\eta} - V_c|k_z|\right], \tag{B.25}$$

$$\overline{p}_c = \frac{P_0}{(2\hat{x})^{1/2}} + g_1 + V_c\overline{\eta}. \tag{B.26}$$